THREE-DIMENSIONAL MODELING OF SHAPE MEMORY POLYMERS CONSIDERING FINITE DEFORMATIONS AND HEAT TRANSFER

A Dissertation

by

BRENT LOUIS VOLK

Submitted to the Office of Graduate Studies of
Texas A&M University
in partial fulfillment of the requirements for the degree of

DOCTOR OF PHILOSOPHY

Approved by:

Co-Chairs of Committee,	Duncan J. Maitland
	Dimitris C. Lagoudas
Committee Members,	John C. Criscione
	Jay R. Walton
	Thomas Wilson
Intercollegiate Faculty Chair,	Ibrahim Karaman

December 2012

Major Subject: Materials Science and Engineering

ABSTRACT

Shape memory polymers (SMPs) are a relatively new class of active materials that can store a temporary shape and return to the original configuration upon application of a stimulus such as temperature. This shape changing ability has led to increased interest in their use for biomedical and aerospace applications. A major challenge, however, in the advancement of these applications is the ability to accurately predict the material behavior for complex geometries and boundary conditions. This work addresses this challenge by developing an experimentally calibrated and validated constitutive model that is implemented as a user material subroutine in Abaqus – a commercially available finite element software package.

The model is formulated in terms of finite deformations and assumes the SMP behaves as a thermoelastic material, for which the response is modeled using a compressible neo-Hookean constitutive equation. An internal state variable, the glassy volume fraction, is introduced to account for the phase transformation and associated stored deformation upon cooling from the rubbery phase to the glassy phase and subsequently recovered upon heating. The numerical implementation is performed such that a system of equations is solved using a Newton-Raphson method to find the updated stress in the material. The conductive heat transfer is incorporated through solving Fourier's law simultaneously with the constitutive equations.

To calibrate and validate the model parameters, thermomechanical experiments are performed on an amorphous, thermosetting polyurethane shape memory polymer.

Strains of 10-25% are applied and both free recovery (zero load) and constrained displacement recovery boundary conditions are considered for each value of applied strain. Using the uniaxial experimental data, the model is then calibrated and compared to the 1-D experimental results. The validated finite element analysis tool is then used to model biomedical devices, including cardiovascular tubes and thrombectomy devices, fabricated from shape memory polymers. The effects of heat transfer and complex thermal boundary conditions are evaluated using coupled thermal-displacement analysis, for which the thermal material properties were experimentally calibrated.

To Grandpa Lowry, who motivated and inspired me,

to Abby, who supported and believed in me,

and to my friends and family, who encouraged and strengthened me

ACKNOWLEDGEMENTS

I would first like to acknowledge my co-advisors, Drs. Duncan Maitland and Dimitris Lagoudas. Both individuals have played a tremendously influential role in my life, understanding and helping me pursue my goals, and ultimately shaping the researcher and person that I have become.

I have to personally thank Dr. Maitland for moving to Texas at just the right time. It was simply a matter of luck that he saw my MSEN seminar flyer in an elevator and decided to attend my presentation. From there, he joined my MS committee and then became my PhD co-advisor. Coming from a national laboratory setting, Dr. Maitland has brought a unique perspective and background to my academic and professional growth. He has challenged me with real-world engineering questions and problems and caused me to think outside of my mechanics bubble. He has been a role model for balancing professional, academic, and personal responsibilities and relationships.

I would like to thank Dr. Lagoudas for taking the risk in bringing in a sophomore Aerospace Engineering graduate student into his research group. For the last 7.5 years, his guidance, teachings, and support have molded me both academically and professionally. From preparing proposals to last-minute conference proceedings & presentations, he has brought out the best in me and helped me learn to take a step back and critically think about the problem at hand. Through international trips, student exchanges, retreats, and food competitions, he has broadened my horizon to the

globalization of today's engineering community and has motivated me to keep aware of history, current events, and global perspectives.

I would also like to thank my other committee members, Drs. John Criscione, Jay Walton, and Tom Wilson. I consider myself extremely fortunate to have a committee that has been willing to aid in my learning and to engage in technical discussions over the course of my research. In particular, I would like to thank Dr. Criscione for his willingness to drop everything and discuss mechanics for lengthy stretches. His insight and our discussions further developed my ability to abstractly and technically think about existing problems in new ways. Finally, I would like to thank Dr. Wilson for his routine discussions on the material fabrication and testing. His material science and chemistry background have engaged and enhanced my ability to relate abstract modeling concepts to the physical response of the material.

I am also grateful for the support provided throughout my graduate education by the National Science Foundation Integrative Graduate Education and Research Traineeship as well as the National Defense Science and Engineering Graduate fellowship. I am especially grateful to the support and assistance provided by Bonnie Reid, Barbara Slusher, and Jan Gerston. Bonnie has provided a steady source of calmness and serenity, even when schedules and tasks got hectic. Her attention to detail, ability to multitask, care for the students, and patience with me when I would bug her with endless questions is unparalleled. Thanks to Barbara for her continuous help in reserving rooms, ordering supplies, and always providing a caring smile on the 5^{th} floor. Thanks to Jan for her tremendous assistance with all of the IGERT, programmatic, and

OGS requirements. She was always a voice of wisdom and helped make sure everything happened as planned and on time.

My undergraduate and graduate research experiences would not have been the same without the people that surrounded me. I want to thank all of my coworkers for sharing in intense technical discussions as well as social events. Thank you to the entire "modeling group", including Krishnendu Haldar, Majid Tabesh, and Brian Lester. In particular, thank you to Krishnendu for helping me work through numerous continuum mechanics derivations or identities. Thank you to Brian for being a fantastic officemate and peer whom I could bounce ideas or results off of and always count on to consistently remind me that I wasn't the only one struggling with my research. Thank you to Jennifer Rodriguez, Keith Hearon, Wonjun Hwang, Ya-Jen Yu, and Andrea Muschenborn for providing countless memories as a result of both technical and social interactions. I would like to thank Landon Nash, Brookelynn Russey, and Antony Zacharatos. It has been a privilege working with and mentoring you. Your efforts helped make this research great, and you challenged me to look at problems from a different perspective.

I would like to extend a special thanks to Parikshith Kumar and Darren Hartl, both of whom were my mentors from the beginning. Kumar especially taught me how to be a precise and punctual experimentalist and never failed to make sure I was keeping up with my movie-watching responsibilities. In addition, Darren was the best peer mentor, office mate, fellow Aggie, and role model that I could've asked for. He has always been a source of knowledge and experience, and I consider myself fortunate to

have learned from him. In addition, he has been a role model for balancing family, friends, and research.

I would like to thank my family. Thank you to my parents and grandparents for raising me to be the person that I am today. I want to thank them for believing in me, supporting me, and teaching me valuable life lessons and morals. Throughout the many years in College Station, they never wavered in their support and always encouraged me to "do whatever I do best." I thank them for installing a sense of diligence and perseverance in me, without which I would not have been able to get through the challenges of these efforts. I would also like to thank my brothers Eric and Chris. Like any older brothers, they provided their share of (loving) heckling at how long it has taken me to finally graduate. Thank you to Eric for being one of my best friends and confidants. He has been on the receiving ends of many rants or life questions and helped prop me up throughout. I would also like to thank my in-laws. They have accepted me as one of their children and provided me with endless support and encouragement throughout this process. I am fortunate to have them as a source of inspiration and admiration.

Finally, I would like to thank my wife Abby. I especially want to thank her for her patience and support during graduate school as she shared in my triumphs as well as my difficult times. Her understanding of my responsibilities and uncertainties associated with graduate school made things easier. Her love and belief in me made me a stronger person. I am blessed to have such an amazing wife and best friend with whom to share every day.

NOMENCLATURE

α	Coefficient of thermal expansion (α^g for the glassy phase, α^r for the rubbery phase)
δ_{ij}	Kronecker delta (δ_{ij} = 1 when i=j, 0 otherwise)
$\boldsymbol{\varepsilon}$	Logarithmic strain ($\boldsymbol{\varepsilon} = \ln \mathbf{V} = \ln \sqrt{\mathbf{F}\mathbf{F}^{\mathrm{T}}}$)
η	Entropy per unit mass (η_0 is the reference value)
η_c	Entropy per unit volume
θ	Absolute temperature (θ_0 is the initial value), in Kelvin
$\theta_{\max}$	Upper bound for the temperature range over which the glassy volume fraction is fit ($\theta_{\min}$ is the lower bound)
λ	In Chapter IV, the Lamé coefficient (λ^g for the glassy phase, λ^r for the rubbery phase)
λ_i	Principal components of the stretch tensor $\mathbf{U}$ (λ is the axial component, λ^g is the axial component in the glassy phase, λ^r is the axial component in the rubbery phase)
μ	Shear modulus (μ^g for the glassy phase, μ^r for the rubbery phase)
ν	Poisson's ratio (ν^g for the glassy phase, ν^r for the rubbery phase)
ξ	Backtrack parameter ($0 < \xi < 1$) used in the line search method
ρ	Density (ρ_0 is the density in the reference configuration)
$\boldsymbol{\sigma}$	Cauchy stress (1-D form: σ). $\boldsymbol{\sigma}^g$ for the glassy phase, $\boldsymbol{\sigma}^r$ for the rubbery phase
τ	Last time a material point was transformed from the rubbery phase to the glassy phase

$\boldsymbol{\tau}$	Kirchhoff stress tensor
$\overset{\nabla}{\boldsymbol{\tau}}$	Jaumann rate of the Kirchhoff stress tensor
υ	Ratio of the current volume to the reference volume
ϕ	Glassy volume fraction
ϕ_{rev}	Value of the glassy volume fraction at the most recent time when cooling ceased and heating began
Φ	Helmholtz free energy per unit mass
Ψ	Helmholtz free energy per unit volume
Ω	Region over which the volume average is taken
Ω_g	Glassy region
Ω_r	Rubbery region
$\underset{\approx}{\mathbf{a}}$	Fourth order modulus relating the Jaumann rate of the Kirchhoff stress to the rate of deformation tensor
A	Shifting factor for the glassy volume fraction function
$\mathbf{b}$	Body force vector
B	Scaling factor for the glassy volume fraction function
c	Heat capacity per unit mass
c_d	Heat capacity per unit volume
$\underset{\approx}{\mathbf{c}}$	Fourth order spatial (co-rotational) elasticity tensor
C	Normalizing factor for the glassy volume fraction function (applicable when piecewise hyperbolic tangent used)
$\mathbf{C}$	Right Cauchy-Green deformation tensor
$\underset{\approx}{\mathbf{C}}^{mat}$	Fourth order material elasticity tensor derived from the Helmholtz thermodynamic potential

$\mathbb{C}$	Fourth order elasticity tensor (material Jacobian). $\mathbb{C}^g$ for the glassy phase, $\mathbb{C}^r$ for the rubbery phase
CR	Constrained recovery
CTE	Coefficient of thermal expansion
$\mathbf{D}$	Rate of deformation tensor
DMA	Dynamic mechanical analysis
DSC	Differential scanning calorimetry
e_0	Reference internal energy per unit volume
E	Young's modulus (E^g for the glassy phase, E^r for the rubbery phase)
f	Norm of the residual vector
$\mathbf{F}$	Deformation gradient
$\bar{\mathbf{F}}$	Average deformation gradient (written later simply as $\mathbf{F}$)
$\mathbf{F}_{nat}$	Deformation gradient from the rubbery phase stress-free configuration to the glassy phase natural configuration
$\mathbf{F}_e$	Elastic deformation gradient ($\mathbf{F}_e^g$ for the glassy phase, $\mathbf{F}_e^r$ for the rubbery phase)
$\mathbf{F}^{stor}$	Accumulated stored deformation upon cooling from the rubbery phase to the glassy phase
$\mathbf{F}_{rev}^{stor}$	Value of the accumulated stored deformation at the most recent time when cooling ceased and heating began
FR	Free recovery
$g(\xi)$	Norm of the residual vector when the increment in the unknowns is applied
$\mathbf{h}$	Entropy flux

HDI	1,6-hexamethylene diisocyanate
HPED	N,N,N0,N0-tetrakis(2-hydroxy-propyl)ethylenediamine
$\mathbf{I}$	Second order identity tensor
$\underset{\approx}{\mathbf{I}}$	Fourth order identity tensor
$I_{\mathbf{C}}$	First invariant of the right Cauchy-Green deformation tensor
k	Superscript representing the current increment ($k-1$ represents the previous increment)
k^{th}	Thermal conductivity
K	Bulk modulus
J	Determinant of the deformation gradient and a function of the third invariant of $\mathbf{C}$ $\left(J=\sqrt{III_{\mathbf{C}}}\right)$. J^g for the glassy phase and J^r for the rubbery phase
J_{ij}	Components of the Jacobian matrix in the Newton-Raphson method
L	Length (L_0 is the initial value)
$L_v\boldsymbol{\tau}$	Lie derivative of the Kirchhoff stress tensor
p	Hydrostatic pressure required to maintain incompressibility (p^g for the glassy phase, p^r for the rubbery phase)
$\mathbf{P}$	First Piola-Kirchhoff stress
$\mathbf{q}$	Heat flux vector (q_n in the normal direction)
$\mathbf{Q}$	Rotation component of the polar decomposition of $\mathbf{P}$
r	Heat source/sink per unit volume
$\tilde{r}$	Heat source/sink per unit mass

r^{pl}	Volumetric heat generation per unit time caused by mechanical working
$\mathbf{R}$	Rotation component of the polar decomposition of $\mathbf{F}$ ($\mathbf{R}^g$ for the glassy phase, $\mathbf{R}^r$ for the rubbery phase)
R_i	Components of the residual vector used in the Newton-Raphson method
PID	Proportional-integral-derivative
PTFE	Polytetrafluoroethylene
s_i	Principal components of the first Piola-Kirchhoff stress tensor $\mathbf{P}$ (s is the axial component, s^g is the axial component in the glassy phase, s^r is the axial component in the rubbery phase)
$s(t)$	As used as an integral limit, the previous time the material experienced the current temperature
$\mathbf{S}$	Second Piola-Kirchhoff stress
SDV20	Abaqus variable used to represent the glassy volume fraction
SMA	Shape memory alloy
SMC	Shape memory ceramic
SMP	Shape memory polymer
t	Time
$\mathbf{t}$	Traction vector
T	Temperature, usually in degrees Celsius
$\mathbf{T}$	Stretch component of the polar decomposition of $\mathbf{P}$
TEA	Triethanolamine
T_g	Glass transition temperature
T_m	Melting temperature

TMA	Thermomechanical analysis
T_{trans}	Transition temperature (can be melting or glass transition temp.)
u	Internal energy per unit mass (u_0 is the reference value)
$\mathbf{u}$	Vector of unknowns in the Newton-Raphson method
$\mathbf{U}$	Stretch component of the polar decomposition of $\mathbf{F}$ ($\mathbf{U}^g$ for the glassy phase, $\mathbf{U}^r$ for the rubbery phase)
$\mathbf{U}_{nat}$	Stretch component of the deformation gradient from the rubbery phase stress-free configuration to the glassy phase natural configuration
$\mathbf{U}^{stor}$	Accumulated stored deformation upon cooling from the rubbery phase to the glassy phase
$\mathbf{U}_{rev}^{stor}$	Value of the accumulated stored deformation at the most recent time when cooling ceased and heating began
UMAT	User material subroutine in Abaqus
$\mathbf{v}$	Spatial velocity field
V	Volume
$\mathbf{W}$	Spin tensor
$\mathbf{X}$	Material point vector in the reference configuration

TABLE OF CONTENTS

Page

LIST OF FIGURES

Page

LIST OF TABLES

Page

CHAPTER I

INTRODUCTION AND LITERATURE REVIEW

Breakthroughs in engineering designs and applications are often a result of research and innovation in material systems. Through a better understanding of the fundamental material behavior, new materials have been designed to provide multifunctional capability and/or solve complex engineering problems. Advances in composite and active materials has directly impacted the state of the art in engineering, from composite and morphing panels on new commercial and military aircraft to shape changing metals being used for cardiovascular stents and aneurysm treatments . More recently, advances in new stimuli-responsive polymer systems – including piezoelectric, electroactive, and shape memory polymers (SMPs) – has broadened the engineering design space by introducing multifunctionality into materials that are capable of large deformations.

Shape memory polymers are a relatively new class of active materials that are capable of storing a temporary shape and then returning to its original, permanent shape upon the application of a stimulus such as heat [1-9]. As such, SMPs join the broader category of shape memory materials, which contains shape memory alloys (SMAs) and shape memory ceramics (SMCs). Compared to these other shape memory materials, SMPs are lightweight, inexpensive, and can recover large deformations. This shape changing ability has led to increased interest in their use for biomedical and aerospace applications. A major challenge, however, in the advancement of these applications is the ability to understand and accurately predict the material behavior for complex

geometries and boundary conditions. This dissertation addresses these challenges by performing an experimental characterization of a new thermosetting shape memory polymer and by developing an experimentally calibrated and validated constitutive model that is implemented as a subroutine in Abaqus® – a commercially available finite element software package.

I.A. Shape Memory Effect

The shape memory effect can be observed to some extent in all polymer systems; however, the term shape memory polymer generally refers to systems in which the shape memory effect has been specifically tailored or exploited in an application. This section provides an overview of the standard thermomechanical cycle, the broad categories of shape memory polymers, and an overview of the mechanism responsible for the shape memory effect as related to the categories of SMPs.

I.A.1. Thermomechanical Cycle

As this work focuses on thermally activated shape memory polymers, the cycle for inducing the shape memory effect will be limited to that which requires a change in temperature. The general thermomechanical cycle for such SMPs [1-9] is as follows and is shown in Figure 1:

(1) Heat the material to above the transition temperature and deform the material to a new configuration

(2) Cool the material to below the transition temperature under constraint (constant strain or constant force) to 'fix' the material

(3) Hold the temperature below the transition temperature and reduce the force to zero

(4a) Heat the material at zero load (free recovery), or

(4b) Heat the material at constant displacement (constrained recovery)

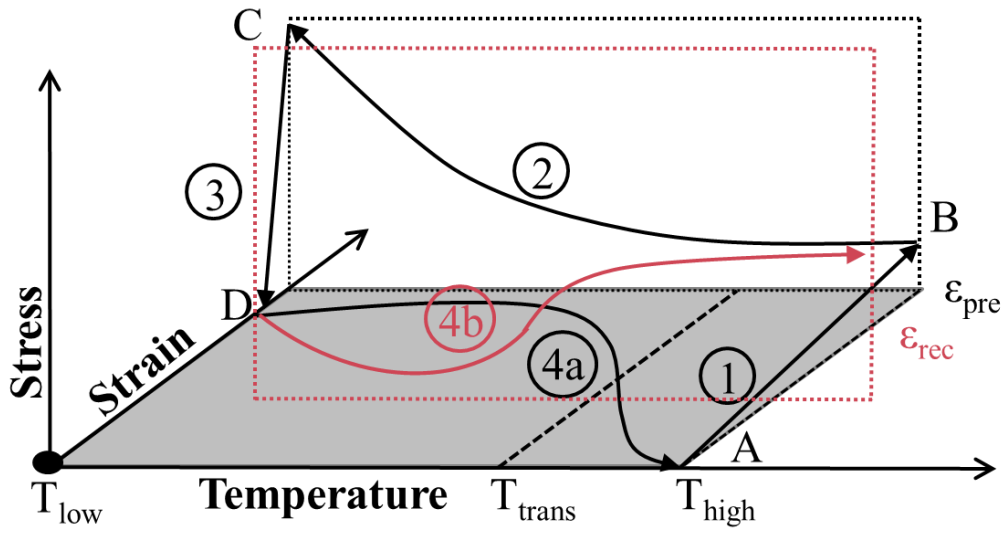

Figure 1 – Schematic of the thermomechanical cycle for shape memory polymers. Large deformations are imposed along (1), the SMP is cooled along (2) to lock in the temporary shape, and the thermal stress is released during unloading along path (3). The free and constrained displacement paths are shown in (4a) and (4b), respectively.

I.A.2. Categories of Shape Memory Polymers

In SMPs, the transition temperature T_{trans} can be the glass transition temperature (T_g) and/or the melting temperature (T_m). In [1, 10] , shape memory polymers were placed into four categories based on their transition temperature and molecular structure. The four categories were:

(I) Covalently cross-linked glassy thermosetting polymers,

(II) Covalently cross-linked semi-crystalline polymers,

(III) Physically cross-linked glassy copolymers, and

(IV) Physically cross-linked semi-crystalline copolymers

I.A.2.1. Covalently Cross-Linked Glassy Thermosetting Polymers

The first category of SMPs, type I, is representative of an amorphous, thermosetting polymer. In this type, the material is cured at high temperature to form the covalent cross-links (also known as chemical cross-links). Due to the nature of the polymer chains and molecular structure, however, the polymer does not form crystalline regions upon cooling; thus, the polymer only exhibits a change in material properties about the glass transition temperature. As such, the T_g is the transition temperature invoked during the shape memory cycle.

I.A.2.2. Covalently Cross-Linked Semi-Crystalline Polymers

The second classification of SMP (II) is similar to that of (I) except the polymer is semi-crystalline. In this case, the polymer contains both amorphous regions and

regions which are capable of crystallizing. As such, there is a change in material properties observed during heating to above both the glass transition temperature (for the amorphous regions) and the melting temperature (for the crystalline regions) [4]. Consequently, either the T_g or the T_m can be used as the transition temperature for the shape memory effect.

I.A.2.3. Physically Cross-Linked Glassy Copolymers

The third type of SMP is a copolymer comprised of two (or more) repeating units in which both repeating units are amorphous. In this type of SMP, one segment (commonly referred to as the 'hard' segment or a physical cross-link) has a melting temperature which is higher than the glass transition temperature of the other ('soft') segment [4, 11]. As a result, the glass transition temperature is used as the transition temperature for the shape memory behavior but heating through the melting temperature of the hard phase can be used to remold the permanent shape of the SMP.

I.A.2.4. Physically Cross-Linked Semi-Crystalline Copolymers

The final type of SMP, type IV, is similar to (III) except that the soft segment is semi-crystalline. Therefore, the soft segment will experience both a glass transition and a melting temperature and the polymer will begin flowing upon heating through the melting temperature of the hard segment. In these SMPs, the melting temperature of the soft segment is typically used as the transition temperature for the shape memory effect [1, 2, 4].

I.A.3. Physical Mechanism for the Shape Memory Effect

In this section, the mechanisms of the shape memory capability are briefly discussed. The mechanisms are presented corresponding to the steps presented in the thermomechanical cycle in Figure 1, and they are related to the classes of SMPs presented in the previous section.

I.A.3.1. Loading at High Temperature ($T>T_{trans}$)

In the first step of the shape memory thermomechanical cycle, the material is loaded. It is during this step that the polymer can be loaded to large values of deformation (>10% strain). The mechanism responsible for allowing the large deformations is comparable to that of rubber elasticity. Stretching vulcanized (chemically cross-linked) rubber above the glass transition temperature results in the straightening of the polymer chains from their original, coiled configuration. The cross-links in the system, however, link the chains together and prevent them from slipping past each other to cause permanent, irrecoverable deformation [4]. During this stretching process, the aligning of the polymer chains significantly reduces the entropy (disorder) of the system.

In relating the stretching response of SMPs with the elastomeric behavior of vulcanized rubber, it is necessary to consider the chemically cross-linked SMP systems (types I and II) independent of the physically cross-linked SMPs (types III and IV). The chemically cross-linked SMPs are most directly comparable to vulcanized rubber, which is also chemically cross-linked. Therefore, the chemical cross-links (covalent bonds) act

as the net points, or physical entanglements, between which the polymer chains are extended by overcoming the secondary forces between individual polymer chains [11, 12]. In physically cross-linked SMP systems, on the other hand, these large deformations are possible below the melting temperature of the hard segment but above the glass transition temperature of the soft segment. In this temperature range, the crystalline or rigid amorphous hard segments serve as the net points between which the polymer chains are extended.

I.A.3.2. Cooling to Low Temperature ($T<T_{trans}$) and Unloading

In the second step of the thermomechanical cycle, the material is constrained (either by applying constant strain or constant force) while the temperature is decreased to below the transition temperature. Below the transition temperature, the polymer stiffens and prevents further large deformations. This stiffening is accomplished by different mechanisms for amorphous and semi-crystalline polymers.

In semi-crystalline polymers (types II and IV), the process of cooling causes the soft segment (regions between the net points) to form crystalline nuclei where the polymer chains become ordered (aligned) into periodic, unit cell configurations and do not have sufficient thermal energy to move. The continued growth of these crystalline regions throughout the polymer prohibits the long-range motion of the remaining amorphous regions [1, 2, 4, 11]. In purely amorphous (glassy) polymers (type I), the process of cooling causes the material to pass through the glass transition temperature.

During cooling through the T_g, thermal energy is removed from the system and the molecules do not have sufficient energy to significantly vibrate or translate [11].

Unloading the SMP after cooling results in a slight contraction, but the limited chain flexibility prevents significant long range motion of the chains. As a result of this lack of motion, the polymer is sometimes referred to as 'frozen' at temperatures below the glass transition temperature [4].

I.A.3.3. Heating to High Temperature ($T>T_{trans}$) for Recovery

After cooling and removing the external force, the final step of the thermomechanical cycle is to heat the polymer to above its transition temperature, either at zero load (free recovery) or at constant displacement (constrained displacement recovery).

In the free recovery case, the polymer will recover its original shape. The material is heated through its transition temperature and either crystalline regions melt (when $T_{trans} = T_m$) or the glass transition temperature is exceeded (when $T_{trans} = T_g$). In either case, the molecular motion is unimpeded and the polymer returns to its original configuration [1, 2]. The mechanism facilitating the return to its original configuration is two-part. The first part is because of the chemical or physical cross-links which help 'remember' (maintain) the original shape of the polymer. The second part is the entropy gain due to the regions between the cross-links returning to their original, coiled configuration.

In some polymer systems, there is irrecoverable deformation observed during the first thermomechanical cycle [1, 2, 4]. This irrecoverable deformation is due to local, microscopic rearrangements of the entanglements (physical and/or chemical cross-links) as compared to the pristine state of the polymer [13, 14]. During subsequent loading cycles, thermosetting polymer systems will often return to this new configuration with no, or very little, irrecoverable deformation; however, thermoplastic polymers may continue to develop additional irrecoverable deformations with each cycle [13].

In the constrained recovery case, the polymer will recover a tensile stress (if the original deformation was tensile) upon heating [1, 13]. If heating begins at a temperature well below the transition region, the stress will initially become compressive. This compressive stress is because the polymer wants to thermally expand upon heating but is kinematically constrained. Upon entering the transition region, the material will attempt to return to its original configuration for reasons previously discussed. Thus, the desire to return to the original configuration during heating results in a tensile stress on the polymer chains.

I.B. Applications of Shape Memory Polymers

The ability for shape memory polymers to recover large deformations, with tunable material properties and relatively low cost, has garnered significant interest in aerospace and biomedical applications. In the aerospace industry, concepts of using SMPs for morphing wings [10], active joints [15], or deployable space structures [16] has been investigated. However, the limitation of SMPs to withstand larger forces has

hindered their acceptance in aerospace applications. As a result, numerous efforts have focused recently on improving the material properties of SMPs through the fabrication of shape memory polymer composites and nanocomposites [17] or by improving the heating ability of the SMP through vascular means [18-38] or alternate energy sources [39].

On the other hand, shape memory polymers have found promise in biomedical applications, such as stents, thrombectomy devices, and tissue scaffolds, that often necessitate self-expansion, tunable material properties, biocompatibility, and/or biodegradability [25, 40-48]. Some devices that have been conceived and/or prototyped include artificial muscles [49-54], pressure bandages [55], and dialysis needles [56].

Perhaps the most commonly investigated biomedical applications are shape memory polymer stents, which have the potential for a better compliance mismatch with arterial walls compared to metallic stents as well as biocompatibility. As an example, Baer et al. [57] fabricated neurovascular stents from polyurethane shape memory polymers and demonstrated that they could be actuated using temperature or lasers. Recent efforts by Xue et al. [41, 58] and Yu et al. [59] have attempted to further tailor SMP stents by incorporating the ability for the stents to be drug-eluting or biodegradable, respectively.

In efforts to treat aneurysms, Maitland et al. [60] and Small et al. [43] have designed and prototyped light diffusers, shape memory polymer stents, and shape memory polymer foams, which can potentially be actuated using alternate sources of energy such as lasers of magnetic fields. Expanding the use of the alternate energy

sources as the driving force of actuation, additional efforts have been performed by Small et al. [44, 61] and Buckley et al. [45, 62] to prototype net-like and spiral-like thrombectomy devices that can recover their permanent shape without directly increasing the temperature.

I.C. Experimental Characterization

In the previous two decades, numerous experimental investigations have been performed to better understand and characterize the material properties and shape memory effect for new SMPs. Many of the initial studies focused on the SMP response when subjected to small deformations (<10% extension) [42]. In particular, Tobushi et al. tested polyurethane films to extensions of up to 10% [10, 63] under both free and constrained displacement recovery conditions. In these experiments, Tobushi et al. observed significant irrecoverable deformation (up to 4% when 10% strain applied) as well as relaxation in the rubbery phase at the start of the constrained cooling. In addition, Liu et al. tested the small deformation response in both free and constrained displacement recovery for an epoxy-based SMP [63]. In this epoxy system, complete recovery was observed for tensile and compressive extensions of up to 9.1%. In addition, the stress increase during cooling was observed to be the same independent of the applied strain, supporting the notion that this stress increase is primarily a response of the material undergoing a prescribed temperature change.

Recent experimental efforts have investigated in more depth the large deformation (>10% extension) response of SMPs, specifically polyurethane,

polystyrene, acrylic, and/or epoxy SMPs. The most commonly investigated type of shape memory polymers is polyurethanes, in part due to the tunable material properties, potential biocompatibility, and ability to fabricate as thermoplastic or thermosetting polymers. In [10], Tobushi et al. characterized thin films of a Mitsubishi® thermoplastic polyurethane SMP. In these experiments, extensions of up to 100% were applied, and the isothermal, viscoplastic, and free recovery behavior was characterized. The SMP was observed to exhibit significant creep strains during isothermal loading as well as large irrecoverable strains during the shape memory cycle. Expanding the investigation of the Mitsubishi® SMPs to include the thermosetting category, Baer et al. [64, 65] observed failure strains of up to 250% in the rubbery phase, isothermal strain recoveries of up to 94%, and shape recovery ratios of up to 85% in the first thermomechanical cycle. A parameter study was performed by Lin et al. [13] that demonstrated the effects of varying the hard segment in a polyurethane system. Specifically, for increasing amounts of the hard segment, a higher glass transition temperature was observed and a smaller ratio of the glassy modulus to the rubbery modulus. Recently, Azra et al. [66] performed a parameter study on the programming and recovery temperatures as well as the stress relaxation and storage times. They found that the time period for recovery could be tuned to occur over a broad time range, and they observed a tradeoff in the rate of shape recovery and the recoverable stress.

Improving on the shape recovery ratios and mechanical properties of the available polyurethane SMPs, Wilson et al. [67] proposed a new series of thermosetting polyurethane shape memory polymers based on aliphatic urethane networks. In this

work, the ability to modify the glass transition temperature and/or the rubbery modulus independently was highlighted, and the SMPs were observed to isothermally recover all of the applied deformation in the 2nd through 5th load/unload cycles. Recently, Volk et al. [68] performed free and constrained recovery experiments on one of the proposed compositions of [69, 70] and observed complete recovery in the first and second thermomechanical shape memory cycles on applied extensions of up to 25%.

In addition to the polyurethane SMPs, efforts by , Atli et al. [68] and Volk et al. [71] have been conducted on a commercially available polystyrene SMP. In these experiments, extensions of up to 100% were applied, and nearly all of the deformation was recovered under free recovery conditions. In addition, Atli et al. [72] characterized the constrained recovery response and observed a stress recovery of up to 0.17MPa for 75% extension. The work of Volk et al. [71] represented one of the first reported investigations of using digital image correlation as a non-contact technique for measure the displacement of the material. Recently, Schmidt et al. [72] performed cyclic experiments on a shape memory polymer called Tecoflex®, to which extensions of 50% and 225% were cyclically applied below the glass transition temperature, and the changes to the surface morphology were observed using scanning electron microscopy. In related efforts, Chowdhury et al. [73] tested the cyclic recovery of the Veriflex® SMP when programmed at 5°C above and below the glass transition temperature. Although both conditions showed a significant decrease in the recovery ratios as a function of cycles, an improvement was observed when programming 5°C above the glass transition temperatures as compared to 5°C below.

Focusing on acrylic SMPs, Yakacki et al. [74] fabricated shape memory polymers and injection molded the material into tubes representing simplified SMP stents, for which the unconstrained recovery was characterized. It was observed that a tube with machined holes initiated recovery faster than a solid tube although the same amount of time was required to finish recovery. Building upon the materials developed in [75], Srivastava et al. [75] performed isothermal tests at various temperatures and loading rates to characterize the mechanical response of the SMP. Recently, Voit et al. [76] have developed new materials that exhibited strain-to-failure values of up to 900% as well as complete recovery in a 200% free recovery experiment. In addition, Lakhera et al. [77, 78] recently performed experiments on methacrylate SMP networks with varying crosslink densities. In these experiments, the polymers were compressed at various temperatures and heated for recovery under constant stresses up to 1.5MPa.

For epoxy SMPs, recent studies by McClung et al. [79] have examined the rate and cycle dependence of the Veriflex®-E shape memory epoxy resin. In these experiments, the material was subjected to isothermal loading at different temperatures and different loading rates in addition to shape memory tests with different hold times and number of cycles. Additional experiments on composites fabricated from this series of epoxy resins as well as styrene resins have focused on quantifying the response of the SMPs and SMP composites when exposed to potentially degrading conditions [80, 81]. In another recent work, Song [82, 83] performed viscoelastic tests on a shape memory epoxy system with varying component ratios and observed the viscoelastic effects were

predominant near the glass transition temperature as compared to temperatures above or below the T_g.

In efforts to better improve the testing equipment and methods for the characterization of shape memory polymers, Volk et al. [84] and McClung et al. [69, 70, 72] have introduced non-contact techniques (digital image correlation and/or laser extensometers) to measure the displacement of the SMP undergoing free recovery. In [85], good agreement was observed in the measurements recorded by the digital image correlation method as compared to the laser extensometer. Further, in [85], Diani et al. has developed a torsion testing apparatus that can provide an alternate method for testing the large deformation response of SMPs. Additionally, [86] recently showed that a polyurethane shape memory polymer was capable of two way shape memory effect under a biasing load. In these experiments, the SMP was deformed above the melting temperature, cooled to between the glassy and melting temperatures, and then cycled under constant load to temperatures above and below the melting temperature. Finally, in [87], Li and Xu presented a new method to achieve the shape memory effect. Rather than deforming the material above the glass transition temperature, it was shown that the SMP could be deformed at temperatures below the glass transition temperature, held to induce stress relaxation, and then subsequently reheated to obtain the original shape.

I.D. Constitutive Modeling

In steps toward developing models for designing and analyzing SMP devices, there have been efforts to more accurately describe and predict the complex material behavior of SMPs. While the majority of the modeling efforts have been focused on the small deformation response of shape memory polymers, modeling efforts in the last five years have begun to emphasize and formulate the models in terms of large deformations.

I.D.1. Small Deformations

Initial models by Tobushi used rheological models with elastic, viscous, and slip elements to model the small deformation response of SMPs [88]. Recently, Bailin et al. [63, 89-91] performed a one-dimensional numerical study to verify the Tobushi constitutive model against the experimental data and found good agreement. Another rheological model was proposed by Lin and Chen [92], which used two Maxwell models in parallel with each Maxwell model representing a different phase (i.e., rubbery and glassy). The Maxwell models had unique relaxation times and thus accounted for the difference in relaxation times for each phase. Kohnakdar et al. [93] studied the recovery behavior of a polyurethane SMP by using a Voigt model in series with a damper. Using a Kelvin-Voigt model in combination with a transient stress dip test, Bonner et al. [94] demonstrated the ability to predict the recovery time for SMPs with recovery times less than 1000s. In addition, Srinivasa and Gosh [95] have proposed a three element rheological model with a dashpot threshold function accounting for the strain storage and release. This work was extended in [96] and observed to have good comparison

with the experimental data of Tobushi et al. [97] and Liu et al. [63] for applied strains up to 10%.

An internal variable approach was first utilized for SMPs in a small deformation framework by Liu et al. [10], who introduced a glassy volume fraction to account for the transformation between the rubbery and glassy phases and the associated stored deformation. Follow up efforts by Wang et al. [10], Zhou et al. [98] and Husson et al. [99, 100] extended the work of Liu et al. to account for rate dependency of the glassy volume fraction, viscous strains, and the temperature dependence of the elastic modulus, respectively. An effort by Gilormini and Diani [101] further investigated the assumption of constant stress between the two phases in [102] and found that assuming constant strain in the two phases could also lead to good model predictions. In addition, Kim et al. [10] used a similar approach to develop one-dimensional equations that were implemented in a user material subroutine to model braided SMP polyurethane stents comprised of simple beam elements.

Recent efforts by Baghani et al. [103] have followed a similar approach to [104, 105] with an additive decomposition of the strain into the rubbery phase elastic, glassy phase elastic, glassy phase stored, and thermal strains. The model was thermodynamically motivated with evolution equations for the glassy volume fraction during both cooling and heating. The model was subsequently implemented in a user material subroutine in Abaqus with the material properties, including heat transfer properties, calibrated from the data of Diani et al. [10], Liu et al. [86], and Volk et al. [10]. Subsequent model predictions were shown to match well with experimental data,

and the shape memory profile of the extruded and perforated stent in [72] was modeled. Further efforts by Baghani et al. [75] used the model to perform semi-analytical studies of helical springs fabricated from shape memory polymers. The semi-analytical results were shown to match well with the finite element solutions.

I.D.2. Large Deformations

Considering large deformations, there have been two general approaches in the literature. The first approach is to model the SMP using temperature dependent material properties, such as relaxation times. The other approach is to use an internal variable approach, similar to that proposed by Liu et al. [106], to evolve the volume fraction of a phase. In the first approach, Diani et al. [10] introduced a model that accounted for viscoelastic deformation and thermal expansion. The expression for the entropy was inspired by rubber elasticity, and an evolution equation was proposed to account for the viscous deformation. Another approach to modeling SMPs was introduced by Nguyen et al. [107], which assumed the shape memory effect was due to a combination of structural and stress relaxation mechanisms. In other words, they assumed the shape memory effect was due to the notion that the SMP could relax back to its original state in the rubbery phase but not in the glassy phase. Thus, the SMP was modeled using temperature dependent relaxation parameters and a fictive temperature to track when the SMP was in a non-equilibrium state. Similar approaches have also been used to model by Westbrook et al. [108-110] to model the behavior of semi-crystalline shape memory polymers, some of which may undergo stretch induced crystallization. A recent model

was proposed by Srivastava et al. [111, 112], which posed a general formulation that provides the framework and methodology to account for an arbitrary number of deformation mechanisms. The free energy is assumed to be an additive decomposition of each mechanism, and an evolution equation must be defined for each separate mechanism. The model was implemented in finite elements for the case of three deformation mechanisms and thermomechanical coupling.

In the second classification of large deformation models for SMPs, multiple efforts have used a similar approach to Liu et al. [76]. One effort was that of Chen and Lagoudas [10], which modeled the SMP as a system in which the glassy phase was nucleated from the rubbery phase and the deformation in each the rubbery and glassy phases was taken to be thermoelastic. This model has been implemented in 1-D by Volk et al. [113, 114] and shown to have good comparison of the model predictions with experimental results for polystyrene and polyurethane thermosetting shape memory polymers. Another effort, by Qi et al. [69, 70, 115], considered the SMP a combination of a rubbery phase, a frozen glassy phase (transformed from the rubbery phase), and an initial glassy phase. The deformations in the rubbery and glassy phases were described by the thermoelastic (Arruda-Boyce) and viscoplastic models, and evolution equations were posed for the glassy volume fractions and the viscoplastic strains. Reese et al. [116] recently took a similar approach by defining contributions to the free energy for each the rubbery and glassy phases and an evolution equation for the glassy volume fraction. The work of Reese et al. also introduced a method to model SMPs using

individual tetrahedral cells and incorporated thermomechanical coupling using Fourier's Law.

I.D.3. Current Modeling Approach

In this work, a large deformation approach is used to model the response of the shape memory polymers. This modeling approach is an extension of the kinematic framework proposed by Chen and Lagoudas [117], which provides a phenomenological representation of the shape storing and recovery behavior of SMPs. Specifically, this modeling effort considers the SMP phase transition as a nucleation phenomenon. As such, it is assumed the material is initially completely in a discrete 'rubbery' phase and the material smoothly transforms over a range of temperatures to a discrete glassy phase. During this cooling, it is assumed the glassy regions nucleate until all rubbery phase regions cease to exist. This kinetic phase transition approach is used to account for the changes in the material properties that occur during cooling from high temperatures to lower temperatures. However, it is noted that the molecular structure of the SMP is not physically changing during this transition but rather the ability for the molecular chains to undergo large-scale conformational motion is restricted upon cooling to below the glass transition temperature.

In addition, this work considers only the thermoelastic response of the rubbery and glassy phases. That is, no permanent irrecoverable deformations, strain- or temperature-rate dependent effects of the SMP behavior are considered. The choice to focus on the rate-independent elastic response generally limits this modeling approach to

considering highly crosslinked thermosetting polymers, such as the thermosetting polyurethane that is the focus of the experimental portion of this work. In these covalently crosslinked SMPs, a more uniform molecular network is formed and the irrecoverable deformation and viscoplastic response is generally minimal compared to physically crosslinked systems.

I.E. Summary of the Dissertation

This dissertation builds on the existing efforts in the literature, the number of which have increased rapidly in the previous two decades, which aim to focus on understanding and predicting the behavior of shape memory polymers. This dissertation, which will focus on the experimental characterization and modeling of thermosetting shape memory polymers, is organized as follows.

In Chapter II, experiments are performed on a relatively new thermosetting shape memory polymer that is being considered for use in biomedical applications. In this chapter, the details of the material fabrication, experimental setup, and test methodology and results are presented. This investigation provides further evidence of the necessity of non-contact measurement techniques to accurately measure the displacement of the material during the constrained cooling and recovery steps. As part of this work, free recovery and constrained displacement recovery experiments are performed, for which the conventional thermomechanical path is modified to avoid undesired influence due to the grips.

In Chapter III, a large deformation constitutive model for shape memory polymers is implemented in a 1D framework. The model is formulated such that the material is assumed to be a mixture of the glassy and rubbery phases, and each phase behaves as an incompressible neo-Hookean material. In addition, a functional form for the glassy volume fraction is introduced to represent the portion of the material in the glassy phase at any temperature, and an assumption is made considering the rotations in the rubbery and glassy phases. This implementation is performed in a general manner to allow for prediction the response of the SMP for load paths in which the stress or the displacement of the material is known. The model is calibrated from the uniaxial experiments of Chapter II, and subsequent model predictions are shown to compare well with the remaining uniaxial shape memory experiments.

In Chapter IV, the implementation of Chapter III is expanded to three dimensions as part of a user material subroutine in Abaqus. Providing more versatility, the constitutive equations for each phase are now modeled as compressible neo-Hookean materials, and an evolution equation is introduced for the recovery heating. The material properties are calibrated from the experiments of Chapter II, and then a series of boundary value problems are analyzed. Coupled temperature-displacement analyses are performed to evaluate the effects of applying various thermal boundary conditions and/or temperature rates.

CHAPTER II

EXPERIMENTAL CHARACTERIZATION*

An introduction to the shape memory effect and the relevant experimental and modeling works in the literature was presented in Chapter I. This chapter presents the details of the experimental effort to characterize a previously untested polyurethane shape memory polymer. In particular, the experimental parameters and results are presented for the experiments that obtain the basic material properties as well as the experiments that characterize the shape memory capability of the material.

II.A. Materials and Methods

This section presents the fabrication procedure for creating the polyurethane SMP as well as details of the experimental parameters and setup used for characterizing the resulting material.

II.A.1. Specimen Type and Preparation

The shape memory polymer used for this study was a polyurethane SMP proposed by Wilson et al. [113], which consisted of 1,6-hexamethylene diisocyanate

---

*Part of this chapter is reprinted with permission from "Characterizing and Modeling the Free Recovery and Constrained Recovery of a Polyurethane Shape Memory Polymer" by Volk, B.L., Lagoudas, D.C., and Maitland, D.J., 2011. *Smart Materials and Structures*. **20**, 094004, DOI: 10.1088/0964-1726/20/9/094004, Copyright 2011 by IOP Publishing Limited.

(HDI), N,N,N0,N0-tetrakis(2-hydroxy-propyl)ethylenediamine (HPED), and triethanolamine (TEA). In [68], Wilson et al. demonstrated the glass transition temperature of the polymer could be varied, as a function of the molar ratios of the monomers, from approximately 35°C to 85°C while maintaining similar (but shifted with respect to T_g) trends in the shear modulus and tan delta as a function of temperature. As a result, this work selected an intermediate composition, of which the respective molar amounts of HDI, HPED, and TEA were 1.00, 0.40, and 0.133, and the glass transition temperature was nominally 76°C – measured by differential scanning calorimetry (DSC) with a temperature rate of 20°C/min [68].

The method for fabricating the thermoset polyurethane SMP was adapted from [68]. The monomers were first decanted from source containers to 60mL glass containers and then subsequently vacuum degassed for 24 hours at 45°C. The monomers were weighed on a Mettler Toledo® PB403-S scale and combined in a Labconco® Precision Basic Glovebox to reduce exposure to moisture. After removing the combination from the glove box, the monomers were mixed using a VWR® Analog Vortex Mixer for 2 minutes. The mixture was sonicated for 2 minutes and vacuum degassed for 6.5 minutes. The mixture was then sonicated again for 3 minutes and then vacuum degassed again for 3 minutes.

The mixture was then cast into an aluminum mold to create a sheet of the polymeric material. The mold was designed to produce a sheet of material that would accommodate the fabrication of ASTM D638 [68] Type V specimens. Type V specimens with a thickness of 1mm were selected (i) to maximize the number of defect-

free sample that could be obtained from a sheet of material (compared to Type IV specimens), and (ii) to result in stresses that would not exceed the capacity of the available load cell. The resulting mold design is shown in Figure 2, and has two aluminum pieces. One h has a cavity with a depth of 2mm and the other piece has an extrusion of 1mm. Upon placing the two pieces in contact, the effective cavity depth is reduced to 1mm while helping to create a seal around the edges of the cavity. Further, two ports are machined into the mold – one for injecting the polymer solution and one for allowing the trapped air to escape during injection.

After fabrication, the aluminum mold was coated with a polytetrafluoroethylene (PTFE) spray, which was sintered on the mold and served to aid in releasing the polymer from the mold. The mold was sealed using a VersaChem® Type 613 silicone gasket between the two pieces, and then was positioned vertically in a clamp. Stopcocks, of which the tips were wrapped with a PTFE tape to provide a better seal, were placed into the tapered ports of the mold, and quick-setting epoxy was used to hold the stopcocks in place during the casting process. Figure 2(a) presents the mold setup ready for casting the polymer. The polymer mixture was injected into the bottom port of the mold using a syringe and tubing which attached to the stopcock via a Luer connection and air was allowed to escape through the top port of the mold. The mold and clamp setup was then placed in a VWR® 1430M temperature chamber that was controlled by a Cole-Parmer® Digi-Sense Temperature Controller R/S. The temperature profile was programmed to heat at 30°C/hour to 120°C, at which the chamber was held constant for an hour before slowly cooling to room temperature. The fabrication process resulted in sheets of

polymer material that measured 6in. x 4in. x 1mm thick. A GravoGraph® LS100 CO_2 laser cutter was used to cut nine ASTM D-638 Type V specimens from each sheet of

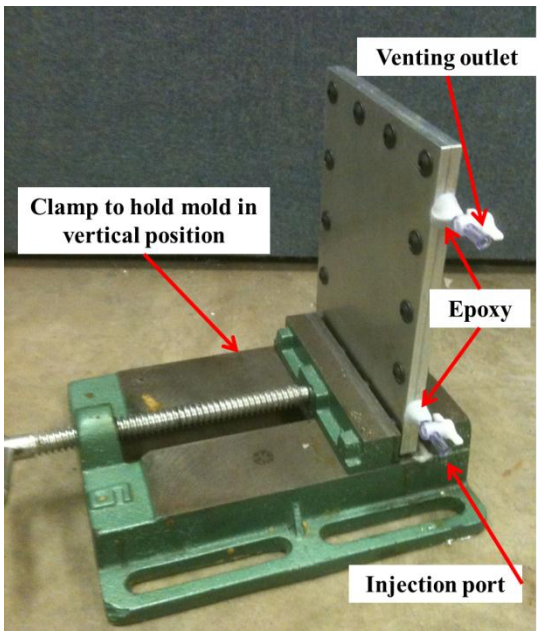

(a)

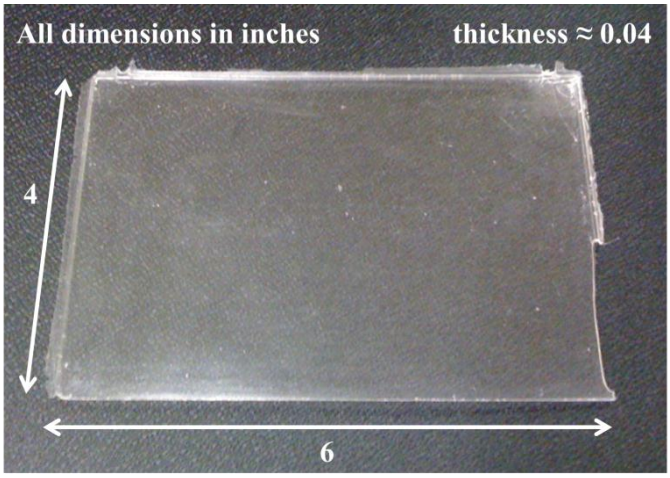

(b)

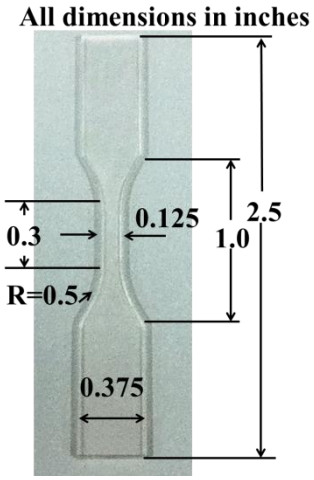

(c)

Figure 2 – (a) Mold setup used to fabricate the polyurethane SMPs. The SMP resin is injected through the bottom port. (b) A resulting sheet of shape memory polymer, after curing in an oven. (c) An ASTM Type V dogbone sample, which was laser cut.

material. A sheet of material and a resulting Type V specimen are shown in Figure 2(b) and (c), respectively.

II.A.2. Experimental Parameters

The experiments performed in this work focus on obtaining the basic material properties in addition to the shape memory response of a thermosetting polyurethane SMP. Through determining the basic material properties, the thermomechanical load path parameters for the shape memory experiments are determined.

II.A.2.1. Thermal and Mechanical Characterization

Experiments were performed to obtain the material properties, such as the glass transition temperature, the modulus in the rubbery and the glassy phases, and the strain to failure in the rubbery phase. These properties were obtained by performing experiments that included Differential Scanning Calorimetry (DSC), Dynamic Mechanical Analysis (DMA), ThermoMechanical Analysis (TMA) and isothermal tensile testing.

II.A.2.1.1. Differential Scanning Calorimetry

Differential scanning calorimetry tests were performed on a TA Instruments Q200 machine to obtain the glass transition temperature. Three samples were tested from each sheet of polyurethane SMP that was fabricated. Each sample was subjected to

two cycles in which the temperature was cycled from -40°C to 150°C. The temperature rate for both cycles was 1°C/min.

In addition, a preliminary experiment was performed to obtain an estimate of the effects of the temperature rate on the measured T_g. In this experiment, a single sample was subjected to five consecutive cycles, with the heating rate increasing from 1°C/min to 5°C/min in increments of 1°C/min.

II.A.2.1.2. Dynamic Mechanical Analysis

Dynamic mechanical analysis tests were performed on a TA Instruments Q800 machine to obtain the rubbery modulus, the glassy modulus, and the glass transition temperature. Three samples were tested from each sheet of polyurethane SMP that was fabricated. Each sample was subjected to one cycle in which the temperature was raised from 0°C to 120°C. The heating rate was 1°C/min. The glassy and rubbery moduli were measured at room temperature (25°C) and high temperature (90°C), which were located in the plateau regions for the respective phases.

II.A.2.1.3. Thermomechanical Analysis

Thermomechanical analysis tests were performed on a TA Instruments Q400 machine to obtain the coefficients of thermal expansion in the rubbery and glassy phases. A sample from each batch of polymer fabrication was subjected to one cycle in which the temperature was raised from 0°C to 120°C. The heating rate was 1°C/min. The coefficients of thermal expansion in the glassy and rubbery phases were calculated

as the slopes of the linear dimension change vs. temperature data from 20°C to 50°C and 85°C to 105°C, respectively.

II.A.2.1.4. Tensile Testing

Isothermal tension tests were performed on a MTS® Insight 30kN electromechanical, screw-driven test frame equipped with a Thermcraft® temperature chamber that uses forced convection for heating and liquid nitrogen for cooling. The test frame was equipped with MTS® Advantage 2kN pneumatic grips and a Honeywell® 222 N (50 lbf) load cell. To avoid undesirable effects of a contact-based measurement technique [118], a MTS® LX1500 laser extensometer was used to measure the extension of the material. Figure 3 presents the test frame, temperature chamber, and laser extensometer used for testing the shape memory polymers. To prepare the specimens for use with the laser extensometer, two pieces of reflective tape were attached, at the ends of the gauge region, to the surface of the specimen. Six specimens, including three that were lightly polished on the edges using sandpaper after CO_2 laser cutting, were strained to failure at 90°C ($T \approx T_g + 30°C$) to determine the extensibility of the rubbery phase. The extension of the material was calculated as the change in the distance between the reflective tapes divided by their initial separation.

II.A.2.2. Shape Memory Characterization

Shape memory tests were performed on ASTM Type V specimens, of which the fabrication was presented in Figure 2. The experiments were conducted using the experimental setup used for isothermal tensile testing in Figure 3.

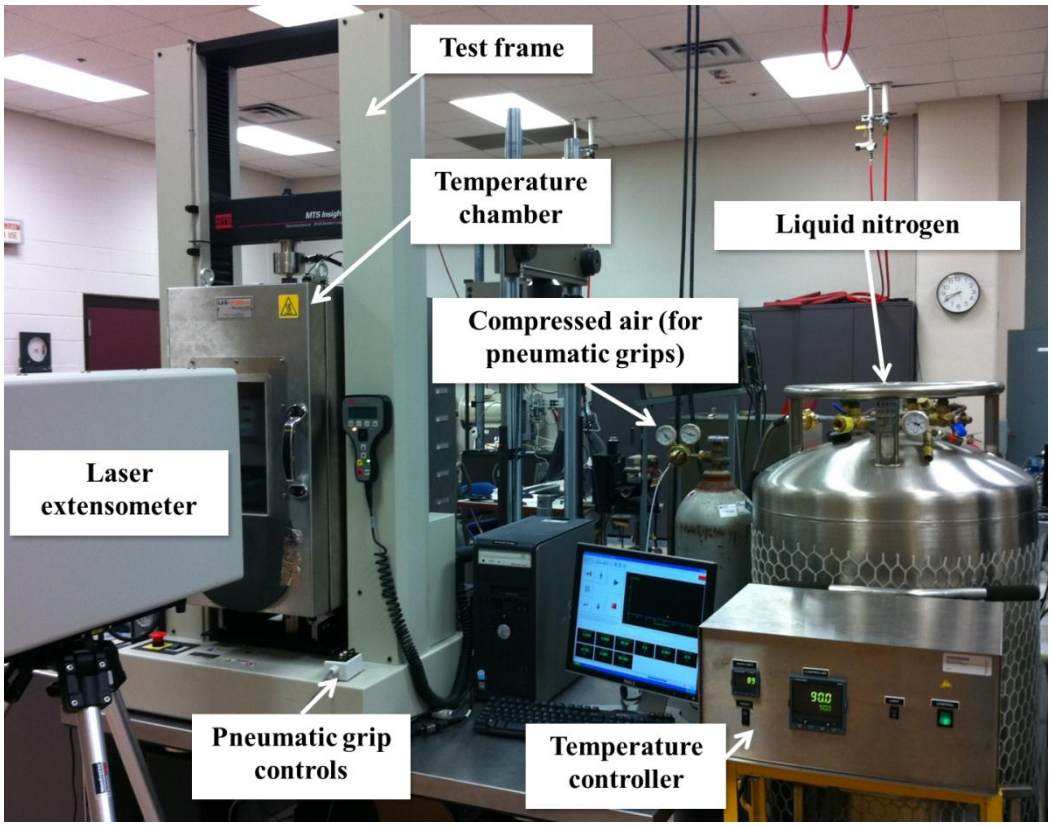

Figure 3 - Experimental setup used for testing the shape memory polymers.

II.A.2.2.1. Thermomechanical Load Path

The experiments performed in this work evaluated both the free recovery (extension recovery at zero load) and the constrained displacement recovery (stress recovery at constant extension) of the SMP. The free recovery experiments were performed to determine the maximum shape recovery, and the constrained displacement recovery tests were performed to provide information (e.g., blocking stress) about the response of the SMP while subjected to external constraints. The tests primarily followed the thermomechanical load path presented in Figure 1 for free and constrained recovery conditions. First, the specimens were held at zero load and the temperature

was increased to 90°C, which was higher than the glass transition temperature that was measured by DSC. The temperature was held at 90°C for 25 minutes to allow the system to reach thermal equilibrium. Zero load was maintained during the heating and dwell periods by keeping the bottom grip released.

The bottom of the material was then gripped and the sample was subsequently deformed at 50mm/min – the displacement rate recommended for nonrigid materials by the ASTM D638 standard for testing tensile properties of plastics [69-72, 85]. Although larger values of extension may be possible by deforming at temperatures near T_g [118], this loading temperature was selected to evaluate the material response of the rubbery phase at temperatures above the glass transition region. The temperature was then decreased to 25°C. During the cooling step, the laser extensometer measurements were used as feedback to the proportional-integral-derivative (PID) controller in the MTS® Testworks® software to adjust the crosshead to minimize the extension induced in the specimen by the thermal contraction of the grips and extension rods. The temperature was held at 25°C for 25 minutes to allow the system to reach thermal equilibrium. Figure 4 shows the temperature for a thermocouple near the center of the chamber compared to the temperature for a thermocouple on the surface of the grip as a function of time. Note that the thermocouple in the center of the chamber reaches the desired temperatures (25°C) at approximately 32 minutes. After approximately 15 minutes, the grip temperature is within 3°C of the chamber temperature.

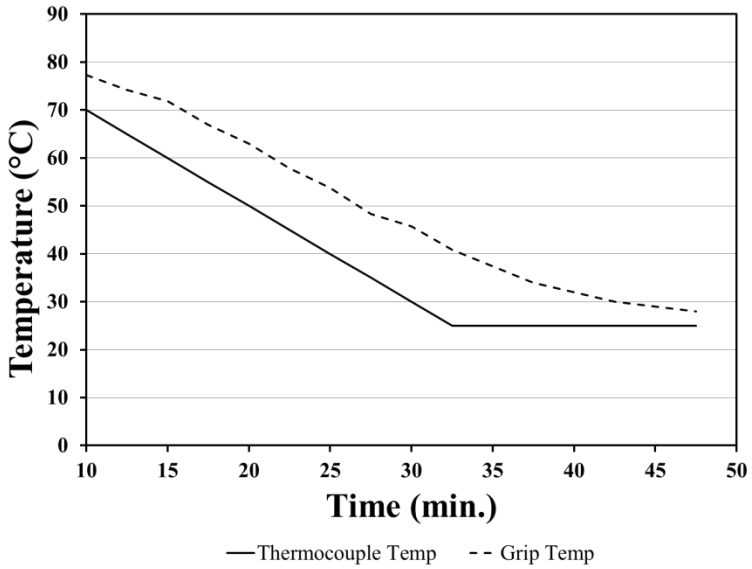

Figure 4 – Comparison, during cooling to 25°C at 1°C/min, of the temperature readings from the thermocouple placed in the center of the oven and the thermocouple placed on the surface of the pneumatic grip.

After reaching thermal equilibrium at 25°C, the displacement was decreased at 5 mm/min – the rate recommended by ASTM D638 for rigid materials [78, 119] – until the load equaled zero. The temperature was again raised to 90° and the recovery was measured. For the free recovery experiments – the bottom grip was opened after unloading and the specimen was again allowed to hang freely from the top grip to ensure zero applied load.

II.A.2.2.2. Modification to Constrained Recovery Step

This work also introduced a modification to the constrained displacement recovery presented in Figure 1. In preliminary tests, the standard thermomechanical step was used, in which specimen was held gripped and the displacement was maintained

constant during the entire heating procedure. However, it was observed that the specimen was subjected to thermal buckling in the glassy phase due to the thermal expansion of the grips and extension rods as well as the constrained thermal expansion of the specimen. Figure 5 presents the observed out-of-plane motion for an undeformed specimen that is heated, at constant displacement, from the glassy phase to the rubbery phase. Thus, to alleviate this out-of-plane motion, the step was modified such that the specimen was allowed to hang freely from the top grip during the first part of the heating step. Before the specimen reached the transition temperature range and initiated shape recovery, the bottom grip was again closed. The displacement was then held constant and the remainder of the heating step was completed.

II.A.2.2.3. Shape Memory Test Matrix

Table 1 presents the test matrix that summarizes all of the shape memory tests performed on the polyurethane SMP. In particular, the SMP was tested at extensions of 10%, 15%, 20%, and 25% for each of the free recovery and constrained recovery conditions. The 25% extension upper limit was observed to be the largest value for which shape memory tests could be repeatability performed. This value of extension, although lower than recently developed high-strain SMPs [118], is a result of the trade-off for developing a high recovery force SMP with a rubbery modulus greater than 20 MPa [77, 78] and is considered appropriate for the devices under consideration. It is noted that this value is lower than the average elongation to failure presented in the upcoming results section. As such, larger extensions may be possible for shape memory

characterization by further optimization of the fabrication and processing conditions, which was not a focus of this work.

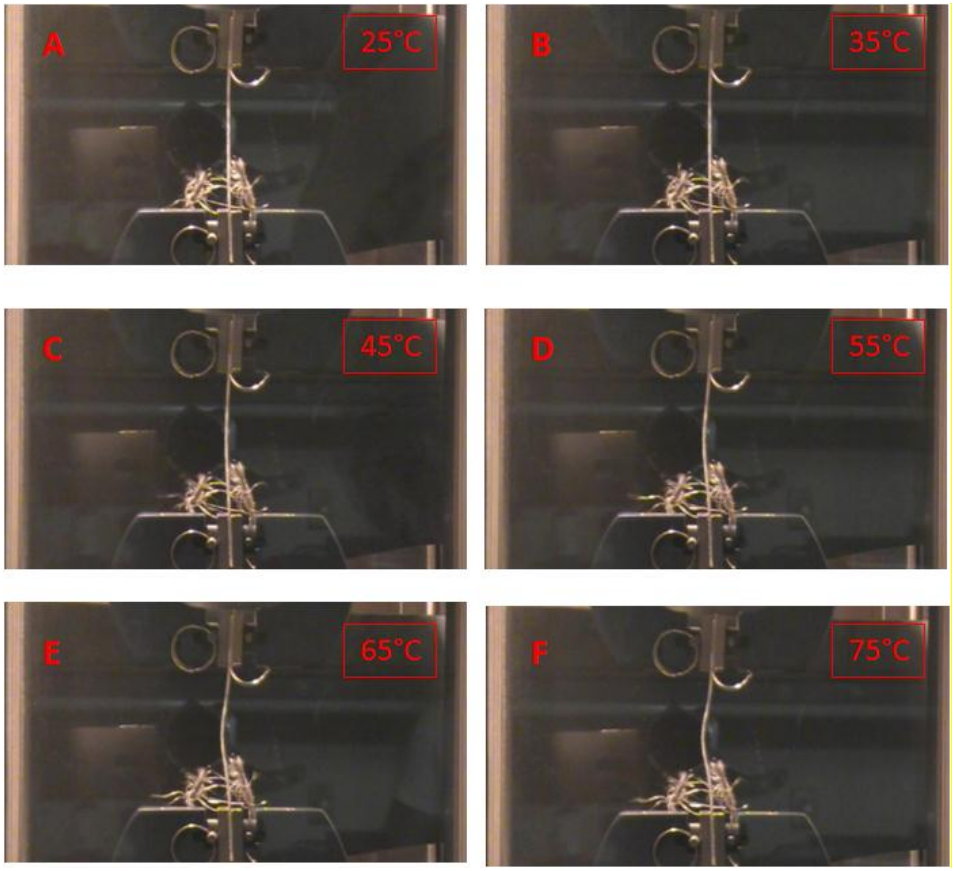

Figure 5 – Observation of out-of-plane deformation while heating an undeformed specimen from 25°C to 90°C. Buckling is induced due to the thermal expansion of the specimen, the grips and extension rods, and the constraint that holds the crosshead fixed during heating.

The temperature rate, the rate of heating and cooling, was 1°C/min for all tests to minimize the temperature rate effects [68]. A pristine specimen was used for each experiment and each specimen was subjected to two cycles under the same parameters. The tests were repeated twice for a total of three specimens (2 cycles per specimen) per

test condition. Additional cycles were not performed after observing negligible change in the shape memory response from the first to the second cycle and based on isothermal results [72] that indicate the largest hysteresis may occur as a result of loading in the first cycle with stable material response beginning in the second cycle.

Table 1 – Test matrix of free (zero load) and constrained displacement recovery experiments performed on polyurethane shape memory polymer. Applied strains were increased from 10% to 25%. Three specimens were tested for each load case, and each specimen was subjected to two thermomechanical cycles.

Applied Strain	Loading Strain Rate	Heating/ Cooling Rate	Recovery Temperature	Recovery Stress (MPa)	Recovery Strain
Free recovery (zero load recovery) experiments					
10%	50mm/min	1°C/min	90°C ($T \approx Tg + 30$)	$\sigma = 0$	**Output**
15%					
20%					
25%					
Constrained displacement recovery experiments					
10%	50mm/min	1°C/min	90°C ($T \approx Tg + 30$)	**Output**	10%
15%					15%
20%					20%
25%					25%

II.B. Results

The results from the experimental characterization of the thermosetting polyurethane SMP are presented in this section. Representative results from the experiments are shown; however, where applicable, the discussion and/or tables provide more information on the repeatability and variation in the resulting data for each type of experiment that was performed in duplicate or triplicate.

II.B.1. Thermal and Mechanical Characterization

The first results presented in this section are from the experiments that were performed to obtain the basic material properties, including the glass transition temperature, the rubbery and glassy tensile modulus, and the coefficients of thermal expansion.

II.B.1.1. Differential Scanning Calorimetry

The DSC experiments were performed such that each sample was subjected to two heat/cool cycles from -50°C to 150°C. The average glass transition temperature during the first heating cycle was 61.6°C with a standard deviation of 2.2°C (7.3% of the average). During the second heating cycle, the average glass transition temperature was 67.1°C with a standard deviation of 0.7°C (1.2% of the average). A result from the second heating cycle of a DSC experiment is presented in Figure 6, in which the glass transition temperature is measured as the inflection point of the change in the heat capacity as the material transforms from the glassy to the rubbery phase.

Upon increasing the temperature rate from 1°C/min to 5°C/min, the glass transition temperature was observed to increase from 66.0°C at 70.8°C. These results indicate a trend that indicates agreement with the T_g of 75.7°C measured by Wilson et al. when a temperature rate of 20°C/min. was used [68].

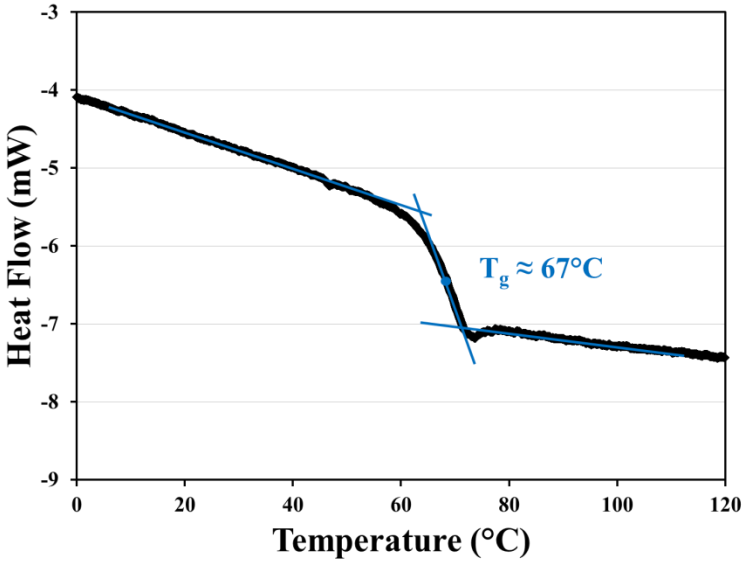

Figure 6 – Differential scanning calorimetry result on the polyurethane shape memory polymer when heated from -50°C to 150°C at 1°C/min. The glass transition is calculated, from the inflection point in the data shift, to be approximately 67°C.

II.B.1.2. Dynamic Mechanical Analysis

A result from a DMA experiment is shown in Figure 7, in which the specimen was heated from 0°C to 120°C at a heating rate of 1°C/min. Three samples were tested from each batch of polymer that was fabricated. The average glass transition temperature, as measured by the peak of the tan δ curve, was 84.5°C with a standard deviation of 1.6°C (1.9% of the average). The rubbery plateau modulus, measured at 100°C, was 20.6 MPa with a standard deviation of 0.33 (1.6% of the average). In addition, the glassy plateau modulus, measured at 25°C, was 2454 MPa with a standard deviation of 139 MPa (5.7% of the average).

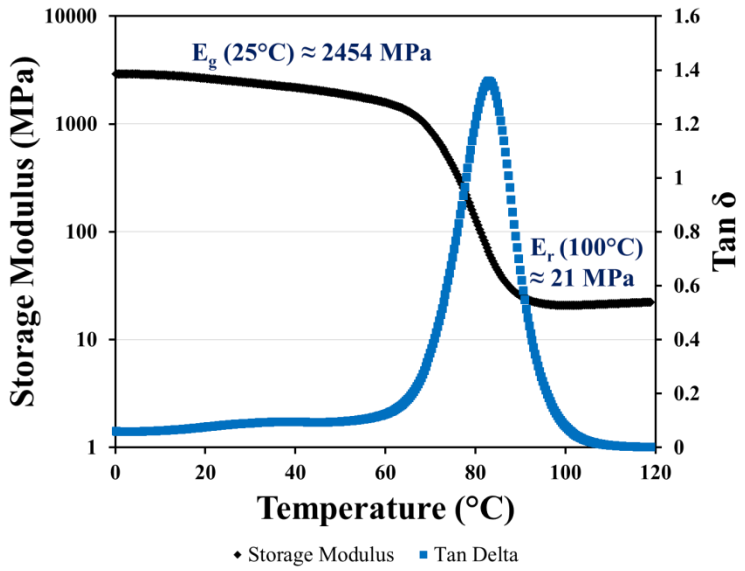

Figure 7 – Dynamic mechanical analysis result on the polyurethane shape memory polymer when heated from 0°C to 120°C at 1°C/min. Presented is the storage modulus (black data points) and the tan δ (blue data points). The glassy and rubbery storage moduli are calculated as approximately 2500MPa and 21MPa, respectively.

II.B.1.3. Thermomechanical Analysis

The TMA experiments were conducted, on one specimen from each batch of polymer that was fabricated, to measure the coefficients of thermal expansion (CTEs) in the glassy and the rubbery phases. Figure 8 presents a representative result, in which the sample was heated from 0°C to 120°C at a heating rate of 1°C/min. The average glassy CTE, calculated from the linear displacement vs. temperature data from 20°C to 50°C, was 7.9E-5 (mm/mm)/ °C with a standard deviation of 5.1E-5 (mm/mm)/ °C (6.5% of the average). Similarly, the average rubbery CTE, calculated from the linear displacement vs. temperature region from 85°C to 105°C, was 2.1E-4 (mm/mm)/°C with a standard deviation of 2.9E-4 (mm/mm)/ °C (1.4% of the average).

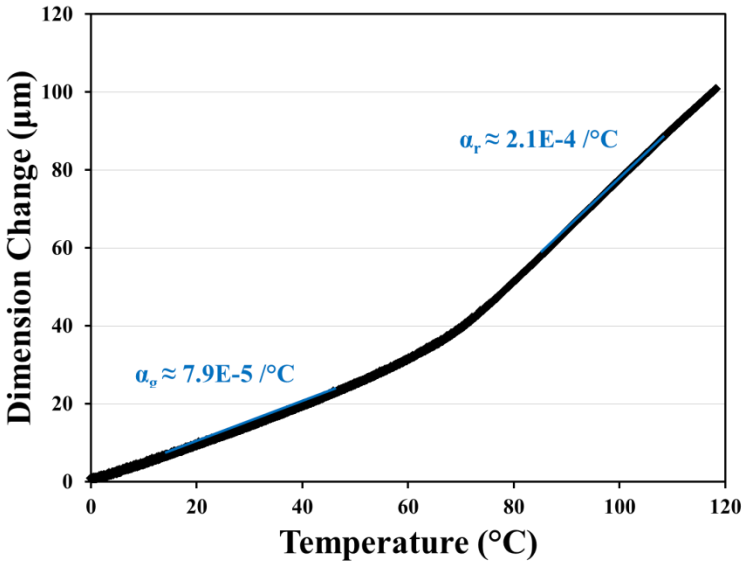

Figure 8 – Thermomechanical analysis result on the polyurethane shape memory polymer when heated from 0°C to 120°C at 1°C/min. The glassy and rubbery coefficients of thermal expansion are calculated from the linear regions to be approximately 7.9E-5/°C and 2.1E-4/°C, respectively.

II.B.1.4. Tensile Testing

The results from the isothermal tensile testing at 90°C are presented in Figure 9. The elongation to failure ranged from 0.37mm/mm to 0.59mm/mm with an average of 0.48mm/mm. The corresponding stresses at failure ranged from 6.4 MPa to 12.6 MPa with an average of 9.9 MPa. It is observed that the rubbery phase stress-strain response of all specimens is approximately linear during deformation to failure. In addition, there was no distinguishable improvement in the failure strains of the polished specimens as compared to the unpolished specimens.

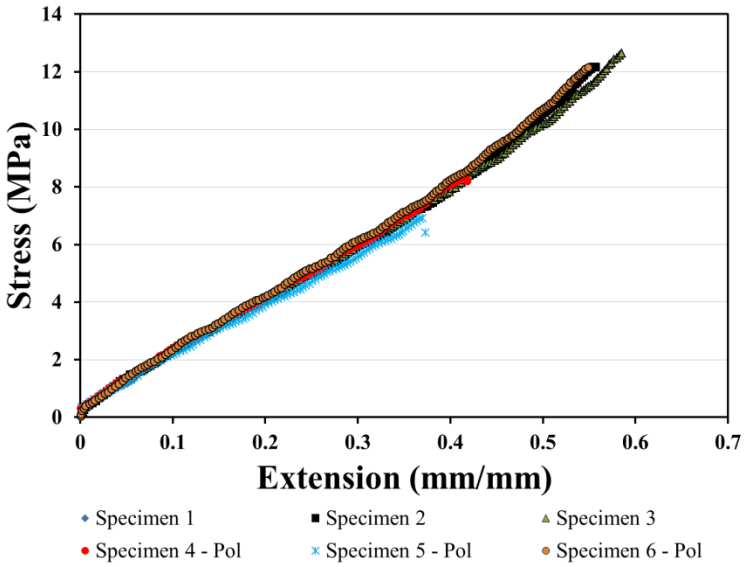

Figure 9 – Elongation-to-failure results for six polyurethane samples. The maximum extension ranged from 0.37mm/mm to 0.59m/mm with an average of 0.48mm/mm.

II.B.2. Shape Memory Characterization

This section presents the results for the free recovery and constrained displacement recovery experiments that were tested at extensions of 10%, 15%, 20%, and 25%. A single, complete result for each of the test cases is presented first, in figures 3 and 4. The data corresponding to the individual segments of the tests, including the samples tested for repeatability, are then presented in greater detail in Sections 2.1 - 2.3. Note that Sections 2.1 and 2.2 present the data for segments that are common to all tests performed (loading at high temperature, constrained cooling, and unloading at low temperature). Section 2.3 presents the data for the two different types of recovery steps – free (zero load) recovery (Section 2.3.1) and constrained displacement recovery (Section 2.3.2).

To begin, consider the results presented in Figure 10 and Figure 11, where the temperature, extension, and stress are plotted with respect to time and the key steps of the thermomechanical load path are labeled as ‘A’, ‘B’, ‘C’, and ‘D’. The reference temperature for each test was 90°C, at which the temperature was held constant for 25 minutes to allow the system to reach thermal equilibrium. During this dwell period, each specimen was allowed to hang freely from the top grip at zero load. At the end of the dwell period, denoted by point ‘A’, the load and extension readings were zeroed and the bottom of the specimens was gripped using the handheld pneumatic controls. The gripping procedure often resulted in a small, compressive force, and thus a non-zero extension at the beginning of loading on the specimen. The specimens were then stretched to a predetermined value of extension, specifically 10%, 15%, 20%, or 25%. After loading the extension was constrained and the temperature was lowered to 25°C. A stress increase was measured during this constrained cooling step from ‘A’ to ‘B’. The temperature was then held at 25°C for 25 minutes to allow the system to reach thermal equilibrium, which coincides with the plateau in the stress profile. The additional increase in stress from ‘B’ to ‘C’ after cooling is complete is likely due to continued cooling of the grips and extension rods, which results in additional elastic stress imposed on the SMP [68]. The load is then removed at time ‘C’ and the recovery step is initiated.

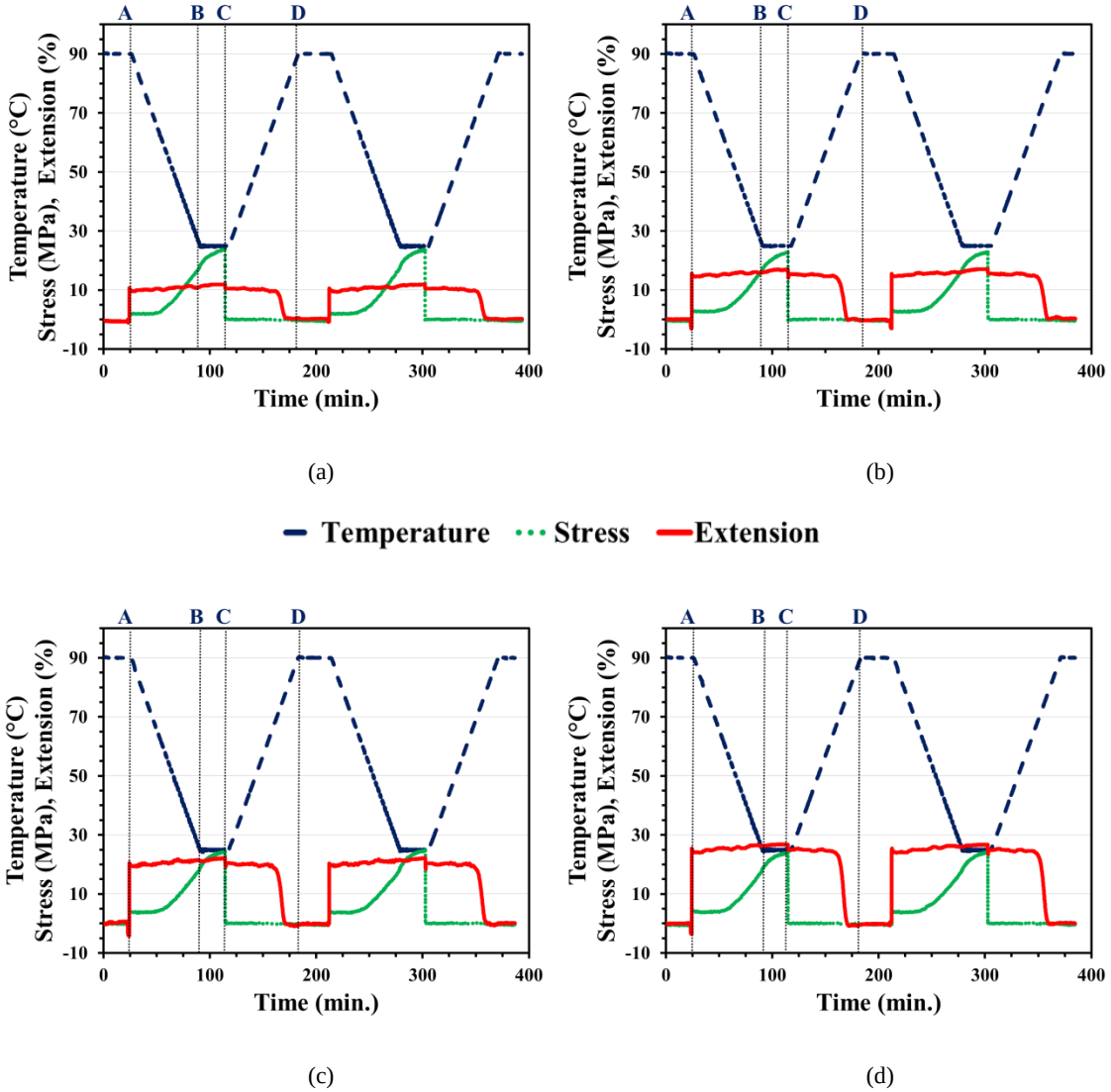

Figure 10 - (a) 10%, (b) 15%, (c) 20%, and (d) 25% free recovery experiments performed with a temperature rate of 1°C/min. Two shape memory cycles per test were performed, and the data for both cycles is presented with respect to time.

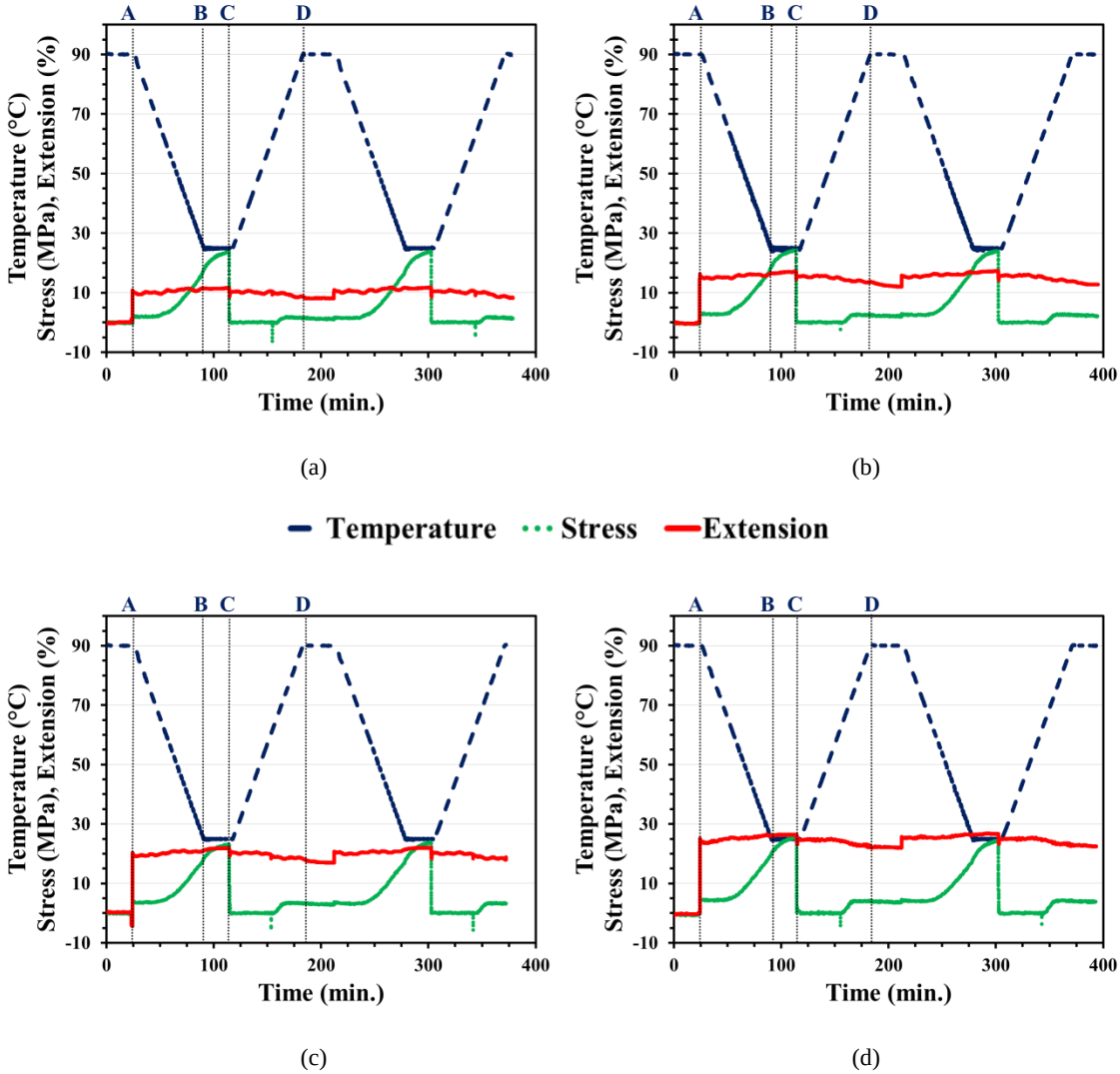

Figure 11 - (a) 10%, (b) 15%, (c) 20%, and (d) 25% constrained displacement recovery experiments performed with a temperature rate of 1°C/min. Two shape memory cycles per test were performed, and the data for both cycles is presented with respect to time.

At the beginning of the recovery heating in the free recovery experiments (cf. Figure 10), the bottom grip was released using the handheld pneumatic controls. By releasing the grip, zero load was maintained on the specimen, neglecting gravity. The temperature was then raised to 90°C, and the extension (shape) recovery was measured using the laser extensometer from 'C' to 'D'. After a 25 minute dwell period at 90°C, the bottom of the specimen was re-gripped, and the thermomechanical cycle was repeated.

In the constrained recovery experiments (cf. Figure 11), the bottom grip was released at the beginning of the recovery step, denoted by time 'C'. Releasing the bottom grip ensured zero load during the beginning of the recovery heating; otherwise, the thermal expansion of the SMP combined with the thermal expansion of the grips and extension rods could have created a significant compressive stress and the potential for thermal buckling in the SMP [69, 72]. At 60°C, before shape recovery would initiate, the bottom of the specimen was re-gripped. This gripping procedure resulted in a small, compressive force on the SMP. To offset this force, the crosshead was moved slightly up using the handheld control of the MTS® test frame. The crosshead was then held constant and a tensile stress increase was measured as the SMP attempted to return to its original shape. During the heating from 60°C to 90°C after re-gripping, the thermal expansion of the grips and extension rods imposed an elastic deformation on the specimen. At the end of the recovery heating (time 'D'), the system was allowed to dwell at 90°C for 25 minutes and then the thermomechanical cycle was repeated.

II.B.2.1. Loading at 90°C ($T>T_g$) and Unloading at 25°C ($T<T_g$)

The stress-extension behavior during loading at 90°C and unloading at 25°C (cf. steps ‘A’ and ‘C’ in Figure 10 and Figure 11, respectively) for sample 10%, 15%, 20%, and 25% extension experiments is presented in Figure 12(a) and (b), respectively, with the beginning (loading) and end (unloading) points offset to zero for comparison. It is observed that the stress-extension relationship is approximately linear during loading, even to extensions of 25%, and the behavior is consistent between specimens. The data for the loading and unloading modulus for both cycles of all test cases is presented in Table 2. Specifically, the average modulus value, calculated using a linear fit to the unloading data and initial loading data, and the range (maximum - minimum) of all three specimens tested at each test condition is presented. It is observed that the modulus during loading at 90°C, calculated up to an extension of 5%, is approximately 20 MPa in both the first and second cycles for all tests performed, and the unloading modulus at 25°C is approximately 1700 MPa. Further, there is a negligible change in the modulus values from the first cycle to the second cycle for the tests performed.

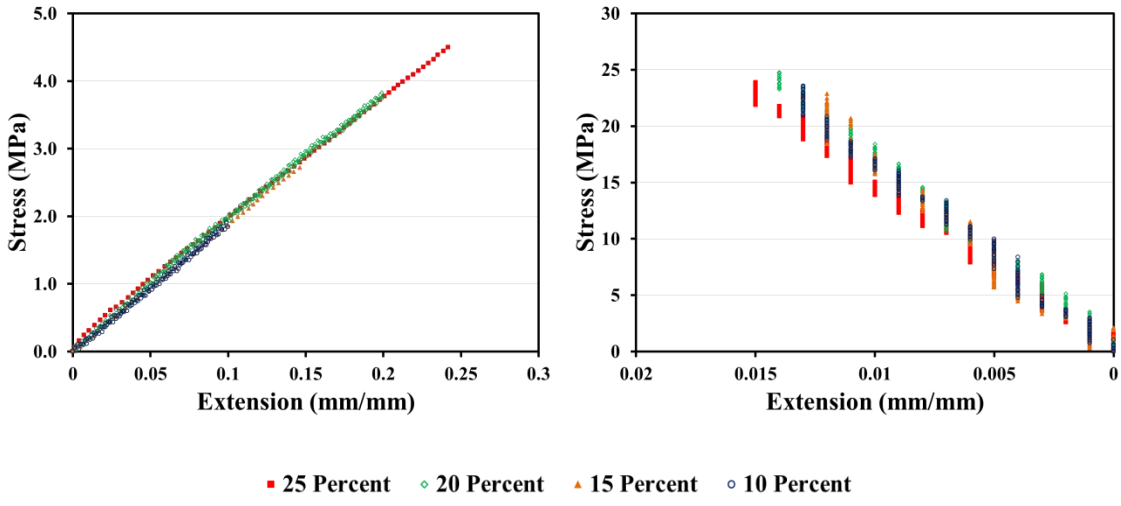

(a) (b)

Figure 12 - Stress-extension results during (a) loading at 90°C and (b) unloading at 25°C for 10%, 15%, 20%, and 25% extension experiments.

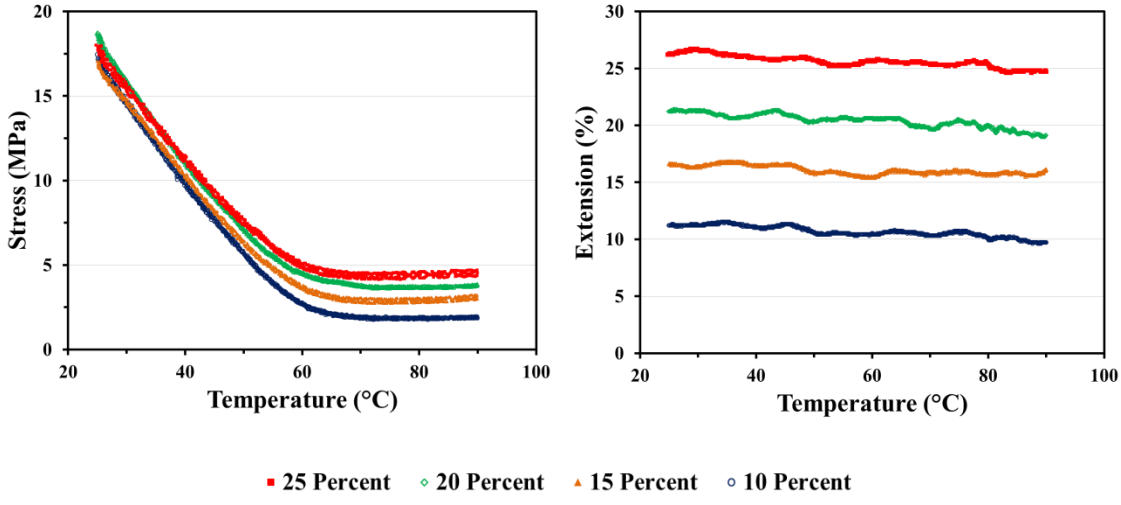

(a) (b)

Figure 13- (a) Stress-temperature and (b) extension-temperature results during constrained cooling from 90°C to 25°C for 10%, 15%, 20%, and 25% extension experiments.

Table 2 - Tensile modulus during loading at 90°C and unloading at 25°C. (Note: FR: free recovery, CR: constrained recovery).

	Loading at 90°C				Unloading at 25°C			
	Cycle 1		Cycle 2		Cycle 1		Cycle 2	
	Tensile Modulus (MPa)	Range[a] (MPa)	Tensile Modulus (MPa)	Range (MPa)	Tensile Modulus (MPa)	Range (MPa)	Tensile Modulus (MPa)	Range (MPa)
FR 10%	20.2	2.3	20.8	2.0	1794	312	1802	90
FR 15%	19.7	2.6	20.3	2.3	1700	154	1734	141
FR 20%	20.1	0.8	20.4	1.0	1567	182	1613	60
FR 25%	18.8	1.1	19.6	1.7	1520	115	1497	266
FR Avg.	**19.7**	**1.7**	**20.3**	**1.8**	**1645**	**191**	**1661**	**139**
CR 10%	20.8	1.4	21.6	1.5	1799	149	2113	563
CR 15%	20.0	0.7	21.0	1.4	1814	359	1778	92
CR 20%	20.8	1.2	19.5	1.5	1634	283	1658	413
CR 25%	20.6	0.3	21.1	2.8	1555	350	1614	334
CR Avg.	**20.6**	**0.9**	**20.8**	**1.8**	**1701**	**285**	**1791**	**351**

[a]Range is the maximum value minus the minimum value of the three specimens tested in each case.

II.B.2.2. Constrained Cooling from 90°C to 25°C

The stress-temperature and extension-temperature relationship during constrained cooling (cf. step 'A' to 'B' in Figure 10 and Figure 11) is presented in Figure 13(a) and (b), respectively, for sample 10%, 15%, 20%, and 25% extension experiments. During this portion of the thermomechanical path, the laser extensometer measurements are used as feedback to the MTS® Testworks® PID control to offset the extension imposed by the thermal contraction of the grips and extension rods. Due to the resolution of the laser extensometer, which is 0.001 in. or 0.3% of the specimen gage length, the system is unable to completely offset the thermal contraction of the grips and rods without causing significant oscillations in the stress of the material. Therefore, the PID parameters were adjusted such that the SMP experienced a relatively smooth stress increase while minimizing the extension increase during the constrained cooling. As presented in Table 3, the SMP specimens experienced a resulting increase in the extension of 1-1.5%, which was a combination of thermal contraction of the SMP and elastic deformation on the SMP due to the thermal contraction of the grips and rods. The stress increase during the cooling step was approximately 15 MPa. Further, no significant differences were observed in the material response from the first cycle to the second cycle.

Table 3 - Stress and extension increases (stress increase and extension increase are the stress and extension values, respectively, measured at the end of cooling (25°C) minus the stress and extension values measured at the beginning of cooling (90°C)) during constrained cooling from 90°C to 25°C. (Note: FR: free recovery, CR: constrained recovery).

	Cycle 1				Cycle 2			
	Stress Increase	**Range[a]**	**Extension Increase**	**Range**	**Stress Increase**	**Range**	**Extension Increase**	**Range**
	(MPa)	**(MPa)**	**(%)**	**(%)**	**(MPa)**	**(MPa)**	**(%)**	**(%)**
FR 10%	16.0	0.8	1.4	0.1	15.8	0.2	1.3	0.7
FR 15%	14.1	0.1	0.8	0.7	14.3	1.0	1.7	0.4
FR 20%	14.5	0.9	1.8	0.6	14.2	1.3	1.5	0.6
FR 25%	13.7	0.5	1.8	0.6	14.3	0.3	1.5	0.9
FR Avg.	**14.6**	**0.6**	**1.5**	**0.5**	**14.7**	**0.7**	**1.5**	**0.6**
CR 10%	15.7	0.5	1.3	0.5	15.7	1.3	0.8	0.5
CR 15%	15.1	0.8	1.3	0.1	14.3	1.3	0.6	0.9
CR 20%	15.2	2.6	1.8	0.5	14.2	1.4	0.7	0.7
CR 25%	15.1	1.1	2.1	0.7	14.0	1.5	1.4	1.8
CR Avg.	**15.3**	**1.3**	**1.6**	**0.5**	**14.6**	**1.4**	**0.9**	**1.0**

[a]Range is the maximum value minus the minimum value of the three specimens tested in each case.

II.B.2.3. Recovery during Heating from 90°C to 25°C

The following sections present the recovery data for the free recovery (2.3.1) and constrained displacement recovery (2.3.2). This step of the load path starts at time 'D' in Figure 10 and Figure 11 and ends when the original temperature of 90°C is achieved.

II.B.2.3.1. Free Recovery

The extension recovery during heating at zero load for each of the four extension values is presented in Figure 14. Figure 14(a) presents the extension recovery as a function of temperature, and Figure 14(b) presents the extension recovery normalized by the extension at the start of the heating. It is observed that the recovery occurs at the same temperature, regardless of the value of applied extension, with the midpoint of recovery occurring at approximately 75°C. Further, Table 4 presents the average values for the extension at the start (25°C) and the end (90°C) of the heating procedure. In the first cycle, the 10% extension tests had a small irrecoverable deformation (0.4%) but the 15%, 20%, and 25% tests recovered 100% of the applied deformation as the final extension at 90°C was within the error range (+/- 0.3%) of the resolution of the laser extensometer. In the second cycle, the specimens recovered 100% of the applied deformation for all values of applied extension.

II.B.2.3.2. Constrained Displacement Recovery

The results for the stress-temperature and extension-temperature behavior during the constrained displacement recovery are presented in Figure 15. In this heating step, the load is first maintained at zero by allowing the specimen to hang freely from the top grip. At approximately 60°C, the bottom of the specimen is re-gripped, the crosshead is adjusted to satisfy zero load conditions, and then the crosshead is held constant until the temperature reaches 90°C. In Figure 15(a), the increase in stress is observed to initiate at approximately 65°C, with recovery complete by approximately 75°C. In addition, the extension-temperature results in Figure 15(b) indicate the bottom of the SMP was re-gripped before the onset of shape recovery, and then the thermal expansion of the grips and extension rods imposes an elastic deformation on the SMP from 60°C to 90°C.

Table 5 presents the values for the stress recovery and the resulting decrease in the extension after re-gripping the bottom of the specimen that is caused by the thermal expansion of the extension rods and grips. The value of the stress at the end of recovery ranges approximately linearly from 1.5 MPa at 10% extension to 4.2 MPa at 25% extension, and the stress recovery is observed to be repeatable between the first and second cycles.

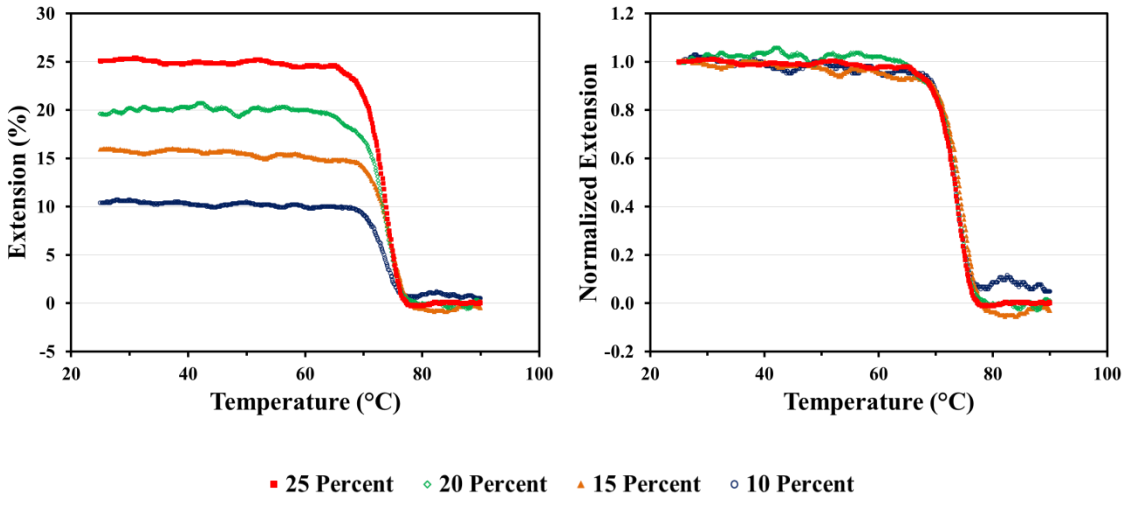

(a) (b)

Figure 14 - (a) Extension-temperature and (b) normalized extension-temperature results during the first cycle recovery heating at zero load from 25°C to 90°C for 10%, 15%, 20%, and 25% extension experiments.

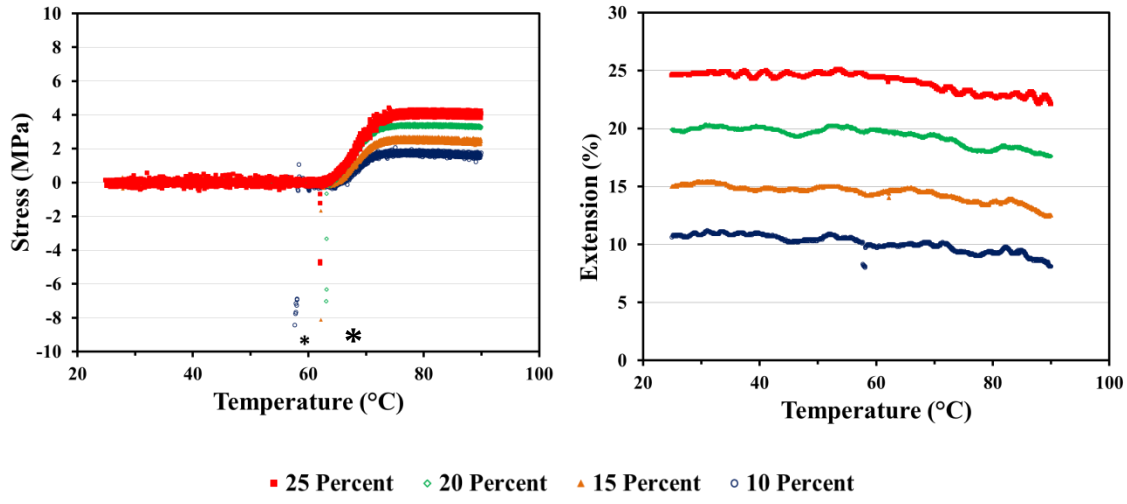

(a) (b)

Figure 15- (a) Stress-temperature and (b) extension-temperature results during the first cycle constrained displacement recovery heating from 25°C to 90°C for 10%, 15%, 20%, and 25% extension experiments. The specimen is allowed to hang freely from the top grip until 60°C, at which temperature the bottom is re-gripped and the crosshead is manually adjusted to offset the compressive stress, denoted by the points near the asterisk * in (a), caused by the gripping procedure.

Table 4 - Extension recovery at zero load.

	Cycle 1				Cycle 2			
	Extension at 25°C	Range[a]	Extension at 90°C	Range	Extension at 25°C	Range	Extension at 90°C	Range
	(%)	(%)	(%)	(%)	(%)	(%)	(%)	(%)
10%	10.2	0.5	0.4	0.3	10.2	0.4	0.1	0.1
15%	15.5	0.6	-0.2	0.8	15.3	0.4	0.1	0.8
20%	20.2	0.9	-0.1	0.6	25.0	0.2	0.0	0.8
25%	25.0	0.2	0.0	0.8	24.9	0.1	0.3	0.2

[a]Range is the maximum value minus the minimum value of the three specimens tested in each case.

Table 5 – Stress recovery at constant crosshead displacement.

	Cycle 1				Cycle 2			
	Stress at End of Recovery	Range[a]	Extension Decrease after Re-gripping	Range	Stress at End of Recovery	Range	Extension Decrease after Re-Gripping	Range
	(MPa)	(MPa)	(%)	(%)	(MPa)	(MPa)	(%)	(%)
10%	1.5	0.5	-1.8	0.5	1.4	0.2	-1.8	0.5
15%	2.4	0.1	-1.7	1.0	2.4	0.3	-1.8	0.9
20%	3.3	0.0	-1.6	0.9	3.4	0.1	-1.8	0.7
25%	4.2	0.1	-1.8	1.2	4.1	0.5	-1.7	0.8

[a]Range is the maximum value minus the minimum value of the three specimens tested in each case.

II.C. Summary and Conclusions

An experimental investigation of a polyurethane shape memory polymer was conducted. The SMP was a thermosetting shape memory polymer first proposed by Wilson et al. [69] that is being considered for use in biomedical applications and was previously untested in terms of shape memory properties. As such, the material was fabricated in a custom mold that resulted in sheets of SMP. Thermal and/or mechanical experiments were conducted, including differential scanning calorimetry, dynamic mechanical analysis, thermomechanical analysis, and tensile tests. These tests were performed to obtain the material properties, including the glass transition temperature, rubbery and glassy moduli, coefficients of thermal expansion, and the strain to failure in the rubbery phase.

In addition, shape memory tests were performed on dogbone specimens, which were cut from the sheet of SMP according to ASTM D638 standards [68]. In these experiments, the material was loaded in the rubbery phase, cooled under constraint to the glassy phase, unloaded to zero stress, and then heated for recovery. Two recovery conditions were tested – free (zero load) recovery and constrained displacement recovery. During the free recovery heating, zero load (neglecting gravity) was maintained by ungripping the bottom of the specimen and allowing the specimen to hang freely from the top grip. During the constrained displacement recovery heating, out-of-plane deformation was observed in the specimen due to the thermal load. Consequently, the constrained displacement recovery load path was modified to hold the material at zero load (bottom grip released) until before the sample was expected to recover. Both

recovery conditions were tested for applied extensions of 10%, 15%, 20%, and 25%. A laser extensometer was used for measuring the displacement of the specimen. This non-contact technique enabled two key features of the shape memory load path: (i) capturing the strains imposed on the specimen during the constrained cooling due to the thermal contraction of the grips and extension rods, and (ii) capturing the strain of the material during zero load recovery, in which the bottom of the specimen is ungripped.

In analyzing the experimental results, it was observed that the tensile modulus of the glassy phase was approximately two orders of magnitude higher than that of the rubbery phase. On the other hand, the coefficient of thermal expansion of the rubbery phase was an order of magnitude larger than that of the glassy phase. It was observed that the specimen was able to withstand up to 55% extension in isothermal strain-to-failure tensile tests. However, the specimen was limited to 25% extension in shape memory experiments as the material was observed to often fail shortly after the initial loading was complete and the constrained cooling began. Thus, this difference in maximum extensions may be a result of the holding procedure, which provides more time for defects in the SMP to propagate.

In the shape memory experiments, the stress-extension response during loading remains approximately linear at 90°C for all values of extension up to 25%. The tensile modulus was calculated to be approximately 20 MPa at 90°C and 1700 MPa at 25°C. During the constrained cooling step, the PID system in the MTS® Testworks® software was able to limit the extension imposed on the SMP by the thermal contraction of the grips and extension rods to approximately 1.5%. In the free recovery experiments, it

was observed that the specimens tested to 10% extension recovered nearly all of the deformation in the first cycle and then 100% of the applied deformation in the second cycle. For the 15%, 20%, and 25% extensions, 100% recovery was observed in both cycles. In addition, the shape recovery occurred at the same temperatures, regardless of the value of applied deformation. In the constrained recovery experiments, it was observed that the value of the stress at the end of recovery, ranging from 1.5 MPa at 10% extension to 4.2 MPa at 25% extension, was approximately linear with respect to the value of the applied extension.

CHAPTER III

ONE-DIMENSIONAL MODELING OF THE FREE AND CONSTRAINED DISPLACEMENT RECOVERY IN SHAPE MEMORY POLYMERS*

An introduction to the shape memory effect and a survey of experimental and modeling efforts in the literature was presented in Chapter I. Chapter II expanded on the experimental efforts to characterize a polyurethane shape memory polymer that is being considered for biomedical applications. In this experimental investigation, uniaxial experiments were performed to evaluate the free and constrained displacement recovery behavior for increasing values of applied extension. This chapter utilizes the experimental data in Chapter II to calibrate a constitutive model that is reduced to and implemented in 1-D. The calibrated model is used to predict the response of the SMP for the other experimental cases.

---

*Part of this chapter is reprinted with permission from "Analysis of the Finite Deformation Response of Shape Memory Polymers: II. 1D Calibration and Numerical Implementation of a Finite Deformation, Thermoelastic Model" by Volk, B.L., Lagoudas, D.C., and Chen, Y.-C.., 2010. *Smart Materials and Structures*. **19**, 075006, DOI: 10.1088/0964-1726/19/7/075006, Copyright 2010 by IOP Publishing Limited.

and from "Characterizing and Modeling the Free Recovery and Constrained Recovery of a Polyurethane Shape Memory Polymer" by Volk, B.L., Lagoudas, D.C., and Maitland, D.J., 2011. *Smart Materials and Structures*. **20**, 094004, DOI: 10.1088/0964-1726/20/9/094004, Copyright 2011 by IOP Publishing Limited.

III.A. Kinematics

In agreement with the type of shape memory polymer that was experimentally characterized and is being considered for biomedical devices, this work focuses on modeling the shape memory polymer response in a finite deformation framework for thermosetting SMPs that are actuated about the glass transition temperature. Thus, the modeling efforts assume the SMP is a rubbery material at high temperatures, a glassy material at low temperatures, and that the shape memory effect (i.e. strain storage and release) is enabled by a phase transition between the two phases during heating or cooling. Due to the fact that the modulus of the rubbery phase is much lower than the glassy phase (cf. Figure 7) and can thus undergo larger deformations, the stress-free rubbery phase is assumed to be the reference configuration.

Further, it is assumed that deformations imposed while the material is in the rubbery phase are stored in the glassy phase upon constrained cooling. As a result of the deformation storing process during constrained cooling, an evolving, intermediate natural configuration is generated. The intermediate natural configuration attains its final configuration once the SMP has been completely transformed (i.e. cooled) to the glassy phase. This final natural configuration can be realized by completing the constrained cooling and removing the applied loads. This configuration is termed the *temporary shape*, in which it is assumed the SMP can remain indefinitely until heat is applied. Upon subsequent heating from the glassy phase to the rubbery phase, the natural configuration evolves from the temporary shape to the reference configuration of the rubbery phase. A kinematic schematic of this behavior is presented in Figure 16.

To model this behavior, this work uses the kinematic relationship proposed by Chen and Lagoudas [118], which is developed on the basis of nonlinear thermoelasticity and thus assumes the deformation gradient is a function of the first Piola-Kirchhoff

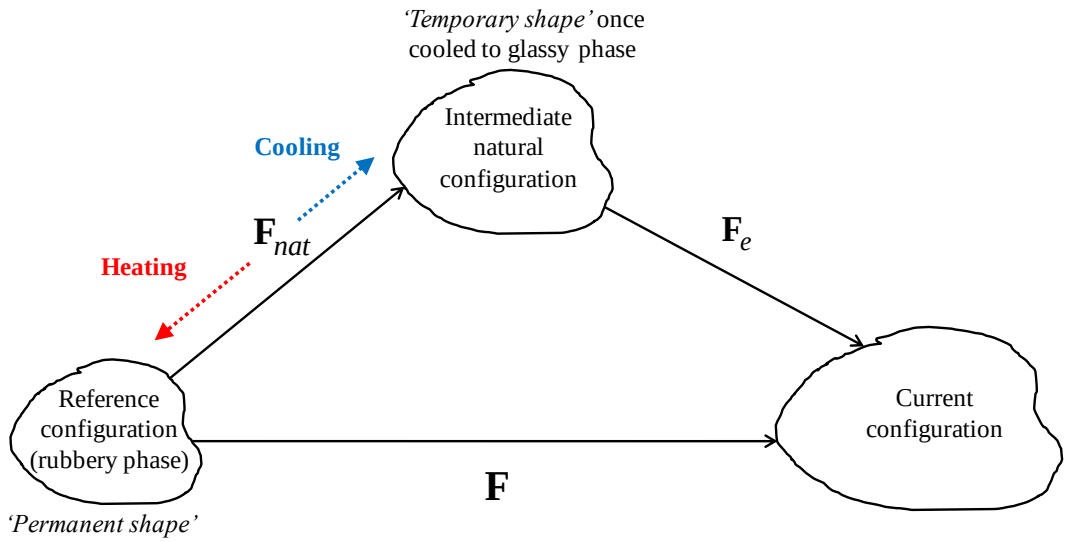

$\mathbf{F} = \mathbf{F}_{nat}\mathbf{F}_e$

$\mathbf{F}$ = total deformation gradient

$\mathbf{F}_{nat}$ = deformation gradient to the natural configuration

$\mathbf{F}_e$ = elastic deformation gradient

Figure 16 – Kinematic schematic of the shape memory polymer behavior. The reference configuration is assumed to be the stress-free in the rubbery phase ('permanent shape). An intermediate natural configuration evolves during cooling (to the 'temporary shape') and is recovered upon subsequent heating.

stress $\mathbf{P}$ and absolute temperature θ. The approach adopted in the kinematics is to first consider a collection of individual material points that begin in the rubbery phase and transform (i.e. nucleate) at a discrete temperature to the glassy phase. Through consideration of the response of individual particles that are in the glassy and rubbery phases, a volume averaging technique is then employed to obtain the constitutive

response temperature in which both particles are present. First, it is proposed that the deformation gradient $\mathbf{F}_e^r\left(\mathbf{P}\left(\mathbf{X},t\right),\theta\left(\mathbf{X},t\right)\right)$ describes the elastic response of a material point $\mathbf{X}$ that has a rubbery phase stress-free configuration and is subsequently undergoing deformation in the rubbery phase. Similarly, a deformation gradient $\mathbf{F}_e^g\left(\mathbf{P}\left(\mathbf{X},t\right),\theta\left(\mathbf{X},t\right)\right)$ is proposed to describe the elastic response of a material point that has a natural configuration in the glassy state and is subsequently undergoing deformation in the glassy phase.

Considering the assumption that all material points have a reference configuration in the rubbery phase, a deformation gradient $\mathbf{F}_{nat}$ is introduced to describe the transformation from the reference rubbery phase to the natural configuration of the glassy phase. Thus, the total deformation gradient for a material point that has a rubbery reference configuration and is currently in the glassy phase is obtained through the multiplicative decomposition $\mathbf{F}=\mathbf{F}_e^g\left(\mathbf{P}\left(\mathbf{X},t\right),\theta\left(\mathbf{X},t\right)\right)\mathbf{F}_{nat}$. The deformation gradient that describes the transformation from the rubbery phase to the glassy phase is obtained through assuming the deformation gradient of the material is continuous as it transforms from the rubbery phase to the glassy phase at time τ, as shown in Equation (1). The resulting expression for $\mathbf{F}_{nat}$ is obtained by rearranging Equation (1) to Equation (2).

$$\mathbf{F}_e^r\left(\mathbf{P}\left(\mathbf{X},\tau\right),\theta\left(\mathbf{X},\tau\right)\right)=\mathbf{F}_e^g\left(\mathbf{P}\left(\mathbf{X},\tau\right),\theta\left(\mathbf{X},\tau\right)\right)\mathbf{F}_{nat} \tag{1}$$

$$\Rightarrow \mathbf{F}_{nat}=\mathbf{F}_e^{g^{-1}}\left(\mathbf{P}\left(\mathbf{X},\tau\right),\theta\left(\mathbf{X},\tau\right)\right)\mathbf{F}_e^r\left(\mathbf{P}\left(\mathbf{X},\tau\right),\theta\left(\mathbf{X},\tau\right)\right) \tag{2}$$

A summary of the deformation gradients for individual material particles and their respective reference and current phases is presented in Table 6. A visual description of the deformation gradients and the enforcement of continuity at the transition temperature can be seen in [113] (cf. Figure 1).

Table 6 – Deformation gradients for material points with different reference and current configurations.

Reference configuration	Current configuration	Deformation gradient
Rubbery	Rubbery	$\mathbf{F}_e^r\left(\mathbf{P}\left(\mathbf{X},t\right),\theta\left(\mathbf{X},t\right)\right)$
Glassy	Glassy	$\mathbf{F}_e^g\left(\mathbf{P}\left(\mathbf{X},t\right),\theta\left(\mathbf{X},t\right)\right)$
Rubbery	Glassy	$\mathbf{F}_e^g\left(\mathbf{P}\left(\mathbf{X},t\right),\theta\left(\mathbf{X},t\right)\right)\mathbf{F}_{nat}$

It is then assumed that the SMP smoothly transitions from the rubbery phase to the glassy phase over a range of temperatures, during which the stress is allowed to change due to elastic and thermal (expansion, contraction) effects. This smooth transition is assumed to be due to the collection material points that are transforming at different temperatures. As such, a representative volume element is introduced and the volume average deformation gradient is calculated through Equation (3). In calculating this equation, it is assumed that the stress and temperature are spatially constant throughout the body. In other words, it is assumed that the stress and temperature are only functions of time.

$$\begin{aligned}\bar{\mathbf{F}}(t) &= \frac{1}{V}\int_{\Omega}\mathbf{F}\,dV(\mathbf{X}) \\ &= \frac{1}{V}\int_{\Omega_r}\mathbf{F}_e^r\left(\mathbf{P}(t),\theta(t)\right)dV(\mathbf{X}) \\ &+ \frac{1}{V}\int_{\Omega_g}\mathbf{F}_e^g\left(\mathbf{P}(t),\theta(t)\right)\tilde{\mathbf{F}}\left(\mathbf{P}(\tau),\theta(\tau)\right)dV(\mathbf{X})\end{aligned} \tag{3}$$

where Ω represents the body, Ω_r and Ω_g represent the rubbery and glassy regions, respectively, and V is the volume of the body. Note that, consistent with the assumption of being spatially constant, $\mathbf{P}$ and θ now depend solely on the time *t*. However, $\mathbf{P}$ and θ in the deformation gradient $\mathbf{F}_{nat}$ depend instead on the time τ, which remains a function of position **X**, at which the particle was last cooled through the glass transition temperature.

A glassy volume fraction $\phi(\theta)$ is introduced in Equation (4) to represent the fraction of material that has transformed from the rubbery phase to the glassy phase. Consistent with experimental results [113], this volume fraction is assumed to be a function of temperature only and does not depend on the value of applied stress or strain.

$$\phi(\theta) = \frac{1}{V}\int_{\Omega_g} dV \tag{4}$$

After substituting the expression for the glassy volume fraction into Equation (3) and performing a change of variables on the glassy region integral [70, 72], the resulting kinematic relationship is presented in Equation (5).

$$\bar{\mathbf{F}} = \left[1-\phi(\theta)\right]\mathbf{F}_e^r(\mathbf{P},\theta) + \int_0^t \mathbf{F}_e^g(\mathbf{P},\theta)\mathbf{F}_{nat}(\mathbf{P}(\tau),\theta(\tau))\phi'(\theta(\tau))\theta'(\tau)d\tau \tag{5}$$

where the dependence of $\bar{\mathbf{F}}$, $\mathbf{P}$ and θ on time t has been suppressed for simplicity. Note that, for the remainder of this work, the average deformation gradient is taken to be equivalent to the deformation gradient of the shape memory polymer $\mathbf{F}$. Thus, $\bar{\mathbf{F}}$ (and quantities derived from $\bar{\mathbf{F}}$) will not be shown with the overbar.

III.A.1. Constraint on the Rubbery and Glassy Rotations

In performing the volume average of the deformation gradient, the stress and temperature were assumed to be spatially uniform. An additional consequence of this assumption, as well as objectivity, is that the rotations of the rubbery and the glassy phases must be arbitrary. That is, when decomposing the deformation gradients into their rotational and stretch components, the rotations should not affect the constitutive response of the material as to maintain the spatially uniform stress state.

As a result, a kinematic assumption is made about the rotations of the material. First, the polar decompositions of the average deformation gradient as well as the elastic deformation gradients in the rubbery and glassy phases are considered in Equation (6). Consistent with the assumption of spatially uniform stress and without loss of generality, the rotations in the polar decompositions are then assumed, in Equation (7), to be spatially constant within the SMP. That is, the average rotation is assumed to be equal to the rotations in each the rubbery and the glassy phases.

$$\begin{aligned}\mathbf{F} &= \mathbf{R}\mathbf{U} \\ \mathbf{F}_e^r &= \mathbf{R}_e^r \mathbf{U}_e^r \\ \mathbf{F}_e^g &= \mathbf{R}_e^g \mathbf{U}_e^g\end{aligned} \tag{6}$$

$$\mathbf{R} = \mathbf{R}_e^r = \mathbf{R}_e^g \tag{7}$$

Substituting the polar decompositions of Equation (6) into the kinematics presented in Equation (5) results in Equation (8).

$$\begin{aligned}\mathbf{U} = &\left[1-\phi(\theta)\right]\mathbf{U}_e^r(\mathbf{S},\theta) \\ &+\mathbf{U}_e^g(\mathbf{S},\theta)\int_0^t \mathbf{U}_{nat}(\mathbf{S}(\tau),\theta(\tau))\phi'(\theta(\tau))\theta'(\tau)d\tau\end{aligned} \tag{8}$$

where the deformation gradient $\mathbf{F}_{nat}$ was reduced in Equation (5) to $\mathbf{U}_{nat}$ by substituting Equations (6) and (7) into Equation (2), as shown in Equation (9).

$$\begin{aligned}\mathbf{U}_{nat} = \mathbf{F}_{nat}\,|_{\mathbf{R}=\mathbf{R}_e^r=\mathbf{R}_e^g} &= \mathbf{U}_e^{g^{-1}}(\tau)\mathbf{R}_e^{g^{-1}}(\tau)\mathbf{R}_e^r(\tau)\mathbf{U}_e^r(\tau) \\ &= \mathbf{U}_e^{g^{-1}}(\tau)\mathbf{R}^{-1}(\tau)\mathbf{R}(\tau)\mathbf{U}_e^r(\tau) \\ &= \mathbf{U}_e^{g^{-1}}(\tau)\mathbf{U}_e^r(\tau)\end{aligned} \tag{9}$$

III.B. Constitutive Equations

In addition to the kinematics derived in Section A, constitutive equations must be prescribed to model the stress-strain behavior of the shape memory polymer. In Equation (5), the average deformation gradient is expressed as a function of the rubbery and glassy phase deformation gradients, which are functions of the current stress and temperature. This section presents the derivations for the constitutive equations for the rubbery and glassy phases. The stress for the entire SMP, as a mixture of the two

phases, is provided through the assumption that the stress is spatially constant; thus, it is assumed that the stress in the rubbery phase is equal to that of the glassy phase.

The constitutive equations in this work follow the previous works by Chen and Lagoudas [113] and Volk et al. [113, 114], in which the rubbery and glassy phases are modeled as incompressible neo-Hookean materials and the material response is assumed to be isotropic. The Helmholtz free energy for the incompressible neo-Hookean material is given through Equation (10),

$$\Psi(\mathbf{C}) = \frac{\mu}{2}\left(I_{\mathbf{C}} - 3\right) \tag{10}$$

where $\mathbf{C}$ is the right Cauchy-Green deformation tensor $\left(\mathbf{C} = \mathbf{F}^{\mathrm{T}}\mathbf{F}\right)$ [69, 70, 115], μ is the shear modulus, and $I_{\mathbf{C}} = \mathrm{tr}(\mathbf{C})$ is the first invariant of $\mathbf{C}$. For incompressible materials that are functions of $\mathbf{C}$, the second Piola-Kirchhoff stress $\mathbf{S}$ is derived through Equation (11) [120, 121].

$$\mathbf{S} = -p\mathbf{C}^{-1} + 2\frac{\partial\Psi\left(\mathbf{C}\right)}{\partial\mathbf{C}} \tag{11}$$

where p is the hydrostatic pressure necessary to maintain incompressibility. The derivative of the Helmholtz free energy with respect to $\mathbf{C}$ is calculated to be

$$\frac{\partial\Psi\left(\mathbf{C}\right)}{\partial\mathbf{C}} = \frac{\mu}{2}\frac{\partial I_{\mathbf{C}}}{\partial\mathbf{C}} = \frac{\mu}{2}\mathbf{I} \tag{12}$$

where $\mathbf{I}$ is the second order identity tensor. Substituting Equation (12) into Equation (11), the second Piola-Kirchhoff stress is given by Equation (13). The first Piola-

Kirchhoff stress $\mathbf{P}$ is then calculated through a transformation of the second Piola-Kirchhoff stress and is given by Equation (14).

$$\mathbf{S} = -p\mathbf{C}^{-1} + \mu\mathbf{I} \tag{13}$$

$$\mathbf{P} = \mathbf{F}\mathbf{S} = -p\mathbf{F}^{-\mathrm{T}} + \mu\mathbf{F} \tag{14}$$

While the phases are assumed to be incompressible due to isothermal deformations, the ability for the material to thermally contract and expand is accounted for through the introduction of a volume ratio $\upsilon(\theta) = \det \mathbf{F}$ that is a function of only the temperature. This quantity represents the ratio of the volume at the current temperature θ to that at the reference temperature θ_0.

Thus, in assuming incompressible neo-Hookean elastic response for each the rubbery and the glassy phases, the constitutive equations for the individual phases are obtained and presented in Equation (15).

$$\begin{aligned} \mathbf{P}^r &= -p^r \mathbf{F}_e^{r\,-\mathrm{T}} + \mu^r \mathbf{F}_e^r, \quad \upsilon^r(\theta) = \det \mathbf{F}_e^r \\ \mathbf{P}^g &= -p^g \mathbf{F}_e^{g\,-\mathrm{T}} + \mu^g \mathbf{F}_e^g, \quad \upsilon^g(\theta) = \det \mathbf{F}_e^g \end{aligned} \tag{15}$$

III.C. Reduction to 1D

The previous sections have established the kinematic and constitutive equations that are the focus of this chapter. In this section, these equations are reduced to 1D to facilitate implementation in a computational code such that the material response in 1D can be quickly predicted.

III.C.1. Constitutive Equations

Beginning with the constitutive equations presented in Equation (15) and following previous efforts [121], the polar and spectral decompositions are employed in reducing the general 3D equation into 1D. To begin, consider the polar decomposition in Equation (16) of the constitutive equation and the associated kinematic quantities in Equation (14).

$$\begin{aligned} \mathbf{P} &= \mathbf{QT} \\ \mathbf{F} &= \mathbf{RU} \end{aligned} \tag{16}$$

where $\mathbf{Q}$ and $\mathbf{R}$ are the proper orthogonal tensors related to the rotation component of the deformation. Similarly, $\mathbf{T}$ and $\mathbf{U}$ are the symmetric tensors related to the stretching component of the deformation. By substituting the polar decompositions and assuming the $\mathbf{Q} = \mathbf{R} = \mathbf{I}$ [108, 115], Equation (14) reduces to Equation (17).

$$\mathbf{T} = -p\mathbf{U}^{-\mathrm{T}} + \mu\mathbf{U}, \qquad \upsilon(\theta) = \det \mathbf{U} \tag{17}$$

After employing the polar decomposition, the spectral decomposition is used to relate the eigenvalues of the stress to the eigenvalues of the stretches. Thus, the spectral decomposition of the stresses and stretches are presented in Equation (18), where s_i and λ_i are the principal stresses and stretches, respectively. The stretch of the material is defined as the ratio of the current dimension compared to the initial dimension. In other words, the stretch assumes a value of 1 when the material is undeformed, a value greater than 1 during extension, and a value less than 1 during compression.

$$\mathbf{T} = \sum_{i=1}^{3} s_i \mathbf{e}_i \otimes \mathbf{e}_i$$
$$\mathbf{U} = \sum_{i=1}^{3} \lambda_i \mathbf{e}_i \otimes \mathbf{e}_i \tag{18}$$

Substituting Equation (18) into Equation (17), the stresses and volume ratios in terms of the principal stretches of the rubbery and glassy phases are presented in Equation (19). Note that no 'r' or 'g' superscript is present on stress components in the constitutive equations, indicating the assumption of constant stress throughout the body $\left(s^r = s^g = s\right)$ has already been enforced.

$$\begin{aligned} s_i &= -p^r \lambda_i^{r^{-1}} + \mu^r \lambda_i^r, \quad \upsilon^r(\theta) = \lambda_1^r \lambda_2^r \lambda_3^r \\ s_i &= -p^g \lambda_i^{g^{-1}} + \mu^g \lambda_i^g, \quad \upsilon^g(\theta) = \lambda_1^g \lambda_2^g \lambda_3^g \end{aligned} \qquad i = 1,2,3 \tag{19}$$

III.C.1.1. Uniaxial Deformations

For uniaxial deformations in which the applied stress state is $s_1 = s(t)$ while $s_2 = s_3 = 0$, the pressure terms in Equation (19) can be eliminated through a system of algebraic equations. The resulting relationship between the principal stretches is given through Equation (20), where λ is defined as the stretch is the direction of the applied stress.

$$\begin{aligned} \lambda_1 &= \lambda \\ \lambda_2 &= \lambda_3 = \sqrt{\frac{\upsilon(\theta)}{\lambda}} \end{aligned} \tag{20}$$

In relating the axial stretch to the experimental data presented in Chapter II, the axial stretch is defined through Equation (21), where L is the length of the SMP, L_0 is the initial length of the SMP, and ΔL is the change in the SMP length in the axial direction. The quantity $\left(\Delta L / L_0\right)$ is defined as the extension, which is the quantity that is experimentally measured and presented in the resulting data.

$$\lambda = 1 + \left(\frac{\Delta L}{L_0} \right) \tag{21}$$

After eliminating the pressure terms in Equation (19), the resulting constitutive equations relating the applied stress and the stretch in the principal direction are given by Equation (22).

$$\begin{aligned} \mu^r \left(\lambda^r - \frac{\upsilon^r(\theta)}{\left(\lambda^r\right)^2} \right) &= s(t) \\ \mu^g \left(\lambda^g - \frac{\upsilon^g(\theta)}{\left(\lambda^g\right)^2} \right) &= s(t) \end{aligned} \tag{22}$$

III.C.2. Kinematics

After performing the polar decomposition of the average deformation gradient in Equation (5) and eliminating the rotational components from the deformation gradients, the average deformation gradient $\mathbf{F}$ is reduced to an expression for the average stretch $\mathbf{U}$ as shown in Equation (8). Through the spectral decomposition of Equation (18), the stretch tensor is further reduced to a diagonal matrix with components equal to the principal stretches in Equation (20). Considering only the stretch in the direction of the

applied stress, Equation (23) presents the principal stretch λ in terms of λ^r and λ^g – the rubbery and glassy principal stretches in the direction of the applied stress, respectively, which are quantified through the constitutive equations in Equation (22). Note that the axial glassy stretch as a function of the current stress and temperature has been moved outside the integral to isolate only the terms that depend on τ inside the integral.

$$\lambda = \left[1-\phi(\theta)\right]\lambda^r(\mathbf{P},\theta) + \lambda^g(\mathbf{P},\theta)\int_0^t \frac{\lambda^r\left(\mathbf{P}(\tau),\theta(\tau)\right)}{\lambda^g\left(\mathbf{P}(\tau),\theta(\tau)\right)}\phi'\left(\theta(\tau)\right)\theta'(\tau)\,d\tau \qquad (23)$$

III.D. Calibration of Material Properties

The rubbery and glassy phase constitutive equations and the kinematic equation presented in Equations (22) and (23), respectively, result in a total of five parameters that must be calibrated to solve the system of equations for the state of the material. These parameters are the shear moduli in the rubbery and glassy phases (μ^r and μ^g, respectively), the volume ratios in the rubbery and glassy phases ($\upsilon^r(\theta)$ and $\upsilon^g(\theta)$, respectively), and the glassy volume fraction $\phi(\theta)$ as a function of temperature. In considering the experiments performed in Chapter II, it is determined that all of the five calibration functions can be calculated from the data when functional forms are assumed for the volume ratios and glassy volume fraction. In particular, the five calibration parameters can be calculated from a single experimental result. As the elastic modulus is commonly defined at smaller values of extension and because the mechanism for shape

recovery is observed to be independent of applied extension (cf. Figure 14(b)), the material properties for the model are calibrated from the 10% free recovery experiment presented in Figure 10(a).

III.D.1. Shear Moduli

Considering first the shear moduli in the rubbery and glassy phases, it is observed that these parameters can be calculated from the isothermal loading and unloading data in the thermomechanical load path. In this work, the shear moduli of the individual phases are assumed to be temperature independent. The effective material properties, however, of the composite are temperature dependent due to the mixture of the rubbery and glassy phases. Specifically, assuming each phase is isotropic, the shear moduli for the rubbery and glassy phases are calculated from Equation (24).

$$\mu^r = \frac{E^r}{2\left(1+\nu^r\right)}$$
$$\mu^g = \frac{E^g}{2\left(1+\nu^g\right)} \tag{24}$$

where ν^r and ν^g are the Poisson's ratios for the rubbery and glassy phases, respectively, and E^r and E^g are the Young's moduli for the rubbery and glassy phases, respectively. The Young's modulus for the rubbery phase and glassy phase is calculated from the loading segment at 90°C and the unloading segment at 25°C, respectively. Figure 17(a) and (b) presents the respective stress-strain data for the loading and unloading steps. Consistent with the assumption of incompressible response in each phase, the values of

the Poisson's ratios are assumed to be 0.5 for the rubbery and glassy phases[1]. Thus, the shear moduli for the rubbery and glassy phases are calculated to be 1/3 of the value of the tensile moduli during the loading and unloading steps, respectively. The rubbery and glassy shear moduli are thus calculated, from the 10% free recovery experiment to be 7.03 MPa and 606 MPa, respectively.

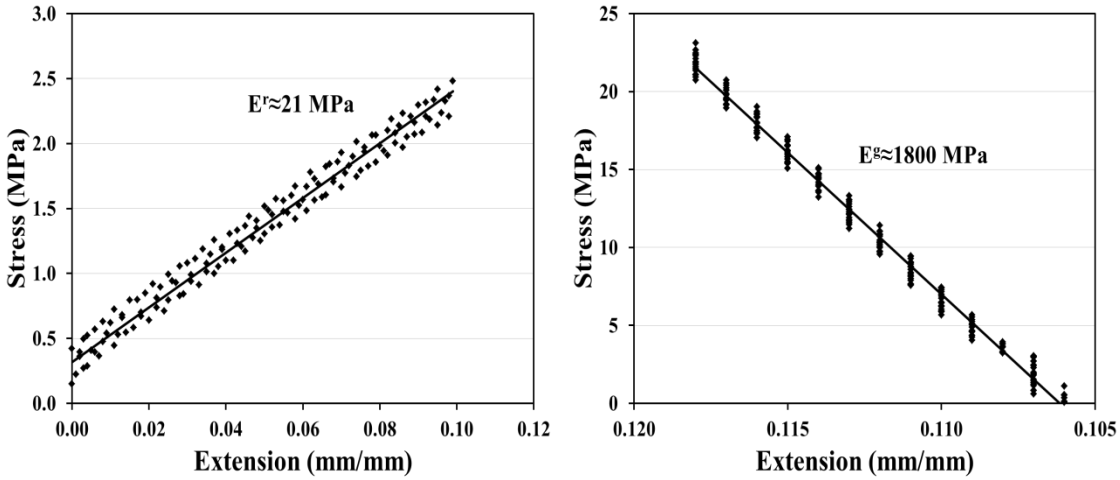

(a) (b)

Figure 17 – Stress-extension data for (a) isothermal loading at 90°C and (b) isothermal unloading at 25°C. Results shown are from a 10% extension free recovery experiment.

[1] In the next chapter, more general compressible neo-Hookean constitutive equations are derived for these two phases that provide a means for calibrating the material properties when the Poisson's ratios are

III.D.2. Volume Ratios

The volume ratios for the rubbery and glassy phases are the ratio of the volume of the material at the current temperature compared to the volume of the material at the reference temperature. In deriving the constitutive equations for the rubbery and glassy phases, it is assumed the material is incompressible when deformed at a constant temperature. When considering the material response due to a change in temperature, on the other hand, the volume ratio is proposed to be expressed as a function of the coefficients of thermal expansion as shown in Equation (25).

$$\begin{aligned} \upsilon^r(\theta) &= \left[1+\alpha^r(\theta-\theta_0)\right]^3 \\ \upsilon^g(\theta) &= \left[1+\alpha^g(\theta-\theta_0)\right]^3 \end{aligned} \tag{25}$$

where α^r and α^g are the coefficients of thermal expansion calculated under zero stress in the rubbery and glassy phases, respectively, and θ and θ_0 are the current and initial temperatures, respectively. It is observed that, for no change in temperature, the volume ratio is equal to one and the assumption of incompressibility at a constant temperature is maintained. Furthermore, substituting Equation (25) into Equation (22) for a zero stress condition results in Equation (26).

$$\begin{aligned} \lambda^r(\theta) &= 1+\alpha^r(\theta-\theta_0) \\ \lambda^g(\theta) &= 1+\alpha^g(\theta-\theta_0) \end{aligned} \tag{26}$$

where the stretch of the material in each phase is defined as a function of the coefficient of thermal expansion and the change in the temperature. Substituting Equation (26) into

Equation (21) results in the familiar equations for the thermal strain in a material, presented in Equation (27).

$$\left(\frac{\Delta L}{L_0}\right)^r = \alpha^r\left(\theta-\theta_0\right)$$
$$\left(\frac{\Delta L}{L_0}\right)^g = \alpha^g\left(\theta-\theta_0\right) \tag{27}$$

Through the introduction of Equation (25), the volume ratios are reduced to coefficients of thermal expansion α^r and α^g that must be calibrated. From the experimental results, the coefficients of thermal expansion for the rubbery and glassy phases can be calculated from the extension–temperature curve during recovery heating, as shown in Figure 18. In particular, the glassy and rubbery CTEs can be calculated from the linear extension-temperature response before recovery initiates and after recovery has completed, respectively. However, due to the low coefficient of thermal expansion in the glassy phase and the limitations on the laser extensometer resolution in the experiments in Chapter II, the glassy phase coefficient of thermal expansion is manually adjusted[2] in this work such to fit the stress simulation during cooling to the experimental data. The resulting values of α^r and α^g, as calibrated from the 10% free recovery experiment, are 5.1E-4 (mm/mm)/ °C and 2.0E-5 (mm/mm)/°C, respectively.

[2] In the next chapter, the material properties for the more general compressible neo-Hookean constitutive equations are recalibrated using the more accurate values for the CTEs obtained from the TMA tests in Chapter II. The current method, however, is maintained in this chapter to demonstrate the ability to calibrate all of the material properties from the data of a single experiment.

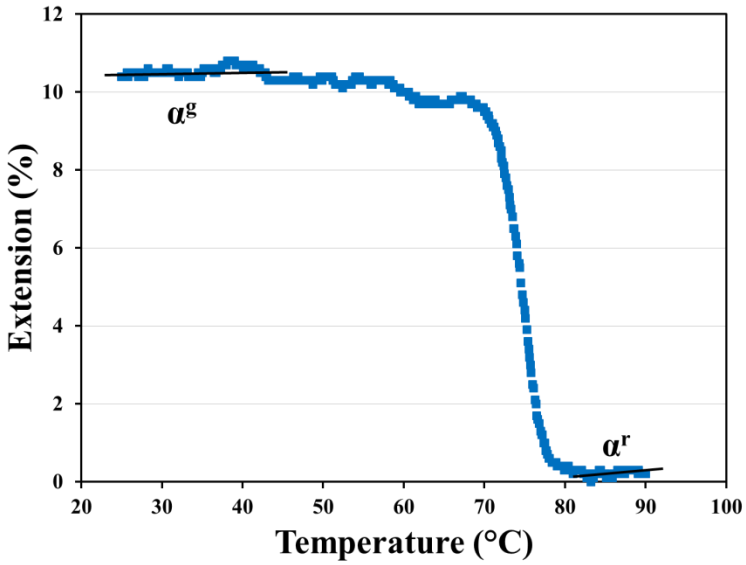

Figure 18 – Extension-temperature results for a 10% free recovery experiment. Indicated are the linear regions outside the transformation region that can be used to calculate the glassy and rubbery coefficients of thermal expansion.

III.D.3. Glassy Volume Fraction

The experimental investigation in Chapter II lacks the capability to directly measure the glassy volume fraction during the experiment. As such, the glassy volume fraction is assumed to behave in a manner similar to that of the shape recovery profile upon heating at zero load. This assumption is supported by reducing Equation (23) and the neo-Hookean relationships for the free recovery condition of $s(t)=0$. By reducing these equations and assuming the thermal stretch is negligible, it can be shown that $\lambda(t) \sim \phi(\theta)$. Consequently, a hyperbolic tangent function is assumed for the glassy volume fraction of the polymer, and is optimized to fit the profile of the strain recovery profile used for calibration. The general form of the proposed function is given in Equation (28).

$$\phi(\theta) = \frac{\tanh\left(\frac{\theta_{\max} - A}{B}\right) - \tanh\left(\frac{\theta - A}{B}\right)}{\tanh\left(\frac{\theta_{\max} - A}{B}\right) - \tanh\left(\frac{\theta_{\min} - A}{B}\right)} \tag{28}$$

where $\theta_{\min}$ and $\theta_{\max}$ are the lower and upper temperature bounds, respectively, for which the hyperbolic tangent function is to be fit. A and B are the respective shifting and scaling factors for adjusting the shape of the hyperbolic tangent function. The parameter A represents the inflection point of the hyperbolic tangent function, and represents a measure of the glass transition temperature T_g. For experiments in which the recovery is observed to be a function of the temperature rate [113], A can be assumed to be proportional to the temperature rate. In addition, the parameter B is inversely proportional to the rate of strain recovery when transforming from the glassy phase to the rubbery phase. B approaches zero in the limit of the phase transition occurring as a step function. The parameters A and B are adjusted to best match the strain recovery profile from which the model is being calibrated.

In this work, the function for the glassy volume fraction is fit to the strain recovery profile for the free recovery experiment with an extension of 10%, which is shown in Figure 19(a). The experimental data curve is first shifted to end at a value of zero and then normalized from 0 to 1. Similarly, the denominator in Equation (28) is used to normalize the resulting hyperbolic tangent function from 0 to 1 to correspond to a material in a pure rubbery or pure glassy phase, respectively. It is observed that a single hyperbolic tangent function of the form presented in Equation (28) is unable to precisely capture the initiation of the shape recovery, as presented in Figure 19(b).

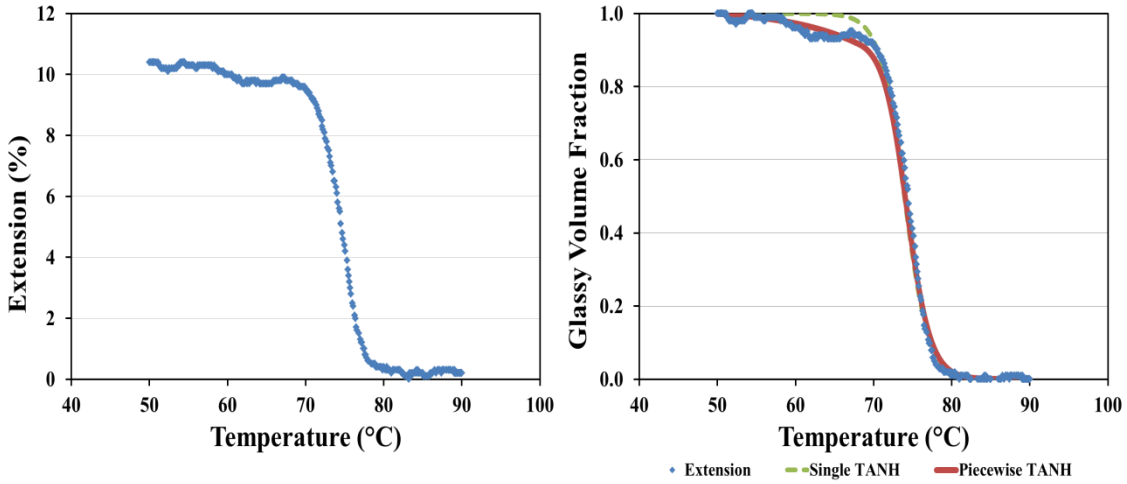

(a) (b)

Figure 19 – (a) 10% extension-temperature free recovery profile and (b) a piecewise hyperbolic tangent function fit to the normalized extension-temperature data. A single hyperbolic tangent is unable to precisely capture the onset of shape recovery and is presented for comparison.

As such, a piecewise function composed of two hyperbolic tangents is used in the current work, with one hyperbolic tangent dictating the curvature of the initiation of recovery and the second hyperbolic tangent dictating the rest of the recovery process. The switch temperature between the two functions is chosen to be the corner at the onset of shape recovery. In addition, a multiplying factor C is introduced to scale the modify the upper limit of the second hyperbolic tangent. A least squares method is used to fit the parameters for the two hyperbolic tangents while enforcing continuity of the glassy volume fraction and its derivative at the switch temperature. The resulting, piecewise hyperbolic tangent is shown in Figure 19(b) as fit to the normalized extension recovery data. It should be noted that the model predictions for the SMP are extremely sensitive to

the fit for the glassy volume fraction. For instance, modeling the glassy volume fraction using the single hyperbolic tangent can be shown, for this polyurethane SMP, to affect the stress at the end of cooling by more than 25%. After determining the function for $\phi(\theta)$, all of the necessary calibration requirements have been determined. Table 7 presents a summary of the material properties for a polyurethane SMP as calibrated from the 10% extension free recovery experiment of Figure 10(a).

Table 7 – Material properties calculated from a 10% free recovery experiment and used as input to the 1D constitutive model using incompressible neo-Hookean equations.

Parameter	Value
Rubbery phase volume ratio	$\upsilon_a = \left[1+\alpha_a\left(\theta-\theta_0\right)\right]^3$ $\alpha_a = 5.1*10^{-4}\ /\ \mathrm{K}$
Glassy phase volume ratio	$\upsilon_f = \left[1+\alpha_f\left(\theta-\theta_0\right)\right]^3$ $\alpha_f = 2.0*10^{-5}\ /\ \mathrm{K}$
Rubbery phase shear modulus	$\mu_a = 7.03$ MPa
Glassy phase shear modulus	$\mu_f = 606$ MPa
Glassy volume fraction	$\phi(\theta) = C\dfrac{\tanh\left(\dfrac{\theta_{\max}-A}{B}\right)-\tanh\left(\dfrac{\theta-A}{B}\right)}{\tanh\left(\dfrac{\theta_{\max}-A}{B}\right)-\tanh\left(\dfrac{\theta_{\min}-A}{B}\right)}$ $\theta_{\min}=323,\ \theta_{\max}=363$ $A=508.44, B=18.71, C=1.00 \quad \theta<341.1$ $A=347.25, B=3.05, C=0.94 \quad \theta\geq 341.1$

III.E. Numerical Implementation in 1D

The previous section reduced the constitutive equations and kinematic relationship for uniaxial deformations. Specifically, Equation (23) reduced the full 3D kinematic relationship in Equation (5) to an expression for the axial stretch in terms of the axial stretches in the rubbery and glassy phases. In addition, Equation (22) presents the reduction of Equation (19) for uniaxial deformations, in which the pressure term is eliminated to result in an equation for the axial stress in terms of the axial stretch for each the rubbery and the glassy phases.

To simulate and predict the uniaxial experiments performed in Chapter II, these 1D equations are numerically implemented in MATLAB®. This implementation is an expansion of previous efforts [72], but improved such that arbitrary uniaxial thermomechanical load paths can be considered. As such, the resulting equations are discretized with respect to time and a system of equations is solved at each increment.

The implementation is performed in such a way to provide two ways of calculating the resulting state of a material during any given load path. In particular, a subroutine is established that calculate the stress of a material when the deformation (i.e. stretch) of the material is given as input. On the other hand, another subroutine calculates the stretch of a material for a given stress input. These two subroutines provide greater flexibility in simulating a standard thermomechanical cycle, in which different segments will control the deformation (e.g., cooling at a fixed strain) or the stress (e.g. heating at zero applied load) of the shape memory polymer.

III.E.1. Stress Controlled Processes

In the system of equations, the method for solving for the state of the material is relatively straightforward for steps in which the applied stress is known. Consider first the kinematic relationship of Equation (23), in which the axial stretch is a function of the axial stretches in the rubbery and glassy phases. The axial stretches of the two constituent phases are subsequently defined through the constitutive relations presented in Equation (22). In these relationships, the stretches are both a function of the applied stress $s(t)$, which is assumed to be constant throughout the body. Solving these equations for the stretch in terms of the stress results in Equation (29).

$$\lambda^{r/g} = \frac{\left(108\upsilon^{r/g}(\theta)\left(\mu^{r/g}\right)^3 + 8s^3 + 12\sqrt{3}\sqrt{\frac{\upsilon^{r/g}(\theta)\left(27\left(\upsilon^{r/g}(\theta)\right)^3\left(\mu^{r/g}\right)^3 + 4s^3\right)}{\mu^{r/g}}}\left(\mu^{r/g}\right)^2 \right)^{1/3}}{6\mu^{r/g}} + \frac{2s^2}{\left(108\upsilon^{r/g}(\theta)\left(\mu^{r/g}\right)^3 + 8s^3 + 12\sqrt{3}\sqrt{\frac{\upsilon^{r/g}(\theta)\left(27\left(\upsilon^{r/g}(\theta)\right)^3\left(\mu^{r/g}\right)^3 + 4s^3\right)}{\mu^{r/g}}}\left(\mu^{r/g}\right)^2 \right)^{1/3}} + \frac{s}{3\mu^{r/g}} \quad (29)$$

where the temperature θ is provided as input and is used to calculate the current volume ratios of the glassy and rubbery phases according to the relationship to the coefficients of thermal expansion in Equation (25). In addition, the shear moduli are given as input as the values previously calibrated in Section D.

Thus, for a step in which the applied stress, current temperature, and calibration parameters are known, the axial stretch for each phase is determined in a straight-

forward manner. These stretches calculated in Equation (22) are then substituted into the kinematic relationship of Equation (23) to solve for the overall axial stretch. With the current rubbery and glassy stretches calculated, the integral term in Equation (23) is now considered. Note that the integral term contains the derivatives of the glassy volume fraction with respect to temperature and the temperature with respect to time. Thus, at high temperature (i.e., above the transformation temperature range), the glassy volume fraction is zero, there is no contribution to the integral, and the axial stretch of the SMP is equal to that of the rubbery phase. In addition, for isothermal processes and for processes at temperatures lower than the transformation region, there is no contribution to the integral term.

For processes in which the SMP is being cooled through the transformation region, the value of τ (i.e., the time at which the SMP is last cooled through the transformation region) becomes identical to the current time t. The integral is then discretized, using a trapezoidal method, to provide a means of calculating the updated integral as a function of the previous integral value and the current variables. Using the trapezoid method, the value of the integral at time t is given by Equation (30), where (k) and $(k-1)$ represent the quantities at the current and previous time steps, respectively. While the trapezoidal method is not the most precise method for numerical integration, it is relatively simple to implement. By using small increments in this work, the numerical error is reduced and this method is assumed to be sufficient.

$$\begin{aligned}
&\int_0^t \frac{\lambda^r\left(\mathbf{P}(\tau),\theta(\tau)\right)}{\lambda^g\left(\mathbf{P}(\tau),\theta(\tau)\right)}\phi'\left(\theta(\tau)\right)\theta'(\tau)\,d\tau \\
&= \int_0^{t-1} \frac{\lambda^r\left(\mathbf{P}(\tau),\theta(\tau)\right)}{\lambda^g\left(\mathbf{P}(\tau),\theta(\tau)\right)}\phi'\left(\theta(\tau)\right)\theta'(\tau)\,d\tau \\
&+ \frac{\left[\theta^{(k)}-\theta^{(k-1)}\right]}{2}\left[\frac{\lambda^{r^{(k)}}}{\lambda^{g^{(k)}}}\phi'\left(\theta^{(k)}\right)-\frac{\lambda^{r^{(k-1)}}}{\lambda^{g^{(k-1)}}}\phi'\left(\theta^{(k-1)}\right)\right]
\end{aligned} \tag{30}$$

Assuming the derivative of the glassy volume fraction is equal to zero as an initial condition at the start of cooling, the value of the integral during the first cooling increment reduces to a function only of the rubbery and glassy phase stretches and the derivative of the glassy volume fraction at the current time, as shown in Equation (31). By determining the value of the integral in this first cooling step, the results are used to calculate the results of the subsequent steps in Equation (30).

$$\int_0^{t_1} \frac{\lambda^r\left(\mathbf{P}(\tau),\theta(\tau)\right)}{\lambda^g\left(\mathbf{P}(\tau),\theta(\tau)\right)}\phi'\left(\theta(\tau)\right)\theta'(\tau)\,d\tau = \frac{\lambda^{r^{(1)}}}{\lambda^{g^{(1)}}}\phi'\left(\theta^{(1)}\right)\theta^{(1)} \tag{31}$$

During heating, the integral term is known from the history during cooling. The kinematics used in the work assume the SMP has fully recovered its stored deformation when it is reheated through the same temperature range [115]. Thus, the integral term in Equation (23) is rewritten as Equation (32), where $s(t) < t$ and $\theta\left(s(t)\right) = \theta(t)$. Physically, $s(t)$ represents the last time that the material was at the current temperature and was being cooled through the transformation region.

$$\int_0^t \frac{\lambda^r\left(\mathbf{P}(\tau),\theta(\tau)\right)}{\lambda^g\left(\mathbf{P}(\tau),\theta(\tau)\right)}\phi'\left(\theta(\tau)\right)\theta'(\tau)\,d\tau = \int_0^{s(t)} \frac{\lambda^r\left(\mathbf{P}(\tau),\theta(\tau)\right)}{\lambda^g\left(\mathbf{P}(\tau),\theta(\tau)\right)}\phi'\left(\theta(\tau)\right)\theta'(\tau)\,d\tau \tag{32}$$

Substituting this relationship into the kinematics of Equation (23) results in Equation (33), which describes the axial stretch during the heating process.

$$\lambda = \left[1-\phi\left(\theta\right)\right]\lambda^{r}\left(\mathbf{P},\theta\right)+\lambda^{g}\left(\mathbf{P},\theta\right)\int_{0}^{s(t)}\frac{\lambda^{r}\left(\mathbf{P}\left(\tau\right),\theta\left(\tau\right)\right)}{\lambda^{g}\left(\mathbf{P}\left(\tau\right),\theta\left(\tau\right)\right)}\phi'\left(\theta\left(\tau\right)\right)\theta'\left(\tau\right)d\tau \qquad (33)$$

With the methods established to handle the integral term during heating and cooling, the system of equations, for a given stress and temperature input, are well defined and programmed in the 1D MATLAB® code.

III.E.2. Stretch Controlled Processes

The previous section described the methodology used to predict the response of a SMP for steps in which the stress and temperature of the material are given as input and the stretch is the output. This section considers the alternate scenario – steps in which the stretch and temperature is given as input, but the stress is the output. Recall the stress is not explicitly described a function that is in terms of all known variables. Rather, the stress is included in the functional dependence for the glassy and rubbery axial stretches in addition to the constraint that the stress is assumed to be equal between the two phases.

The approach used to solve for the stress in a stretch-controlled step is to first simplify the kinematic relationship to remove the integral term. Then, the resulting differential equation is solved simultaneously with the constitutive equations to calculate the updated state of the material.

First, the inverse of the glassy axial stretch is multiplied through the kinematic relationship in Equation (23) to isolate the integral in the last term of the equation.

$$\frac{\lambda}{\lambda^g\left(\mathbf{P},\theta\right)}=\left[1-\phi\left(\theta\right)\right]\frac{\lambda^r\left(\mathbf{P},\theta\right)}{\lambda^g\left(\mathbf{P},\theta\right)}+\int_0^t\frac{\lambda^r\left(\mathbf{P}\left(\tau\right),\theta\left(\tau\right)\right)}{\lambda^g\left(\mathbf{P}\left(\tau\right),\theta\left(\tau\right)\right)}\phi'\left(\theta\left(\tau\right)\right)\theta'\left(\tau\right)d\tau \tag{34}$$

Equation (34) is then differentiated with respect to time and the fundamental theorem of calculus is used on the integral term.

$$\begin{aligned}\frac{d}{dt}\left(\frac{\lambda}{\lambda^g\left(\mathbf{P},\theta\right)}\right)&=\frac{d}{dt}\left(\left[1-\phi\left(\theta\right)\right]\frac{\lambda^r\left(\mathbf{P},\theta\right)}{\lambda^g\left(\mathbf{P},\theta\right)}\right)\\&+\frac{\lambda^r\left(\mathbf{P}\left(t\right),\theta\left(t\right)\right)}{\lambda^g\left(\mathbf{P}\left(t\right),\theta\left(t\right)\right)}\phi'\left(\theta\left(t\right)\right)\theta'\left(t\right)\\&-\frac{\lambda^r\left(\mathbf{P}\left(0\right),\theta\left(0\right)\right)}{\lambda^g\left(\mathbf{P}\left(0\right),\theta\left(0\right)\right)}\phi'\left(\theta\left(0\right)\right)\theta'\left(0\right)\end{aligned} \tag{35}$$

Expanding the time derivative on the right hand side of the first line of Equation (35) results in a term that cancels with the second line. Equation (36) is then the result of combining this result with the initial condition that the derivative of the glassy volume fraction at $t=0$ is equal to zero, which eliminates the third line of Equation (35).

$$\frac{d}{dt}\left(\frac{\lambda}{\lambda^g\left(\mathbf{P},\theta\right)}\right)=\left[1-\phi\left(\theta\right)\right]\frac{d}{dt}\left(\frac{\lambda^r\left(\mathbf{P},\theta\right)}{\lambda^g\left(\mathbf{P},\theta\right)}\right) \tag{36}$$

Using a Backward Euler method [113] and the product rule, the differential equation in Equation (36) is rewritten as Equation (37).

$$\begin{aligned}&\frac{1}{\lambda^{g^{(k)}}}\left(\frac{\lambda^{(k)}-\lambda^{(k-1)}}{\Delta t}\right)-\frac{\lambda^{(k)}}{\left(\lambda^{g^{(k)}}\right)^2}\left(\frac{\lambda^{g^{(k)}}-\lambda^{g^{(k-1)}}}{\Delta t}\right)\\&=\left[1-\phi\left(\theta\right)\right]\left[\frac{1}{\lambda^{g^{(k)}}}\left(\frac{\lambda^{r^{(k)}}-\lambda^{r^{(k-1)}}}{\Delta t}\right)-\frac{\lambda^{r^{(k)}}}{\left(\lambda^{g^{(k)}}\right)^2}\left(\frac{\lambda^{g^{(k)}}-\lambda^{g^{(k-1)}}}{\Delta t}\right)\right]\end{aligned} \tag{37}$$

where the superscripts (k) and $(k-1)$ represent the current and previous time steps, respectively. Equation (37) is then further simplified to Equation (38) through the elimination of cancelling terms as well as the elimination of the Δt parameter in each term. Note that the elimination of Δt is expected as the model was developed as a rate-independent model such that the material response should not depend on the time.

$$\left(\frac{\lambda^{g^{(k-1)}}}{\lambda^{g^{(k)}}}\right)\lambda^{(k)} - \lambda^{(k-1)} = \left[1-\phi(\theta)\right]\left[\left(\frac{\lambda^{g^{(k-1)}}}{\lambda^{g^{(k)}}}\right)\lambda^{r^{(k)}} - \lambda^{r^{(k-1)}}\right] \tag{38}$$

The unknowns in Equation (38) are current step rubbery and glassy axial stretches, $\lambda^{r^{(k)}}$ and $\lambda^{g^{(k)}}$, respectively. For the first increment, the initial conditions $\lambda^{r^{(0)}}$ and $\lambda^{g^{(0)}}$ are prescribed to be equal to 1 (i.e., the initial configuration for the rubbery and glassy phases is the undeformed configuration).

Equation (38) represents the discretized kinematic relationship between the total axial stretch and the axial stretches of the rubbery and glassy phases. In addition to this equation, Equation (39) represents the constraint between the stresses of the rubbery phase and the glassy phase. Specifically, as a result of assuming spatially constant stress in the body, the constitutive equations of Equation (22) are set equal to result in Equation (39).

$$\mu^r\left(\lambda^{r^{(k)}} - \frac{\upsilon^r\left(\theta^{(k)}\right)}{\left(\lambda^{r^{(k)}}\right)^2}\right) = \mu^g\left(\lambda^{g^{(k)}} - \frac{\upsilon^g\left(\theta^{(k)}\right)}{\left(\lambda^{g^{(k)}}\right)^2}\right) \tag{39}$$

Equations (38) and (39) form a nonlinear system of equations with $\lambda^{r^{(k)}}$ and $\lambda^{g^{(k)}}$ as the unknowns. These equations are solved using the Newton Method for solving nonlinear equations. In this method, of which the full details are described in [122], a matrix equation is set up as shown in Equation (40).

$$[J]\left\{\partial\lambda^{r/g^{(k)}}\right\} = \{R\} \tag{40}$$

In this system, the 2x2 Jacobian matrix J is composed of the partial derivatives of the equations with respect to the unknowns, the 2x1 unknowns vector consists of increments to $\lambda^{r^{(k)}}$ and $\lambda^{g^{(k)}}$, respectively, and the 2x1 vector on the right hand side is the residual vector R, which contains the residual of the equations when solved using the guess solution. The components of the Jacobian, after rearranging Equations (38) and (39) such that right hand side of the equation is set equal to zero, are calculated with the results shown in Equation (41).

$$\begin{aligned}
J_{11} &= -\frac{\lambda^{g^{(k-1)}}\lambda^{(k)}}{\left(\lambda^{g^{(k)}}\right)^2} + \left[1-\phi\left(\theta^{(k)}\right)\right]\frac{\lambda^{g^{(k-1)}}\lambda^{r^{(k)}}}{\left(\lambda^{g^{(k)}}\right)^2} & J_{21} &= \mu^g\left(1+\frac{2\upsilon^g\left(\theta^{k)}\right)}{\left(\lambda^{g^{(k)}}\right)^3}\right) \\
J_{12} &= -\left[1-\phi\left(\theta^{(k)}\right)\right]\left(\frac{\lambda^{g^{(k-1)}}}{\lambda^{g^{(k)}}}\right) & J_{22} &= \mu^r\left(1+\frac{2\upsilon^r\left(\theta^{(k)}\right)}{\left(\lambda^{r^{(k)}}\right)^3}\right)
\end{aligned} \tag{41}$$

The equations for the residual vector are presented in Equation (42), where the first equation represents the kinematic relationship and the second equation represents the constraint equating the stress in the rubbery and glassy phases.

$$R_1 = \left(\frac{\lambda^{g^{(k-1)}}}{\lambda^{g^{(k)}}} \right) \lambda^{(k)} - \lambda^{(k-1)} - \left[1 - \phi\left(\theta^{(k)}\right) \right] \left[\left(\frac{\lambda^{g^{(k-1)}}}{\lambda^{g^{(k)}}} \right) \lambda^{r^{(k)}} - \lambda^{r^{(k-1)}} \right]$$

$$R_2 = \mu^r \left(\lambda^{r^{(k)}} - \frac{\upsilon^r\left(\theta^{(k)}\right)}{\left(\lambda^{r^{(k)}}\right)^2} \right) - \mu^g \left(\lambda^{g^{(k)}} - \frac{\upsilon^g\left(\theta^{(k)}\right)}{\left(\lambda^{g^{(k)}}\right)^2} \right) \tag{42}$$

The Newton Method, which seeks to minimize the residuals in the system of equations, is solved using the previous converged (or initial) value as the starting guess for $\lambda^{r^{(k)}}$ and $\lambda^{g^{(k)}}$. The system of equations presented in Equation (40) is solved iteratively until the increments to the unknowns have converged and are no longer changing. Once the values for the rubbery and glassy stretches are obtained, the stress of the SMP is calculated by substituting these values back into the constitutive equations in Equation (22). Note that, consistent with the assumption of the stresses in the two phases being equal, the constitutive equation for only one of the phases needs to be solved for the new stress.

III.F. Modeling Results

After calculating the parameters necessary to calibrate the constitutive model, the 10% extension free recovery experiment from which the material properties were calculated was first simulated and then the model was validated by comparing the model predictions to the experimental data for the 15%, 20%, and 25% extension free recovery experiments and the 10%, 15%, 20%, and 25% constrained displacement recovery experiments.

III.F.1. Simulation of Calibration Experiment

The simulation of the 10% extension free recovery experiment from which the material properties were calibrated is presented in a three-dimensional extension-stress-temperature plot in Figure 20. It is observed that the model predictions (shown in blue) match well with the experimental data (shown in black) in all steps of the thermomechanical load path.

In addition to the 3-D plot, Figure 21 – Figure 23 present the two-dimensional projections of the data. Figure 21 first presents the stress-extension response as compared to the model simulation. It is observed that the model simulation captures the stress-extension response during loading, which supports the choice of modeling the material behavior as a neo-Hookean material[3].

Figure 22 presents the stress-temperature response for the model simulation and the experimental data. In performing the simulations, the extension increase during constrained cooling (cf. Section 2.2 in Chapter II) from 90°C to 25°C was approximated as a linear function. It is observed that the model simulation matches well with the experimental data. In particular, the model captures well the onset of the large stress increase that initiates around 65°C during the cooling step. This agreement is primarily a result of using a piecewise hyperbolic tangent to calibrate the glassy volume fraction.

[3] While the neo-Hookean representation of the material response appears sufficient for this material system, new constitutive equations may need to be derived and implemented in future efforts for materials that exhibit more nonlinearity, larger deformations, and/or stiffening.

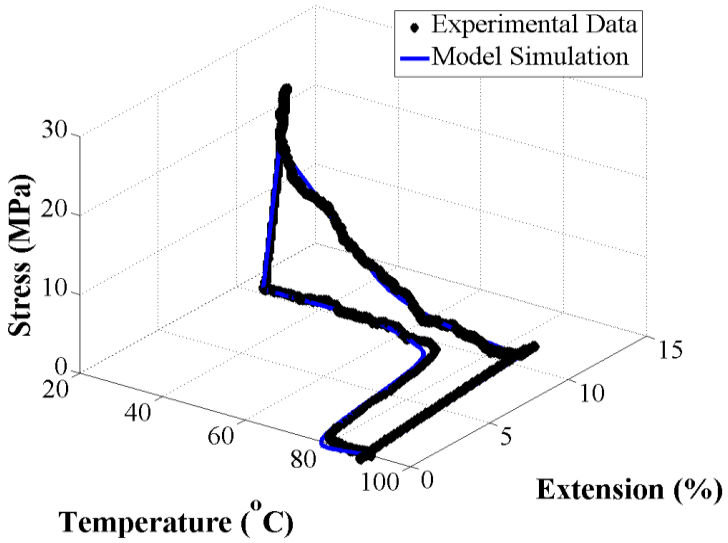

Figure 20 –Simulation of the 10% extension free recovery experiment, presented in extension-stress-temperature space and compared to experimental data, from which the material properties and glassy volume fraction were calibrated.

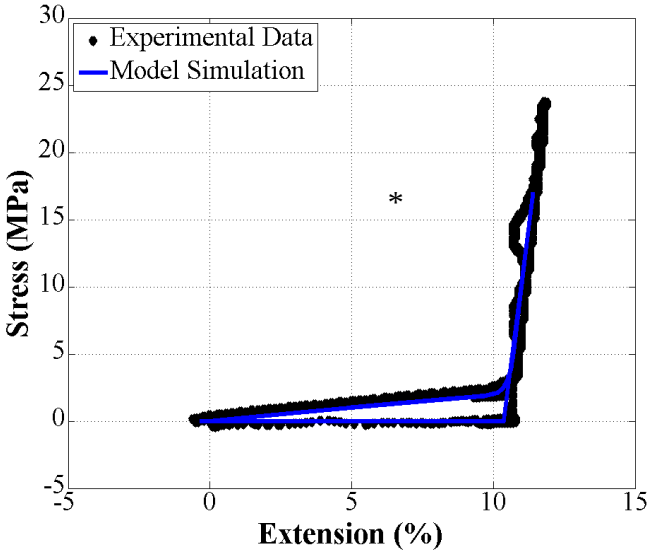

Figure 21 – Stress-extension comparison between the model simulation and the experimental data for the 10% extension free recovery experiment from which the material properties and glassy volume fraction were calibrated. The asterisk * denotes an example of oscillations in the experimental data as the PID system attempts to maintain a constant extension during cooling through the glass transition.

By using a single hyperbolic tangent, the transition from the rubbery to the glassy phase (upon cooling) would have completed at a higher temperature and the resulting stresses during cooling would have been higher (~25%) than the current simulation. In addition to the piecewise hyperbolic tangent, it is recalled that the coefficient of thermal expansion for the glassy phase was calibrated to this stress-temperature data experimental during cooling. In particular, the glassy CTE was adjusted such that the slope of the linear region in the model simulations during cooling from 50°C to 25°C (i.e., the cooling that occurred after the phase transition was complete) matched well with the experimental data.

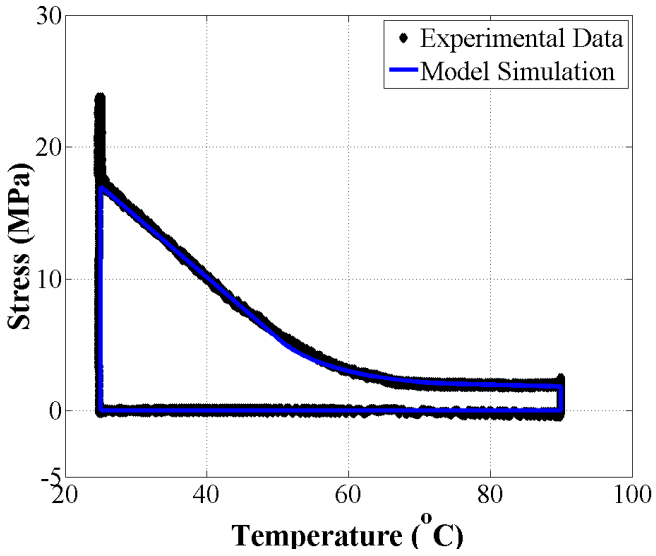

Figure 22 – Stress-temperature comparison between the model simulation and the experimental data for the 10% extension free recovery experiment from which the material properties and glassy volume fraction were calibrated.

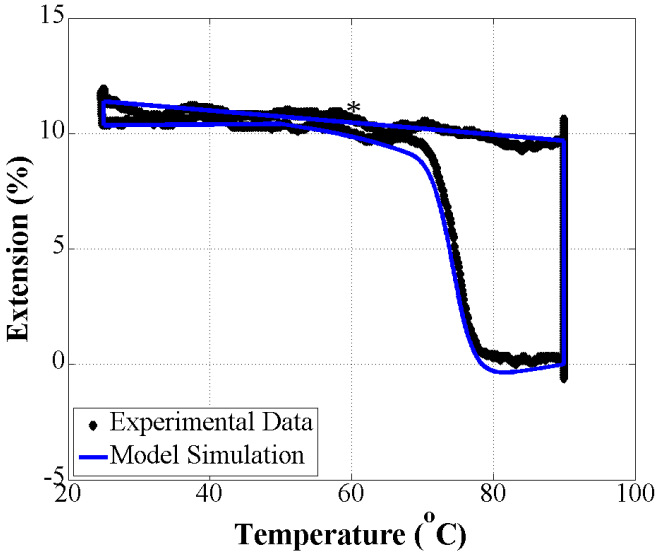

Figure 23 – Extension-temperature comparison between the model simulation and the experimental data for the 10% extension free recovery experiment from which the material properties and glassy volume fraction were calibrated. The asterisk * denotes an example of oscillations in the experimental data as the PID system attempts to maintain a constant extension during cooling through the glass transition.

Finally, Figure 23 presents the extension-temperature response for the 10% extension free recovery experiment as simulated by the 1-D model and compared to the experimental data. Note that the extension in the simulation increases linearly during cooling from 90°C to 25°C. This linear increase, which represents an approximation to the actual oscillating behavior seen experimentally, was the input to the model during the cooling step as previously described. In addition, it is observed that the simulation matches well with the experimental data during the zero load recovery heating from 25°C to 90°C. In particular, the onset temperature, qualitative shape of recovery, and completion temperature of the shape recovery matches well between the simulations and the experimental data. Small differences are observed, however, in comparing the

curves at the onset and completion of the extension recovery. These differences may be reduced by optimizing the temperature range across which the glassy volume fraction is calibrated or by considering the thermal expansion effects, which were neglected in this calibration, when calibrating the glassy volume fraction. As expected, the simulation indicates the material recovers all of the applied deformation. This assumption is supported upon comparison to the experimental data in this figure and the data tabulated in Table 4.

III.F.2. Free Recovery Predictions

After simulating the 10% extension free recovery experiment, from which the material properties were calibrated, the model was used to predict the 15%, 20%, and 25% extension free recovery experiments that were presented in Figure 10. Figure 24 – Figure 26 present the three-dimensional extension-temperature-stress predictions for the 15%, 20%, and 25% extension experiments, where the black dash, dotted, and solid lines represent the predicted results. It is observed that the model predictions match well with the experimental data in all cases. Further investigation into the comparison between the model predictions and the experimental data is presented in the two-dimensional projections shown in Figure 27 – Figure 29.

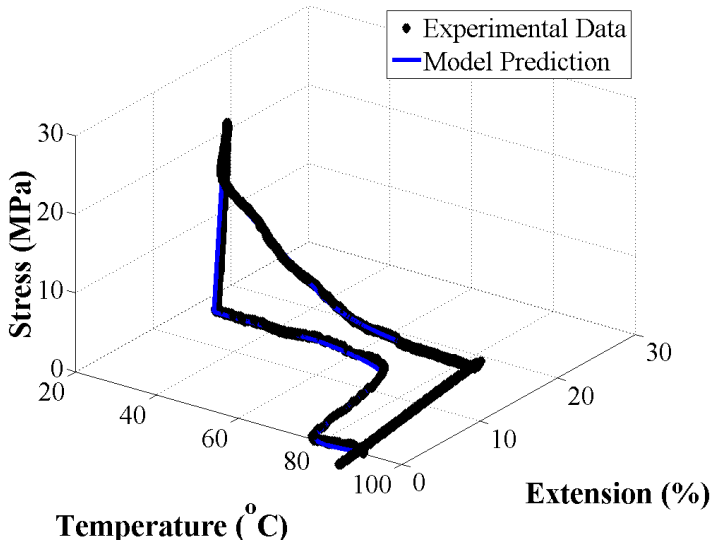

Figure 24 – Prediction of the 15% extension free recovery experiment, presented in extension-stress-temperature space and compared to experimental data.

Figure 27 presents the two-dimensional projections in stress-extension space. It is observed that the predictions for the stress as a function of the applied extension match well with the experimental data for all values of applied extension. As presented in the experimental data of Chapter II (cf. Figure 12(a) and Table 2), the stress-extension response of this polyurethane SMP is approximately linear for all values of extension, and the variation (i.e., range) in the rubbery phase modulus is less than 10% of the average rubbery modulus. As such, these results agree with the expectation that the neo-Hookean constitutive behavior, which is a relatively simple constitutive model, should be able to adequately capture the response of the material for the extension range in consideration and for the material system which displays relatively consistent behavior from sample-to-sample.

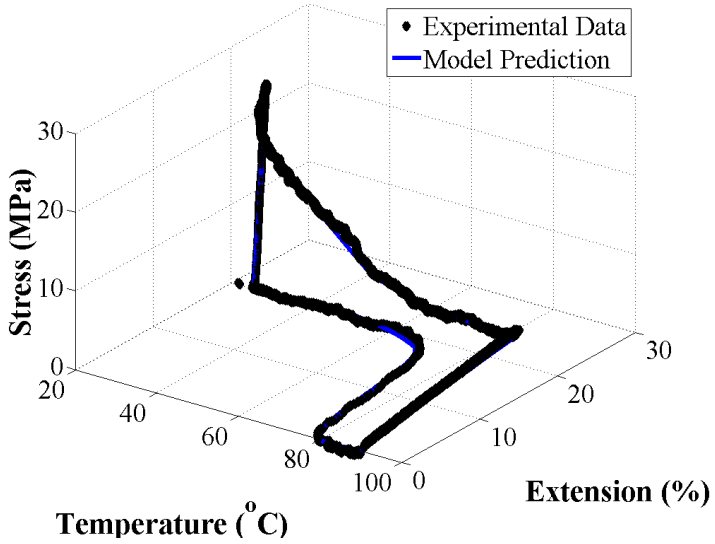

Figure 25 – Prediction of the 20% extension free recovery experiment, presented in extension-stress-temperature space and compared to experimental data.

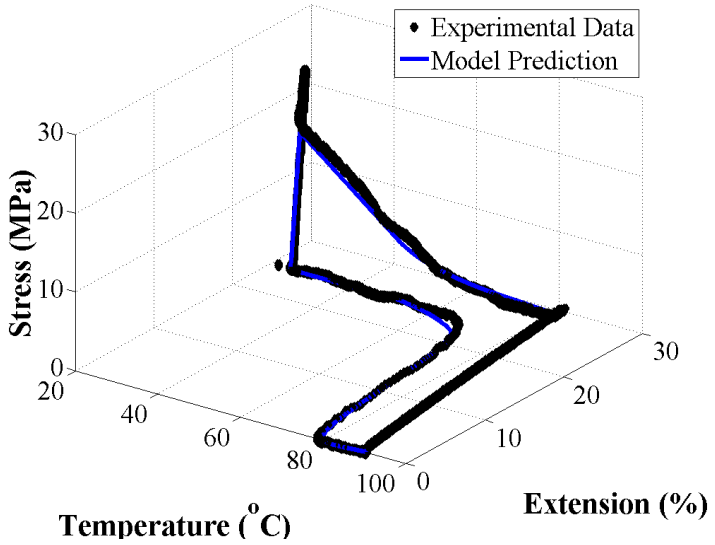

(c)

Figure 26 – Prediction of the 25% extension free recovery experiment, presented in extension-stress-temperature space and compared to experimental data.

In addition, Figure 28 presents the stress-temperature response of the 15%, 20%, and 25% extension cases as compared to the model predictions. It is observed that the model is able to predict well the response of the SMP for all three values of applied extensions. In addition to matching the general trend of the stress increase during cooling, the value of the stress at the end of cooling is near that of the experiments. The differences in the end values are likely due to variations in the material properties. Specifically, there may be small differences in the coefficients of thermal expansion, glassy modulus, or glass transition temperature that would in a different stress increase when cooled through the same temperature range. Further, the error in the laser extensometer readings may influence the model predictions. Due to the resolution of the laser extensometer being ~0.3% strain, a potential source of error is in the linear

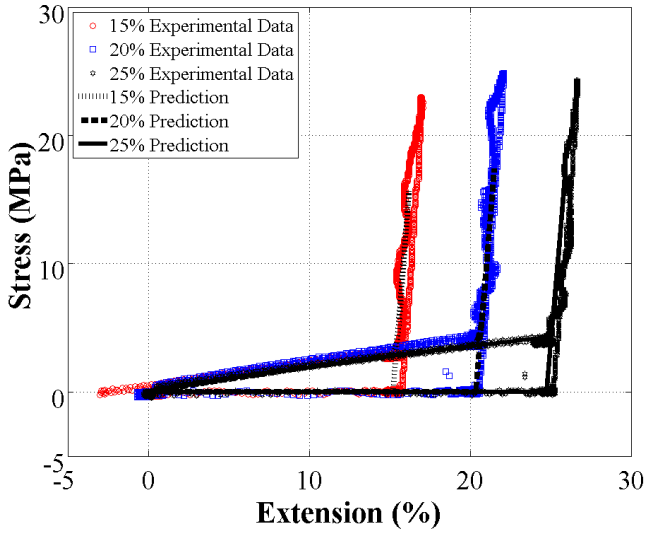

Figure 27 – Stress-extension model predictions compared to the experimental data for the 15%, 20%, and 25% extension free recovery experiments.

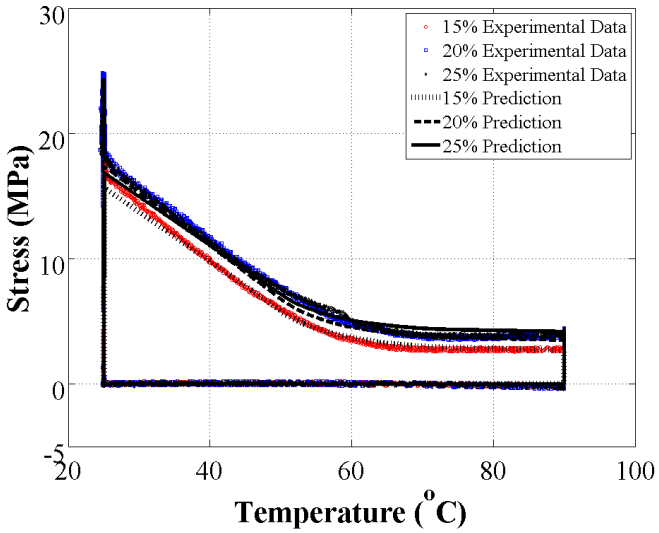

Figure 28 – Stress-temperature model predictions compared to the experimental data for the 15%, 20%, and 25% extension free recovery experiments.

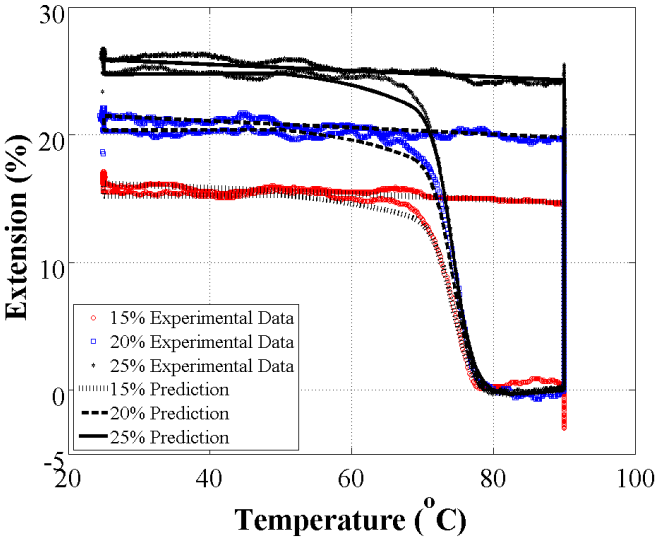

Figure 29 – Extension-temperature model predictions compared to the experimental data for the 15%, 20%, and 25% extension free recovery experiments.

approximation used to model the extension increase during cooling for each experiment.

The final two-dimension comparison for the free recovery mode predictions is shown in Figure 29, which presents the extension-temperature response of the SMP for the three predicted values of applied extension. It is observed that the model predictions match well with the experimental data. Specifically, the model is able to predict well the transformation temperatures and the general shape recovery trend. The largest difference between the predictions and experiments appears at the onset of recovery. This difference is likely due to small differences in the material properties and/or the shape of the onset of shape recovery (cf. Figure 14(b)), to which the glassy volume fraction is fit and is a critical calibration parameter in predicting the response of the SMP. The assumption of no irrecoverable deformation in the model results in all of the applied extension being recovered in the predictions, which match well with the results observed experimentally.

III.F.3. Constrained Displacement Recovery Predictions

In addition to predicting the free recovery experiments, the calibrated model was used to predict the constrained recovery experiments (cf. Figure 11) for all four values of applied extension – 10%, 15%, 20%, and 25%. The three-dimensional predictions for the constrained recovery experiments are presented in Figure 30. While the figure indicates good agreement between the predictions and the experiments, Figure 31 – Figure 33 present the two-dimensional projections, including a better comparison for the stress recovery as a function of temperature.

Figure 31 presents the extension-temperature comparison for the four values of applied extension. While it is observed that the predictions match well with the experimental data, it is noted that the extension increase during cooling and decrease

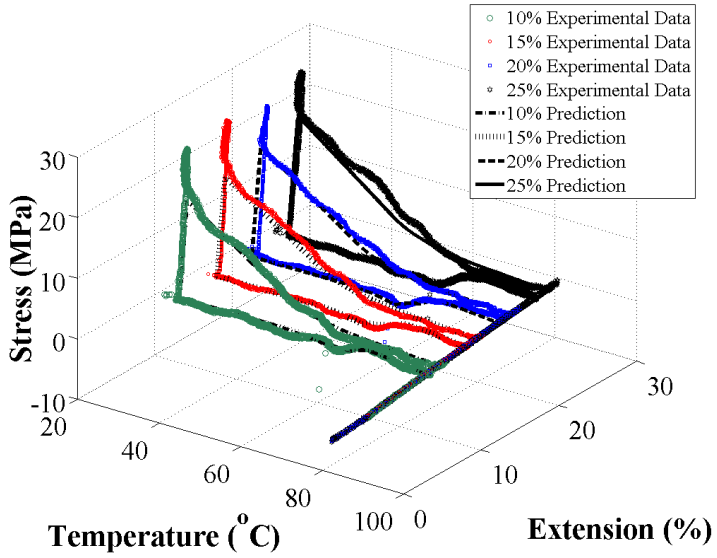

Figure 30 – Prediction of the 10%, 15%, 20%, and 25% extension constrained displacement recovery experiments, presented in extension-stress-temperature space and compared to experimental data

during heating are actually used as input to the model. Specifically, a linear approximation is used to model the extension increase during the constrained cooling. In heating from 25°C to 60°C, the model maintains zero load. Thus, the extension during this temperature range of heating is a prediction. However, at 60°C (i.e., when the bottom of the specimen is regripped in the experiments), the extension decrease observed while heating from 60°C to 90°C is approximated using a linear function and

subsequently used as input to the model. Thus, as expected, the overall predictions for the extension as a function of temperature match well with the experimental data.

In addition, Figure 32 presents the stress-temperature results for the four experimental cases. It is observed that the predictions match reasonably well with the experimental data. Specifically, the predictions capture the onset of the phase transition when cooling from the rubbery phase to the glassy phase. Although matching the qualitative trend well, there are deviations in the stress prediction during this constrained cooling step (~5-11% error in the value at the end of cooling). These deviations are likely a result of variations in the oscillations of the PID system attempting to maintain a constant extension during the constrained cooling.

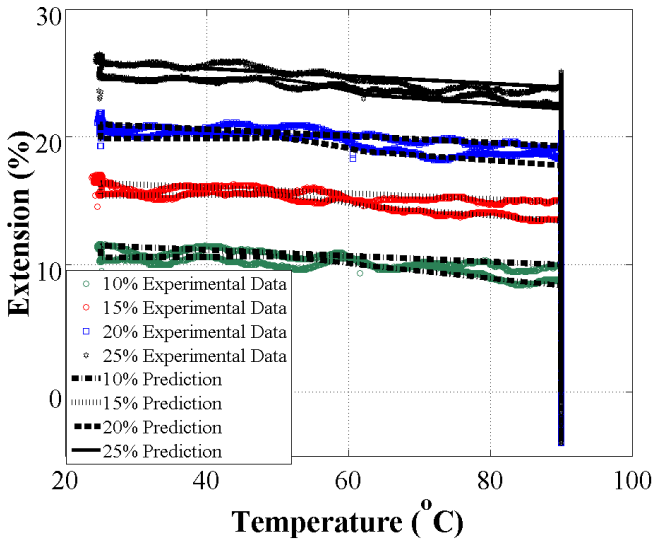

Figure 31 – Extension-temperature model predictions compared to the experimental data for the 10%, 15%, 20%, and 25% extension constrained displacement recovery experiments.

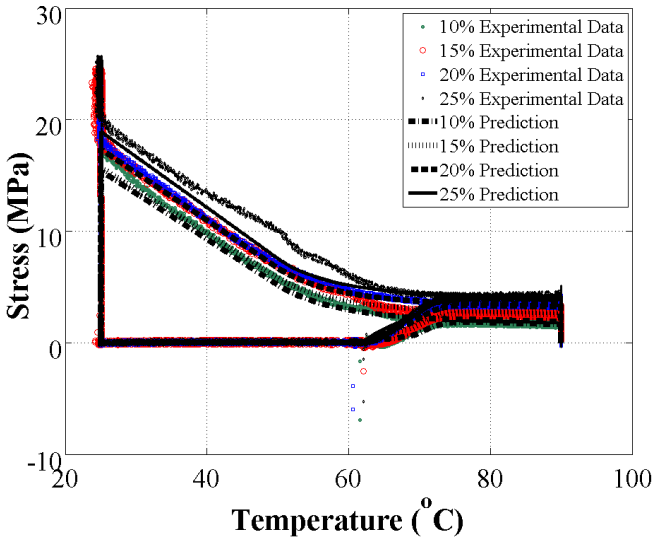

Figure 32 – Stress-temperature model predictions compared to the experimental data for the 10%, 15%, 20%, and 25% extension constrained displacement recovery experiments.

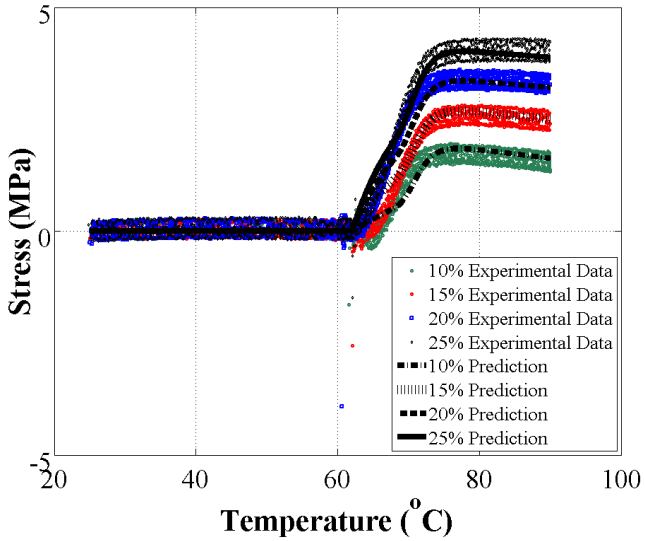

Figure 33 – Stress-temperature model predictions, during the recovery heating step, compared to the experimental data for the 10%, 15%, 20%, and 25% extension constrained displacement recovery experiments.

Finally, in Figure 33, the stress-temperature results during the constrained displacement recovery are presented. These results are a subset of the results shown in Figure 32with focus on just the final step in the thermomechanical path. It is observed that the model is able to predict well the recovery temperature and recovery stresses for each of the four extension values. There is some deviation in the comparison at the start of the recovery, in which the model predicts a more gradual increase in the stress as function of temperature. This deviation is likely due to the piecewise form of the glassy volume fraction as well as the experimental procedure, in which the crosshead was manually adjusted to keep the stress at zero for a few degrees after closing the bottom grip.

III.G. Summary and Conclusions

In this work, a large deformation model for modeling shape memory polymers was implemented in 1-D. The kinematics, formulated in terms of the deformation gradients, assumed a mixture of the rubbery and the glassy phases. A glassy volume fraction was introduced as an internal state variable to quantify the amount of the material that is in the glassy phase, and the average state variables were obtained by performing a volume average on the mixture of the rubbery and glassy phases. Consistent with the assumption of constant stress in the representative volume element, the rotations of the rubbery and glassy phases were assumed to be equal to that of the average rotation, and the expression for the average deformation gradient was reduced to an expression for the average stretch in the SMP. Motivated by the experimental results

of Chapter II, this glassy volume fraction is assumed to be only a function of temperature.

The constitutive response was defined for each the rubbery and glassy phases and assumed to take the form of an incompressible neo-Hookean material. The resulting constitutive equations related the stress to the deformation gradient and the hydrostatic pressure required to maintain incompressibility. After performing the polar and spectral decompositions, the system of equations was reduced to their one-dimensional form. By considering uniaxial deformations, the indeterminate hydrostatic pressure term in the constitutive equations was eliminated, and the constitutive equations in each phase were reduced to the stress in terms of the principal stretch. The equations were then implemented in MATLAB® in a general, incremental formulation that provides the ability to solve for the state of the material for steps in which either the displacement or the stress is provided.

The system of equations, including the kinematics and the compressible neo-Hookean constitutive equations, required five calibration parameters – the rubbery and glassy phase shear moduli, the rubbery and glassy coefficients of thermal expansion (CTEs), and a function for the glassy volume fraction as a function of temperature. The results from the 10% extension free recovery experiment in Chapter II were used to calibrate the necessary parameters. Specifically, the rubbery and glassy tensile moduli were calculated from the high temperature loading and low temperature unloading steps, respectively. The shear moduli were then calculated from the tensile modulus and the assumption of incompressible material response (Poission's ratios = 0.5). In addition,

the coefficients of thermal expansion and the glassy volume fraction were calculated from 10% free recovery experiment. The rubbery CTE was calculated from the strain-temperature response during zero load heating, and the glassy CTE was calculated to match the stress-temperature increase observed during constrained cooling. Finally, the glassy volume fraction was assumed to take the shape of the free recovery strain profile. As such, a hyperbolic tangent function was introduced, and the constants were calculated using a least squares method when compared to the normalized free recovery profile. A piecewise hyperbolic tangent was necessary to precisely fit the onset of shape recovery, which is a key parameter affecting the stress predictions during constrained cooling.

After calibrating the necessary parameters and observing good agreement of the model simulation with the experimental data, the model was then used to predict the 15%, 20%, and 25% extension free recovery experiments as well as the 10%, 15%, 20%, and 25% extension constrained displacement recovery experiments. The model predictions were observed to have good agreement with the experimental data, with minor differences likely due to variations in the material properties and phase transformation behavior between specimens.

CHAPTER IV

NUMERICAL IMPLEMENTATION OF A THREE-DIMENSIONAL CONSTITUTIVE MODEL FOR SHAPE MEMORY POLYMERS

The previous two chapters presented uniaxial experiments and one-dimensional constitutive modeling of a polyurethane shape memory polymer. A subset of experimental data was used to calibrate the material properties used in the model, and the model was then used to predict the response for the other uniaxial load paths. This chapter expands on this framework and presents the three-dimensional modeling of shape memory polymers. Using the kinematic framework established in the previous chapter, new constitutive equations are derived to provide a more general analysis tool for modeling the compressible behavior of SMPs. The resulting equations are then numerically implemented in a user material subroutine (UMAT) in Abaqus, a commercially available finite element software. Following the numerical implementation and calibration of material properties, example three-dimensional analyses – including the effects of the heat transfer on the shape recovery – are presented.

IV.A. Kinematics

The three-dimensional modeling efforts in this work build upon the kinematic framework established in Section A of Chapter III and in [122], in which a relationship between the average deformation gradient and the deformation gradient of the constituent rubbery and glassy phases is established.

IV.A.1. Average Deformation Gradient

In these kinematics, the shape memory polymer is assumed to have a rubbery, stress-free reference configuration (i.e., the temperature is sufficiently high that the material is in a pure rubbery state). Upon cooling the material to below the glass transition temperature range, the material enters a pure glassy state. At intermediate temperatures, the material is assumed to be a mixture of the rubbery and glassy phases with a spatially constant stress. It is further assumed that the rubbery and glassy phases undergo only rate-independent elastic and thermal strains. In other words, no dependence on the strain rate or temperature rate is considered, and no permanent, irrecoverable deformations are considered. To model this behavior, the kinematics first considers individual material particles that undergo transformation from the rubbery phase to the glassy phase at a discrete temperature. Then, the average deformation gradient is obtained through performing a volume average of all of the particles in the glassy and rubbery phases. A glassy volume fraction is introduced and prescribed to represent the percentage of the material that has transformed, at a given temperature, to the glassy phase. Equation (5), presented here as Equation (43), presents the equation for the average deformation gradient **F**

$$\begin{aligned}\mathbf{F} &= \left[1-\phi\left(\theta\right)\right]\mathbf{F}_e^r\left(\mathbf{P},\theta\right) \\ &\quad +\mathbf{F}_e^g\left(\mathbf{P},\theta\right)\int_0^t \mathbf{F}_{nat}\left(\mathbf{P}(\tau),\theta(\tau)\right)\phi'\left(\theta\left(\tau\right)\right)\theta'\left(\tau\right)d\tau\end{aligned} \tag{43}$$

where $\mathbf{F}_e^r\left(\mathbf{P},\theta\right)$ and $\mathbf{F}_e^g\left(\mathbf{P},\theta\right)$ are the rubbery and glassy elastic deformation gradients, which are functions of stress $\mathbf{P}$ and temperature θ . In addition, $\mathbf{F}_{nat}$ represents the

deformation that is stored when cooling from the rubbery phase to the glassy phase, defined through Equation (2), and $\phi(\theta)$ is the glassy volume fraction as a function of temperature.

Using the polar decomposition and the assumption on the rotations of the individual phases presented in Chapter III, the average deformation gradient of Equation (43) was subsequently reduced to an expression for the average stretch of the SMP as a function of the stretches of the rubbery and glassy phases. This expression, provided as Equation (8) in Chapter III, is recalled here as Equation (44).

$$\begin{aligned}\mathbf{U} &= \left[1-\phi(\theta)\right]\mathbf{U}_e^r(\mathbf{P},\theta) \\ &\quad +\mathbf{U}_e^g(\mathbf{P},\theta)\int_0^t \mathbf{U}_{nat}\left(\mathbf{P}(\tau),\theta(\tau)\right)\phi'\left(\theta(\tau)\right)\theta'(\tau)\,d\tau\end{aligned} \tag{44}$$

IV.A.2. Heating Evolution Equation

The kinematic relationships of Equations (43) and (44) describes how the shape memory polymer responds to changes in stress and temperature, which are dependent variables in the rubbery and glassy deformation gradients as well as the glassy volume fraction. The integral term represents the stored deformation at a current time *t*. Physically, this integral term indicates that deformation is stored when the material is being cooled from the rubbery phase to the glassy phase. Specifically, τ represents the last time the material was at the current temperature $\left(\theta(t)\right)$ *and* was being actively cooled $\left(\phi'(\theta)\neq 0\right)$. In other words, thermomechanical deformations in the pure rubbery

$\left(\phi(\theta)=0,\ \phi'(\theta)=0\right)$ or pure glassy state $\left(\phi(\theta)=1,\ \phi'(\theta)=0\right)$ do not contribute the stored deformation. Similarly, isothermal deformations at an intermediate temperature $\left(0<\phi(\theta)<1,\ \theta'(t)=\phi'(\theta)=0\right)$ do not contribute to the stored deformation until cooling is resumed.

During heating, Equation (44) can be rewritten as Equation (45), in which $s(t)<t$ such that $\theta\left(s(t)\right)=\theta(t)$. In other words, $s(t)$ is the most recent time previous to the current time in which the SMP experienced the same temperature. The consequence of this assumption is that, during heating, it is assumed that the material returns to exactly the same configuration as it experienced when it was cooled through the same temperature. Practically, this assumption necessitates the storage of the state of the SMP during each cooling step and the subsequent lookup of these states during the heating procedure. For large systems or complex analyses, a large number of values would need to be stored, which would adversely affect storage and run times.

$$\begin{aligned}\mathbf{U}=&\left[1-\phi(\theta)\right]\mathbf{U}_e^r(\mathbf{P},\theta)\\&+\mathbf{U}_e^g(\mathbf{P},\theta)\int_0^{s(t)}\mathbf{U}_{nat}\left(\mathbf{P}(\tau),\theta(\tau)\right)\phi'\left(\theta(\tau)\right)\theta'(\tau)\,d\tau\end{aligned}\tag{45}$$

This work considers an alternative approach to calculating the shape recovery during heating. In this approach, an evolution equation is introduced for the recovery of the stored deformation, where Equation (46) represents the average stored deformation during cooling.

$$\mathbf{U}^{stor}=\int_0^t\mathbf{U}_{nat}\left(\mathbf{P}(\tau),\theta(\tau)\right)\phi'\left(\theta(\tau)\right)\theta'(\tau)\,d\tau\tag{46}$$

During the heating step, it is then assumed that the stored deformation recovers proportional to the glassy volume fraction, as shown in Equation (47). It is noted, however, that the material does not need to complete transformation to the glassy phase before recovery heating can initiate. Thus, Equation (47) is normalized through the use of $\mathbf{U}_{rev}^{stor}$ and ϕ_{rev}, which represent the value of the stored deformation and the glassy volume fraction, respectively, when the cooling ceased and the subsequent heating began. It is observed that this form of an evolution equation has recently been used in the modeling of other shape memory materials [113].

$$\dot{\mathbf{U}}^{stor} = \frac{\mathbf{U}_{rev}^{stor}}{\phi_{rev}} \dot{\phi}(\theta) \qquad \dot{\phi}(\theta) < 0 \tag{47}$$

IV.B. Constitutive Equations

Equations (43) and (44) present the average deformation gradient and average stretch, respectively, as a function of the rubbery and glassy elastic deformation gradients. In addition to the kinematic description of the SMP behavior, constitutive equations must be defined for the shape memory polymer and the rubbery and glassy phases. In this work, the stress in the SMP is assumed to be spatially homogenous. As such, the stress of the SMP assumes the value of the stress in the pure rubbery or pure glassy phases when the glassy volume fraction equals 0 or 1, respectively. At temperatures when both the rubbery and glassy phases are present, the stress of the SMP is equal to both the rubbery and glassy stresses, which are equal due to the spatially constant stress assumption. Thus, through the above assumptions, the stress of the SMP

can be obtained through prescribing the constitutive equations for each the rubbery and the glassy phases.

Chapter III, as well as the previous efforts in [123], modeled the rubbery and glassy phases as incompressible neo-Hookean materials. Through the polar and spectral decompositions, the eigenvalues for the stress were reduced to functions for the eigenvalues of the stretch and the hydrostatic pressure required to maintain incompressibility (cf. Equation (19)). It has been documented [69, 70, 115], however, that polymers in the glassy phase are generally compressible in nature, with Poisson's ratios ranging from 0.33 to 0.46. Further, while the hydrostatic pressure in Equation (19) could be eliminated for particular boundary value problems, the implementation of the incompressible constitutive equations in a general finite element subroutine presents additional challenges that often require the use of hybrid elements or enforcement of incompressibility through a Lagrange multiplier penalty method [11].

Thus, in this chapter, compressible neo-Hookean constitutive equations are derived to address the glassy phase compressibility observations and the computational challenges associated with incompressibility. Equation (48) presents the Helmholtz free energy, as a function of the right Cauchy-Green deformation tensor $\mathbf{C}$ and the temperature θ, that is adopted in this work to for the compressible neo-Hookean response.

$$\Psi(\mathbf{C},\theta) = \frac{\mu}{2}\left(I_{\mathbf{C}} - 3 - 2\ln J\right) + \frac{\lambda}{4}\left(J^2 - 1 - 2\ln J\right)$$
$$-3\alpha\left(\theta - \theta_0\right)\left(\lambda + \frac{2}{3}\mu\right)\frac{\ln J}{J} \qquad (48)$$
$$+c_d\left(\theta\left(1 - \ln\frac{\theta}{\theta_0}\right) - \theta_0\right) + e_0 - \theta\eta_0$$

where the first line represents terms that are a function only of **C**, the second line captures the thermoelastic response and is a function of both **C** and θ, and the third line is a function of only the temperature and reference material properties. While the free energy previously presented in Equation (10) is formulated in terms of only the $I_{\mathbf{C}}$ (i.e., the first invariant of the right Cauchy-Green deformation tensor), the compressible free energy in this chapter also introduces *J*, which is the determinant of the deformation gradient $\left(J = \det \mathbf{F_e}\right)$ and is a function of the third invariant of **C** $\left(J = \sqrt{III_{\mathbf{C}}}\right)$. *J* physically represents the ratio of the current volume to that of the reference volume. This free energy has been previously adopted in describing the finite deformation response of shape memory alloys [121], and is assumed to be sufficient in this work for shape memory polymers undergoing moderate strains with relatively little nonlinearity in the stress-strain response. This assumption is supported by the experimental observations in Chapter II, in which the stress-strain curve for the thermosetting polyurethane SMP is approximately linear during elongation to failure.

The material properties in Equation (48) are the shear modulus μ, the Lamé coefficient λ, the coefficient of thermal expansion α, the heat capacity c_d, and the reference internal energy and entropy - e_0 and η_0, respectively. It is observed that the

term $\lambda + {}^{2\mu}\!/_{3}$ represents the bulk modulus K, which represents the change in the constitutive response due to volumetric changes. It is observed that, for incompressibility $(J=1)$ and in the absence of temperature effects, the free energy of Equation (48) reduces to the Helmholtz free energy of Chapter III (cf. Equation (10)). In addition, the Lamé coefficient can be expressed in terms of the shear modulus and the Poisson's ratio ν, as shown in Equation (49), where for an incompressible material $(\nu = 0.5)$, the Lamé coefficient (and consequently, the bulk modulus) would tend to infinity as the denominator tends to zero.

$$\lambda = \frac{2\mu\nu}{1-2\nu} \tag{49}$$

With the Helmholtz free energy defined, the second Piola-Kirchhoff stress and the Cauchy stress is derived through Equation (50) and Equation (51), respectively.

$$\mathbf{S} = 2\frac{\partial \Psi(\mathbf{C})}{\partial \mathbf{C}} \tag{50}$$

$$\boldsymbol{\sigma} = \frac{1}{J}\mathbf{F}\mathbf{S}\mathbf{F}^{\mathrm{T}} = \frac{2}{J}\mathbf{F}\frac{\partial \Psi(\mathbf{C})}{\partial \mathbf{C}}\mathbf{F}^{\mathrm{T}} \tag{51}$$

The partial derivative of the Helmholtz free energy in Equation (48) with respect to the right Cauchy-Green deformation tensor **C** is given in Equation (52).

$$\begin{aligned}\frac{\partial \Psi(\mathbf{C})}{\partial \mathbf{C}} = \mu\left(\frac{1}{2}\frac{\partial I_{\mathbf{C}}}{\partial \mathbf{C}} - \frac{\partial \ln J}{\partial \mathbf{C}}\right) + \frac{\lambda}{4}\left(\frac{\partial J^2}{\partial \mathbf{C}} - 2\frac{\partial \ln J}{\partial \mathbf{C}}\right) \\ -3\alpha\Delta\theta\left(\lambda + \frac{2\mu}{3}\right)\frac{\partial\left(\frac{\ln J}{J}\right)}{\partial \mathbf{C}}\end{aligned} \tag{52}$$

where the partial derivatives of the first and second invariants are given [124] by Equation (53).

$$\begin{aligned}\frac{\partial I_{\mathbf{C}}}{\partial \mathbf{C}} &= \mathbf{I} \\ \frac{\partial J}{\partial \mathbf{C}} &= \frac{J}{2}\mathbf{C}^{-1}\end{aligned} \tag{53}$$

Substituting the partial derivatives of Equation (52) and (53) into Equation (50) and performing simplifying operations, the resulting second Piola-Kirchhoff stress is presented in Equation (54).

$$\mathbf{S} = \mu\mathbf{I} + \left(\frac{\lambda}{2}J^2 - \frac{\lambda}{2} - \mu\right)\mathbf{C}^{-1} - 3\alpha\Delta\theta\left(\lambda + \frac{2\mu}{3}\right)\frac{1}{J}\left(1 - \ln J\right)\mathbf{C}^{-1} \tag{54}$$

where $\mathbf{C}^{-1} = \left(\mathbf{F}^{\mathrm{T}}\mathbf{F}\right)^{-1} = \mathbf{F}^{-1}\mathbf{F}^{-\mathrm{T}}$. Transforming Equation (54) via Equation (51) results in an expression for the Cauchy stress presented in Equation (55).

$$\boldsymbol{\sigma} = \frac{\mu}{J}\mathbf{F}^{\mathrm{T}}\mathbf{F} + \left(\frac{\lambda}{2}J - \frac{\lambda}{2J} - \frac{\mu}{J}\right)\mathbf{I} - 3\alpha\Delta\theta\left(\lambda + \frac{2\mu}{3}\right)\frac{1}{J^2}\left(1 - \ln J\right)\mathbf{I} \tag{55}$$

Through assuming each phase behaves as a compressible neo-Hookean material, an equation of the form in Equation (55) is defined for each the rubbery and glassy phases. These resulting constitutive equations are presented, in terms of the elastic deformation gradient for the rubbery and glassy phases, in Equations (56) and (57), respectively.

$$\boldsymbol{\sigma}^r = \frac{\mu^r}{J^r}\mathbf{F}_e^r\mathbf{F}_e^{r^{\mathrm{T}}} + \left(\frac{\lambda^r}{2}J^r - \frac{\lambda^r}{2J^r} - \frac{\mu^r}{J^r}\right)\mathbf{I}$$
$$-3\alpha^r\Delta\theta\left(\lambda^r + \frac{2\mu^r}{3}\right)\frac{1}{\left(J^r\right)^2}\left(1-\ln J^r\right)\mathbf{I} \tag{56}$$
$$J^r = \det\mathbf{F}_e^r$$

$$\boldsymbol{\sigma}^g = \frac{\mu^g}{J^g}\mathbf{F}_e^g\mathbf{F}_e^{g^{\mathrm{T}}} + \left(\frac{\lambda^g}{2}J^g - \frac{\lambda^g}{2J^g} - \frac{\mu^g}{J^g}\right)\mathbf{I}$$
$$-3\alpha^g\Delta\theta\left(\lambda^g + \frac{2\mu^g}{3}\right)\frac{1}{\left(J^g\right)^2}\left(1-\ln J^g\right)\mathbf{I} \tag{57}$$
$$J^g = \det\mathbf{F}_e^g$$

IV.C. Thermoelastic Coupling

In addition to the constitutive and kinematic equations, the balance of energy equations can be solved simultaneously for problems in which the displacements and the temperature are changing simultaneously. As a result, this section derives the equations that relate the change in temperature to the change in strain, the components of which are coded into the Abaqus user material subroutine for coupled temperature-displacement analyses. Recall that the Helmholtz free energy *per unit volume* for the compressible neo-Hookean material that is being considered in this work (cf. Equation (48)) is a function only of the right Cauchy-Green deformation tensor **C** and the temperature θ; thus, these thermomechanical coupling derivations are limited in scope to only thermoelastic coupling (i.e., no latent heat, etc.).

IV.C.1. First Law of Thermodynamics

The global form of the balance of energy (1st law of thermodynamics) in the spatial description is written as Equation (58) [121].

$$\frac{\mathrm{D}}{\mathrm{D}t}\int_{\Omega}\left(\frac{1}{2}\rho\mathbf{v}^2+e_c\right)dv=\int_{\partial\Omega}\left(\mathbf{t}\cdot\mathbf{v}+q_n\right)ds+\int_{\Omega}\left(\mathbf{b}\cdot\mathbf{v}+r\right)dv \tag{58}$$

where ρ is the mass density, $\mathbf{v}$ is the spatial velocity field, e_c is the internal energy *per unit volume*, $\mathbf{t}$ is the applied traction vector, q_n is the heat flux, $\mathbf{b}$ is the body force vector, and r is heat sink/source *per unit volume.* Equation (58) can then be written in a reduced global form as Equation (59).

$$\frac{\mathrm{D}}{\mathrm{D}t}\int_{\Omega}e_c dv=\int_{\Omega}\left(\boldsymbol{\sigma}\cdot\mathbf{D}-\mathrm{div}\mathbf{q}+r\right)dv \tag{59}$$

where $\mathbf{D}$ is the rate of deformation tensor. Equation (59) is rewritten as Equation (60) with the internal energy and heat sink/source expressed as quantities *per unit mass*.

$$\frac{\mathrm{D}}{\mathrm{D}t}\int_{\Omega}\rho u dv=\int_{\Omega}\left(\boldsymbol{\sigma}\cdot\mathbf{D}-\mathrm{div}\mathbf{q}+\rho\tilde{r}\right)dv \tag{60}$$

where u is the internal energy per unit mass and $\tilde{r}$ is the heat sink/source per unit mass. The total time derivative in Equation (60) is then reduced using Reynolds's Transport Theorem [121],which is presented in Equation (61).

$$\frac{\mathrm{D}}{\mathrm{D}t}\int_{\Omega}\rho(\mathbf{x},t)\Pi(\mathbf{x},t)dv=\int_{\Omega}\rho(\mathbf{x},t)\dot{\Pi}(\mathbf{x},t)dv \tag{61}$$

where Π is used to represent an arbitrary scalar function. Using Equation (61), Equation (60) is rewritten as Equation (62).

$$\int_{\Omega} \rho \dot{u} dv = \int_{\Omega} \left(\boldsymbol{\sigma} \cdot \mathbf{D} - \text{div}\mathbf{q} + \rho \tilde{r} \right) dv \tag{62}$$

Equation (62) is then written in the local form in Equation (63).

$$\rho \dot{u} = \boldsymbol{\sigma} \cdot \mathbf{D} - \text{div}\mathbf{q} + \rho \tilde{r} \tag{63}$$

The internal energy and its derivative with respect to time are then rewritten in Equations (64) and (65), respectively, using a Legendre transformation, in terms of the Helmholtz free energy Φ *per unit mass*, the entropy η *per unit mass*, and the temperature θ.

$$u = \Phi + \eta\theta \tag{64}$$

$$\dot{u} = \dot{\Phi} + \dot{\eta}\theta + \eta\dot{\theta} \tag{65}$$

The Helmholtz free energy per unit mass $\left(\Phi = \frac{1}{\rho} \Psi \right)$ is defined in Equation (66), where c is the heat capacity of the material per unit mass and u_0 and η_0 are the reference internal energy and entropy, respectively, per unit mass.

$$\begin{aligned} \Phi(\mathbf{C}, \theta) = & \frac{\mu}{2\rho}\left(I_{\mathbf{C}} - 3 - 2\ln J \right) + \frac{\lambda}{4\rho}\left(J^2 - 1 - 2\ln J \right) \\ & - \frac{3\alpha}{\rho}\left(\theta - \theta_0 \right)\left(\lambda + \frac{2}{3}\mu \right)\frac{\ln J}{J} \\ & + c\left(\theta\left(1 - \ln\frac{\theta}{\theta_0} \right) - \theta_0 \right) + u_0 - \theta\eta_0 \end{aligned} \tag{66}$$

Substituting Equation (65) into Equation (63) results in the local form of the 1st Law of Thermodynamics written in terms of the time derivative of the Helmholtz free energy in Equation (67). Note that the stress power term in the right hand side of

Equation (63) has also been rewritten in Equation (67) in terms of the second Piola-Kirchhoff stress $\mathbf{S}$ and the rate of the right Cauchy-Green deformation tensor $\mathbf{C}$.

$$\rho\dot{\Phi} + \rho\dot{\eta}\theta + \rho\eta\dot{\theta} = \frac{1}{2J}\mathbf{S}\cdot\dot{\mathbf{C}} - \mathrm{div}\mathbf{q} + \rho\tilde{r} \tag{67}$$

IV.C.2. Entropy Inequality Principle - Second Law of Thermodynamics

The second law of thermodynamics postulates that the total entropy production for all thermodynamic processes is non-negative. Applying this principle to continuum mechanics, Equation (68) presents the global form of the second law of thermodynamics in the spatial description.

$$\frac{\mathrm{D}}{\mathrm{D}t}\int_{\Omega}\eta_c dv + \int_{\partial\Omega}\mathbf{h}\cdot\mathbf{n}ds - \int_{\Omega}\frac{r}{\theta}dv \geq 0 \tag{68}$$

where η_c is the entropy in the spatial configuration per unit volume, $\mathbf{h}$ is the entropy flux, and r/θ is the entropy source. Rewriting the entropy and entropy source per unit mass, Equation (68) becomes Equation (69).

$$\frac{\mathrm{D}}{\mathrm{D}t}\int_{\Omega}\rho\eta dv + \int_{\partial\Omega}\mathbf{h}\cdot\mathbf{n}ds - \int_{\Omega}\frac{\rho\tilde{r}}{\theta}dv \geq 0 \tag{69}$$

Using Reynolds's Transport Theorem to simplify the time derivative in the first term, Equation (69) is reduced to Equation (70).

$$\int_{\Omega}\rho\dot{\eta}dv + \int_{\partial\Omega}\mathbf{h}\cdot\mathbf{n}ds - \int_{\Omega}\frac{\rho\tilde{r}}{\theta}dv \geq 0 \tag{70}$$

The divergence theorem is then introduced in Equation (71) to rewrite the second term of Equation (70), noting that the entropy vector $\mathbf{h}$ is related to the heat flux vector $\mathbf{q}$ through $\mathbf{h} = \mathbf{q}/\theta$.

$$\int_{\partial\Omega} \mathbf{h}\cdot\mathbf{n}ds = \int_{\Omega} \mathrm{div}\mathbf{h}dv = \int_{\Omega} \mathrm{div}\frac{\mathbf{q}}{\theta}dv = \int_{\Omega}\left(\frac{1}{\theta}\mathrm{div}\mathbf{q} - \frac{\mathbf{q}}{\theta^2}\cdot\nabla\theta\right)dv \tag{71}$$

Substituting Equation (71) into Equation (70), the entropy inequality principle is then rewritten as Equation (72).

$$\int_{\Omega}\rho\dot{\eta}dv + \int_{\Omega}\left(\frac{1}{\theta}\mathrm{div}\mathbf{q} - \frac{\mathbf{q}}{\theta^2}\cdot\nabla\theta\right)dv - \int_{\Omega}\frac{\rho\tilde{r}}{\theta}dv \geq 0 \tag{72}$$

Equation (72) is then written in the local form as Equation (73).

$$\rho\dot{\eta} + \frac{1}{\theta}\mathrm{div}\mathbf{q} - \frac{\mathbf{q}}{\theta^2}\cdot\nabla\theta - \frac{\rho\tilde{r}}{\theta} \geq 0 \tag{73}$$

Through the assumption of Fourier's Law and positive heat conductivity, the third term is realized to be always non-negative. Thus, Equation (73) is rewritten as Equation (74), which is often referred to as the strong form of the entropy inequality principle.

$$\rho\dot{\eta}\theta + \mathrm{div}\mathbf{q} - \rho\tilde{r} \geq 0 \tag{74}$$

IV.C.3. Combining the 1st and 2nd Laws

The first of thermodynamics, as written in Equation (67), is then substituted into the entropy inequality principle established in Equation (74) to result in Equation (75).

$$\frac{1}{2J}\mathbf{S}\cdot\dot{\mathbf{C}} - \rho\dot{\Phi} - \rho\eta\dot{\theta} \geq 0 \tag{75}$$

The time derivative of the Helmholtz free energy is then expanded using Equation (76), which is substituted into Equation (75), resulting in Equation (77).

$$\dot{\Phi} = \frac{\partial \Phi}{\partial \mathbf{C}} \dot{\mathbf{C}} + \frac{\partial \Phi}{\partial \theta} \dot{\theta} \tag{76}$$

$$\frac{1}{2J} \mathbf{S} \cdot \dot{\mathbf{C}} - \rho \left(\frac{\partial \Phi}{\partial \mathbf{C}} \dot{\mathbf{C}} + \frac{\partial \Phi}{\partial \theta} \dot{\theta} \right) - \rho \eta \dot{\theta} \geq 0 \tag{77}$$

Thus, grouping terms related to the time derivative of the right Cauchy-Green deformation tensor and the temperature in Equation (77) results in Equation (78).

$$\left(\frac{1}{2J} \mathbf{S} - \rho \frac{\partial \Phi}{\partial \mathbf{C}} \right) \dot{\mathbf{C}} - \rho \left(\frac{\partial \Phi}{\partial \theta} + \eta \right) \dot{\theta} \geq 0 \tag{78}$$

To consider all admissible processes, the inequality in Equation (78) is considered for processes in which either the deformation or the temperature is fixed. Considering first the case when the temperature is fixed, the second Piola-Kirchhoff stress is given through Equation (79).

$$\mathbf{S} = 2\rho J \frac{\partial \Phi}{\partial \mathbf{C}} \tag{79}$$

In addition, considering the case where there is no change in the deformation, the entropy per unit mass is given through Equation (80).

$$\eta = -\frac{\partial \Phi}{\partial \theta} \tag{80}$$

Further, the time derivative in Equation (76) are substituted into the local form of the first law in Equation (67), resulting in Equation (81).

$$\rho \frac{\partial \Phi}{\partial \mathbf{C}} \dot{\mathbf{C}} + \rho \frac{\partial \Phi}{\partial \theta} \dot{\theta} + \rho \dot{\eta} \theta + \rho \eta \dot{\theta} = \frac{1}{2J} \mathbf{S} \cdot \dot{\mathbf{C}} - \mathrm{div} \mathbf{q} + \rho \tilde{r} \tag{81}$$

The results in Equations (79) and (80) due to the enforcement of the entropy inequality principle are substituted into Equation (81), which is reduced to Equation (82)

.

$$\rho\dot{\eta}\theta = -\text{div}\mathbf{q} + \rho\tilde{r} \tag{82}$$

From Equation (80), the entropy is calculated as the partial derivative of the Helmholtz free energy with respect to mass and presented in Equation (83).

$$\eta = -\frac{\partial\Phi}{\partial\theta} = \frac{3\alpha}{\rho}\left(\lambda + \frac{2}{3}\mu\right)\frac{\ln J}{J} + c\ln\frac{\theta}{\theta_0} + \eta_0 \tag{83}$$

The time derivative of the entropy in Equation (82) is performed by taking the chain rule, as shown in Equation (84), and substituting the density by $\rho = \rho_0 / J$, where ρ_0 is the density in the reference configuration. Note that the time chain rule is expanded in terms of the logarithmic strain $\boldsymbol{\varepsilon} = \ln\mathbf{V} = \ln\sqrt{\mathbf{F}\mathbf{F}^{\mathrm{T}}}$ to provide a form that will facilitate implementation into the Abaqus user material subroutine.

$$\dot{\eta} = \frac{\partial\eta}{\partial\boldsymbol{\varepsilon}}\dot{\boldsymbol{\varepsilon}} + \frac{\partial\eta}{\partial\theta}\dot{\theta} = \frac{3\alpha}{\rho_0}\left(\lambda + \frac{2}{3}\mu\right)\frac{\partial\ln J}{\partial\boldsymbol{\varepsilon}}\dot{\boldsymbol{\varepsilon}} + \frac{c}{\theta}\dot{\theta} \tag{84}$$

where the partial derivative in the first term of Equation (84) is reduced by recognizing $\mathbf{V} = \exp\boldsymbol{\varepsilon}$ and that $J = \det\mathbf{V} = \det\left(\exp\left(\boldsymbol{\varepsilon}\right)\right)$. Using the identity [121] $\det\left(\exp\left(\mathbf{A}t\right)\right) = \exp\left(\left(\text{tr}\mathbf{A}\right)t\right)$ with $t = 1$ and $\mathbf{A} = \ln\mathbf{V}$, the first partial derivative shown on the right hand side of Equation (84) reduces to Equation (85).

$$\frac{\partial\ln J}{\partial\boldsymbol{\varepsilon}} = \mathbf{I} \tag{85}$$

Further, substituting Equation (85) into Equation (84) and using the identity that $\mathbf{I}\cdot\mathbf{A}=\mathrm{tr}(\mathbf{A})$ results in the final expression for the time derivative of the entropy in Equation (86).

$$\dot{\eta}=\frac{3\alpha}{\rho_0}\left(\lambda+\frac{2}{3}\mu\right)\mathrm{tr}\left(\dot{\boldsymbol{\varepsilon}}\right)+\frac{c}{\theta}\dot{\theta} \tag{86}$$

Substituting Equation (86) into Equation (82) provides an expression for the temperature balance, which is solved for in solving thermoelastic and/or heat transfer problems, in Equation (87).

$$\rho c\dot{\theta}=-\mathrm{div}\mathbf{q}-3\alpha\theta\left(\lambda+\frac{2}{3}\mu\right)\frac{1}{J}\mathrm{tr}\left(\dot{\boldsymbol{\varepsilon}}\right)+\rho\tilde{r} \tag{87}$$

Examining Equation (87), it is observed that the second term on the right hand side represents the thermoelastic coupling and is a function of the rate of straining, temperature, bulk modulus, and the volume ratio. This term is defined in Abaqus as r^{pl} – the volumetric heat generation per unit time at the end of the increment caused by mechanical working. Thus, this term and its derivatives with respect to the increments in both temperature and the logarithmic strain are presented in Equation (88) and subsequently coded in the user material subroutine. In Equation (88), the time derivative of the trace of the logarithmic strain tensor has been discretized using the Backward Euler method, where the superscripts (k) and $(k-1)$ represent the current and previous time increments, respectively.

$$
\begin{aligned}
r^{pl} &= -3\alpha\theta\left(\lambda+\frac{2}{3}\mu\right)\frac{1}{J}\left(\frac{\mathrm{tr}\boldsymbol{\varepsilon}^{(k)}-\mathrm{tr}\boldsymbol{\varepsilon}^{(k-1)}}{\Delta t}\right)\\
\frac{\partial r^{pl}}{\partial\theta} &= -3\alpha\left(\lambda+\frac{2}{3}\mu\right)\frac{1}{J}\left(\frac{\mathrm{tr}\boldsymbol{\varepsilon}^{(k)}-\mathrm{tr}\boldsymbol{\varepsilon}^{(k-1)}}{\Delta t}\right)\\
\frac{\partial r^{pl}}{\partial\varepsilon_{ij}} &= -\frac{1}{J\Delta t}3\alpha\theta\left(\lambda+\frac{2}{3}\mu\right)\left[1-\left(\mathrm{tr}\boldsymbol{\varepsilon}^{(k)}-\mathrm{tr}\boldsymbol{\varepsilon}^{(k-1)}\right)\right]\delta_{ij}
\end{aligned}
\tag{88}
$$

IV.D. Numerical Implementation

The previous sections (A and B) derived the set of equations that describe both the kinematics and constitutive response of the shape memory polymer. Specifically, Equations (43) and (44) present the equations for the average deformation gradient and average stretch, respectively, Equation (47) presents the new evolution equation for heating processes (in terms of known quantities), and Equations (56) and (57) present the constitutive equations for the rubbery and glassy phases, respectively. This section focuses on the numerical implementation of this set of equations, including the discretized and reduced equations and the procedures for solving the nonlinear system of equations in a user material subroutine (UMAT) in Abaqus - a displacement driven finite element code.

In a displacement driven finite element code, a guess to the displacement is provided and the resulting stress is calculated. After solving for the stress across the entire discretized structure (mesh), equilibrium is checked. If equilibrium is satisfied, then the program moves to the next increment; if not, new displacements are provided and the procedure is iterated until a solution is found. Thus, the UMAT for the shape

memory polymers must return, for a given displacement input, the stress and the fourth order Jacobian tensor. In solving the current system of equations (i.e. Equations (43)and (44), (56), and (57)), the deformation gradient **F** and temperature θ is provided as input from Abaqus and the solution procedure calculates the new stress $\boldsymbol{\sigma}$. In this work, the temperature is first used to calculate the value of the glassy volume fraction, which depends only on temperature. Dependent on the value of the glassy volume fraction, the procedure for solving the stress is then broken into three different cases: (i) the SMP is in the pure rubbery phase $\left(\phi(\theta)=0\right)$, (ii) the material is in the pure glassy phase $\left(\phi(\theta)=1\right)$, and (iii) the material is at a temperature such that it is a mixture of the rubbery and the glassy phases $\left(0<\phi(\theta)<1\right)$.

IV.D.1. Pure Rubbery Phase

The first case considered is that when the temperature is sufficiently high enough to result in the glassy volume fraction being equal to zero. In other words, the temperature is sufficiently high that the material is completely in the rubbery phase. In this scenario, the kinematic equation presented in Equation (43)[4] reduces to Equation

[4] Note that Equation (43) is used instead of Equation **Error! Reference source not found.**. Due to the constraint on the rotations described in Chapter III, either equation could be used equivalently. However, because the full deformation gradient is provided by Abaqus and it is not necessary to solve a system of equations, the full deformation gradient is subsequently used here to increase efficiency and to avoid potential numerical round-off errors when performing the polar decompositions.

(89)[5]. In this equation, the rubbery deformation gradient $\mathbf{F}_e^r$ is equal to the guess deformation gradient **F** that is provided as input in the current step. The stress of the material is then calculated as the stress of the rubbery phase through Equation (90).

$$\mathbf{F} = \mathbf{F}_e^r \tag{89}$$

$$\begin{aligned}\boldsymbol{\sigma} = \boldsymbol{\sigma}^r &= \frac{\mu^r}{J^r}\mathbf{F}_e^r\mathbf{F}_e^{r^{\mathrm{T}}} + \left(\frac{\lambda^r}{2}J^r - \frac{\lambda^r}{2J^r} - \frac{\mu^r}{J^r}\right)\mathbf{I} \\ &\quad - 3\alpha^r\Delta\theta\left(\lambda^r + \frac{2\mu^r}{3}\right)\frac{1}{\left(J^r\right)^2}\left(1-\ln J^r\right)\mathbf{I} \\ J^r &= \det\mathbf{F}_e^r\end{aligned} \tag{90}$$

IV.D.2. Pure Glassy Phase

The second phase considered is that in which the material has been cooled from the rubbery phase to a temperature in which the glassy volume fraction equals a value of one. In other words, the material is completely in the pure glassy phase with no change in the glassy volume fraction. In this scenario, the kinematic equation presented in Equation (43)[6] reduces to Equation (91).

$$\mathbf{F} = \mathbf{F}_e^g\int_0^t \tilde{\mathbf{F}}\left(\mathbf{P}(\tau),\theta(\tau)\right)\phi'\left(\theta(\tau)\right)\theta'(\tau)\,d\tau \tag{91}$$

---

[5] The dependency of $\mathbf{F}_e^r$ on **P** and θ has been suppressed for visual simplification. Unless noted otherwise, future instances of $\mathbf{F}_e^r$ and $\mathbf{F}_e^g$ without functional dependencies listed will be assumed to be functions of **P** and θ.

[6] Similar to the methodology for the pure rubbery phase, the full deformation gradient is used in the pure glassy scenario to improve computational efficiency and to avoid potential round-off errors in numerically performing the polar decomposition.

In Equation (92), the inverse of the glassy elastic deformation gradient is multiplied through on the left side of Equation (91).

$$\mathbf{F}_e^{g^{-1}}\mathbf{F} = \int_0^t \tilde{\mathbf{F}}\left(\mathbf{P}(\tau),\theta(\tau)\right)\phi'\left(\theta\left(\tau\right)\right)\theta'\left(\tau\right)d\tau \tag{92}$$

Further, Equation (93) presents the time derivative of Equation (92)

$$\dot{\overline{\mathbf{F}_e^{g^{-1}}\mathbf{F}}} = 0 \tag{93}$$

where the right hand side of the equation is equal to zero due to the fact that the integral term is a constant when cooling is complete and there is no current change in the glassy volume fraction. Equation (94) expands the time derivative on the left hand side of Equation (93).

$$\left(\dot{\mathbf{F}}_e^{g^{-1}}\right)\mathbf{F} + \mathbf{F}_e^{g^{-1}}\dot{\mathbf{F}} = 0 \tag{94}$$

Equation (94) is then discretized using a Backward Euler difference scheme, resulting in Equation (95).

$$\frac{\left(\mathbf{F}_e^{g^{-1}}\right)^{(k)} - \left(\mathbf{F}_e^{g^{-1}}\right)^{(k-1)}}{\Delta t}\mathbf{F}^{(k)} + \left(\mathbf{F}_e^{g^{-1}}\right)^{(k)}\frac{\mathbf{F}^{(k)} - \mathbf{F}^{(k-1)}}{\Delta t} = 0 \tag{95}$$

where the superscripts (k) and $(k-1)$ represent the values at the current and the previous time steps, respectively, and Δt is the time increment between the current and previous steps. Equation (95) is then simplified by eliminating the Δt in both terms and multiplying through on the left by the glassy elastic deformation gradient at the current time $\mathbf{F}_e^{g^{(k)}}$.

$$2\mathbf{F}^{(k)} - \mathbf{F}_e^{g^{(k)}} \left(\mathbf{F}_e^{g^{-1}} \right)^{(k-1)} \mathbf{F}^{(k)} - \mathbf{F}^{(k-1)} = 0 \tag{96}$$

Finally, Equation (96) is rearranged as Equation (97) to provide an explicit equation for the current glassy elastic deformation gradient in terms of input quantities ($\mathbf{F}_i$) and quantities known from previous increments.

$$\mathbf{F}_e^{g^{(k)}} = \left(2\mathbf{F}^{(k)} - \mathbf{F}^{(k-1)} \right) \mathbf{F}^{-1^{(k)}} \mathbf{F}_e^{g^{(k-1)}} \tag{97}$$

With the new glassy elastic deformation explicitly defined, the stress of the SMP is then calculated as the stress of the glassy phase through Equation (98).

$$\begin{aligned} \boldsymbol{\sigma} = \boldsymbol{\sigma}^g &= \frac{\mu^g}{J^g} \mathbf{F}_e^g \mathbf{F}_e^{g^{\mathrm{T}}} + \left(\frac{\lambda^g}{2} J^g - \frac{\lambda^g}{2J^g} - \frac{\mu^g}{J^g} \right) \mathbf{I} \\ &\quad - 3\alpha^g \Delta\theta \left(\lambda^g + \frac{2\mu^g}{3} \right) \frac{1}{\left(J^g \right)^2} \left(1 - \ln J^g \right) \mathbf{I} \\ J^g &= \det \mathbf{F}_e^g \end{aligned} \tag{98}$$

IV.D.3. Mixed Rubbery and Glassy Phases

The third consideration is when the temperature of the SMP is such that the glassy volume fraction is between 0 and 1. In other words, the temperature of the shape memory polymer is such that both the glassy and the rubbery phases are present. In this situation, the stress of the SMP is the unknown but is a dependent variable of the elastic deformation gradients for both the rubbery and the glassy phases. Thus, to calculate the new stress, the equation for the average stretch, Equation (44), and the constitutive equations in Equations (56) and (57) must be solved simultaneously to find the new

rubbery and glassy stretches while enforcing a spatially constant stress, as shown in Equation (99) .

$$\boldsymbol{\sigma} = \boldsymbol{\sigma}_r = \boldsymbol{\sigma}_g \tag{99}$$

In considering Equation (44), it is recalled that the average stretch of the SMP is expressed in terms of the stretch of the rubbery and glassy phases. In the finite element software, however, the total deformation gradient $\mathbf{F}$ is provided as input. As a result, the deformation gradient must then be decomposed into the rotational and stretch components. In this work, this decomposition is performed using the algorithm of [120], which is also detailed in Appendix A.

Using the kinematic assumption that the rotations in the rubbery and glassy phases are equal to the average rotation, the constitutive equations in Equations (56) and (57) are rewritten as Equations (100) and (101), where $\mathbf{F}_e^r$ and $\mathbf{F}_e^g$ have been expanded using the polar decompositions of Equation (6) with the rotations set equal to the rotation of the average deformation gradient as in Equation (7). Note that, writing Equations (100) and (101), the symmetry of $\mathbf{U}$ has been used $\left(\mathbf{U} = \mathbf{U}^{\mathrm{T}}\right)$ as well as the property that rigid body rotations do not result in volumetric changes such that $\det \mathbf{F} = \det \mathbf{R} \det \mathbf{U} = \det \mathbf{U}$.

$$\boldsymbol{\sigma}^r = \frac{\mu^r}{J^r}\mathbf{R}\mathbf{U}_e^r\mathbf{U}_e^r\mathbf{R}^{\mathrm{T}} + \left(\frac{\lambda^r}{2}J^r - \frac{\lambda^r}{2J^r} - \frac{\mu^r}{J^r}\right)\mathbf{I}$$
$$-3\alpha^r\Delta\theta\left(\lambda^r + \frac{2\mu^r}{3}\right)\frac{1}{\left(J^r\right)^2}\left(1-\ln J^r\right)\mathbf{I} \qquad (100)$$
$$J^r = \det\mathbf{U}_e^r$$

$$\boldsymbol{\sigma}^g = \frac{\mu^g}{J^r}\mathbf{R}\mathbf{U}_e^g\mathbf{U}_e^g\mathbf{R}^{\mathrm{T}} + \left(\frac{\lambda^g}{2}J^g - \frac{\lambda^g}{2J^g} - \frac{\mu^g}{J^g}\right)\mathbf{I}$$
$$-3\alpha^g\Delta\theta\left(\lambda^g + \frac{2\mu^g}{3}\right)\frac{1}{\left(J^g\right)^2}\left(1-\ln J^g\right)\mathbf{I} \qquad (101)$$
$$J^g = \det\mathbf{U}_e^g$$

IV.D.3.1. Newton-Raphson Method

In the previous section, the equations were derived for solving for the state of the SMP when provided a deformation gradient and temperature input from the finite element software. When the material is in the pure rubbery or pure glassy phases, the system of equations is solved in a straight-forward manner. Specifically, an explicit equation is used to calculate the new rubbery and glassy deformation gradients (cf. Equations (89) and (97)) as a function of the deformation gradient passed into the UMAT. These rubbery and glassy deformation gradients are then substituted into the respective constitutive equations (cf. Equations (90) and (98)), from which the stress is calculated and returned to the global finite element solver. However, in the temperature range in which the rubbery and glassy phases coexist, Equations (44), (100), and (101)

must be solved simultaneously while invoking the assumption that the stress is spatially constant as shown in Equation (99).

This section derives the equations, as reduced and discretized, that are necessary for the Newton-Raphson method that is invoked for solving the system of nonlinear equations. The Newton-Raphson method, which is described in more detail in [125], provides a solution to the matrix equation in Equation (102)

$$\left[J\right]\left\{\partial u\right\} = \left\{R\right\} \tag{102}$$

where J is the Jacobian matrix and consists of the partial derivatives of the nonlinear equations with respect to the unknowns, ∂u is the vector that contains increments to the unknowns, and R is the residual vector that is being minimized through an iterative solution procedure. In this problem, Equation (102) is consists of 12 equations that are solved simultaneously. Specifically, Equation (44) is solved in conjunction with the Equation (99) where U_{ij}^{r} and U_{ij}^{g} are the unknown quantities[7] when $\mathbf{U}$ and θ are provided as inputs. In solving for the converged values of the unknowns, the stress in the SMP is automatically obtained through the constraint in Equation (99).

Due to the introduction of the evolution equation for the stored deformation during heating in Equation (44), the resulting systems of kinematic equations differ for the cooling and heating processes. The derivations for both processes are presented in the following subsections.

---

[7] The subscript 'e' has been suppressed on $\mathbf{U}_e^r$ and $\mathbf{U}_e^g$ for conciseness for the remainder of this chapter, and it is assumed that stretches, rotations, or deformation gradients written with the superscripts 'r' or 'g' are referring to the elastic response of the material.

IV.D.3.1.1. Cooling Kinematics

First, the scenario in which the SMP is in the transformation temperature range and the temperature is being decreased is considered. Starting first with the kinematic expression for the average stretch in the SMP, the inverse of the glassy elastic deformation gradient is multiplied through Equation (44) on the left to result in Equation (103).

$$\mathbf{U}^{g^{-1}}\mathbf{U} = \left[1-\phi\left(\theta\right)\right]\mathbf{U}^{g^{-1}}\mathbf{U}^{r} + \int_{0}^{t}\mathbf{U}_{nat}\left(\mathbf{S}(\tau),\theta(\tau)\right)\phi'\left(\theta\left(\tau\right)\right)\theta'\left(\tau\right)d\tau \tag{103}$$

Subsequently, the time derivative of Equation (103) is performed, resulting in Equation (104). In performing the time derivative, the fundamental theorem of calculus is used on the integral term. Recalling that τ represents the most recent time the material was cooled through transformation, it is observed that τ is equivalent to the current time t and thus the integral can be expressed as a difference of the function evaluated at the integral limits.

$$\begin{aligned}\dot{\overline{\mathbf{U}^{g^{-1}}\mathbf{U}}} = {} & \dot{\overline{\left[1-\phi\left(\theta\right)\right]\mathbf{U}^{g^{-1}}\mathbf{U}^{r}}} \\ & +\mathbf{U}_{nat}\left(\mathbf{S}(t),\theta(t)\right)\phi'\left(\theta\left(t\right)\right)\theta'\left(t\right) \\ & -\mathbf{U}_{nat}\left(\mathbf{S}(0),\theta(0)\right)\phi'\left(\theta\left(0\right)\right)\theta'\left(0\right)\end{aligned} \tag{104}$$

Expanding the time derivatives in the first line of Equation (104) results in Equation (105).

$$\begin{aligned}\dot{\overline{\mathbf{U}^{g^{-1}}}}\,\mathbf{U}+\mathbf{U}^{g^{-1}}\dot{\mathbf{U}} &= -\dot{\phi}(\theta)\mathbf{U}^{g^{-1}}\mathbf{U}^{r} \\ &\quad +\left[1-\phi(\theta)\right]\dot{\overline{\mathbf{U}^{g^{-1}}}}\,\mathbf{U}^{r} \\ &\quad +\left[1-\phi(\theta)\right]\mathbf{U}^{g^{-1}}\dot{\mathbf{U}}^{r} \\ &\quad +\mathbf{U}_{nat}\left(\mathbf{S}(t),\theta(t)\right)\phi'\left(\theta(t)\right)\theta'(t) \\ &\quad -\mathbf{U}_{nat}\left(\mathbf{S}(0),\theta(0)\right)\phi'\left(\theta(0)\right)\theta'(0)\end{aligned} \tag{105}$$

Noting that the first and fourth terms on the right hand side are equal (cf. Equation (9)) cancel and the fifth term is equal to zero, Equation (105) reduces to Equation (106).

$$\dot{\overline{\mathbf{U}^{g^{-1}}}}\,\mathbf{U}+\mathbf{U}^{g^{-1}}\dot{\mathbf{U}} = \left[1-\phi(\theta)\right]\dot{\overline{\mathbf{U}^{g^{-1}}}}\,\mathbf{U}^{r}+\left[1-\phi(\theta)\right]\mathbf{U}^{g^{-1}}\dot{\mathbf{U}}^{r} \tag{106}$$

Discretizing Equation (106) using the Backward Euler method results in Equation (107), where the superscripts (k) and $(k-1)$ represent the current and previous increments, respectively, and the time increment Δt has been eliminated from the equation.

$$\begin{aligned}&\left[\mathbf{U}^{g^{-1}(k)}-\mathbf{U}^{g^{-1}(k-1)}\right]\mathbf{U}^{(k)}+\mathbf{U}^{g^{-1}(k)}\left[\mathbf{U}^{(k)}-\mathbf{U}^{(k-1)}\right] \\ &\quad =\left[1-\phi(\theta)\right]\left[\mathbf{U}^{g^{-1}(k)}-\mathbf{U}^{g^{-1}(k-1)}\right]\left(\mathbf{U}^{r}\right)^{(k)} \\ &\quad +\left[1-\phi(\theta)\right]\mathbf{U}^{g^{-1}(k)}\left[\mathbf{U}^{r^{(k)}}-\mathbf{U}^{r^{(k-1)}}\right]\end{aligned} \tag{107}$$

Multiplying Equation (107) by the glassy elastic stretch $\mathbf{U}^{g^{(k)}}$ on the left side and consolidating terms results in Equation (108).

$$2\mathbf{U}^{(k)} - \mathbf{U}^{(k-1)} = \left[1-\phi(\theta)\right]\left[2\mathbf{U}^{r^{(k)}} - \mathbf{U}^{r^{(k-1)}} - \mathbf{U}^{g^{(k)}}\mathbf{U}^{g^{-1^{(k-1)}}}\mathbf{U}^{r^{(k)}} \right] + \mathbf{U}^{g^{(k)}}\mathbf{U}^{g^{-1^{(k-1)}}}\mathbf{U}^{(k)} \tag{108}$$

Equation (109) then presents Equation (108) with all of the terms on one side, written in indicial notation, and set equal to R_{ij}. In other words, Equation (109) defines the residual equations for the six kinematic equations during the cooling process.

$$\begin{aligned} R_{ij} = &\left[1-\phi(\theta)\right]\left[2U_{ij}^{r^{(k)}} - U_{il}^{g^{(k)}}U_{lm}^{g^{-1^{(k-1)}}}U_{mj}^{r^{(k)}} \right] \\ &+U_{il}^{g^{(k)}}U_{lm}^{g^{-1^{(k-1)}}}U_{mj}^{(k)} \\ &-\left[1-\phi(\theta)\right]U_{ij}^{r^{(k-1)}} - 2U_{ij}^{(k)} + U_{ij}^{(k-1)} \end{aligned} \tag{109}$$

where the terms in the first line contain the unknowns in the rubbery and the glassy phases, the second line contains the unknown glassy stretches, and the third line consists of quantities that are all known either from previous increments or from input to the current step. In addition, by taking the partial derivatives of Equation (109) with respect to the unknowns U_{ij}^{r} and U_{ij}^{g}, Equations (110) and (111) present the contributions to the Jacobian matrix from the kinematic equations.

$$\begin{aligned} \frac{\partial R_{ij}}{\partial U_{st}^{r}} &= 2\left[1-\phi(\theta)\right]\delta_{is}\delta_{jt} - \left[1-\phi(\theta)\right]U_{il}^{g^{(k)}}U_{lm}^{g^{-1^{(k-1)}}}\delta_{ms}\delta_{jt} \\ &= 2\left[1-\phi(\theta)\right]\delta_{is}\delta_{jt} - \left[1-\phi(\theta)\right]U_{il}^{g^{(k)}}U_{ls}^{g^{-1^{(k-1)}}}\delta_{jt} \end{aligned} \tag{110}$$

$$\begin{aligned} \frac{\partial R_{ij}}{\partial U_{st}^{g}} &= -\left[1-\phi(\theta)\right]\delta_{is}\delta_{lt}U_{lm}^{g^{-1^{(k-1)}}}U_{mj}^{r^{(k)}} + \delta_{is}\delta_{lt}U_{lm}^{g^{-1^{(k-1)}}}U_{mj}^{(k)} \\ &= \delta_{is}U_{tm}^{g^{-1^{(k-1)}}}\left[U_{mj}^{(k)} - \left[1-\phi(\theta)\right]U_{mj}^{r^{(k)}} \right] \end{aligned} \tag{111}$$

where δ_{ij} is the Kronecker delta and represents the components of the second order identity tensor (i.e., $\delta_{ij}=1$ when $i=j$ and $\delta_{ij}=0$ when $i\neq j$).

In addition to solving for the updated values of $\mathbf{U}^r$ and $\mathbf{U}^g$, the stored deformation must also be calculated at each step. Multiplying the kinematics in Equation (44) through by the inverse of the glassy elastic stretch $\mathbf{U}^{g^{-1}}$ results in an explicit equation for the calculating the stored deformation, as presented in Equation (112).

$$\begin{aligned}\mathbf{U}^{stor} &= \int_0^t \mathbf{U}_{nat}\left(\mathbf{S}(\tau),\theta(\tau)\right)\phi'\left(\theta(\tau)\right)\theta'(\tau)\,d\tau \\ &= \mathbf{U}^{g^{-1}}\mathbf{U}-\left[1-\phi(\theta)\right]\mathbf{U}^{g^{-1}}\mathbf{U}^r\end{aligned} \tag{112}$$

IV.D.3.1.2. Heating Kinematics

The previous section derived the discretized equations for the kinematics when the SMP is being cooled. This section focuses on the equations for the kinematics when the SMP is being heated or for isothermal processes when the SMP is in the transformation temperature range. In both cases (i.e., heating or isothermal), there is no added stored deformation to the integral term of Equation (44). As such, Equation (44) and Equation (46) are combined and rewritten as Equation (113).

$$\mathbf{U}=\left[1-\phi(\theta)\right]\mathbf{U}^r+\mathbf{U}^g\mathbf{U}^{stor} \tag{113}$$

where $\mathbf{U}^{stor}$ is the stored deformation that is defined through Equation (114), which is the result of integrating Equation (47), and $\mathbf{U}_{rev}^{stor}$ is the stored deformation at the last time the material was cooled, calculated during the cooling step using Equation (112).

$$\mathbf{U}^{stor} = \frac{\mathbf{U}_{rev}^{stor}}{\phi_{rev}} \phi(\theta) \tag{114}$$

Writing Equation (113) in incremental and indicial form results in Equation (115) , where (k) represents the current increment.

$$U_{ij}^{(k)} = \left[1 - \phi^{(k)}(\theta)\right] U_{ij}^{r^{(k)}} + U_{il}^{g^{(k)}} \frac{\left(U_{rev}^{stor}\right)_{lj}^{(k)}}{\phi_{rev}} \phi^{(k)}(\theta) \tag{115}$$

Rewriting Equation (115) as Equation (116) by moving all terms to one side and setting it equation to R_{ij} defines the residual to be used in the Newton-Raphson matrix equation (cf. Equation (102)).

$$R_{ij} = \left[1 - \phi^{(k)}(\theta)\right] U_{ij}^{r^{(k)}} + U_{il}^{g^{(k)}} \frac{\left(U_{rev}^{stor}\right)_{lj}^{(k)}}{\phi_{rev}} \phi^{(k)}(\theta) - U_{ij}^{(k)} \tag{116}$$

where the first term on the right hand side only contains the rubbery unknowns and the second term contains only the glassy unknowns. Taking the partial derivative of Equation (116) with respect to the unknowns results in Equations (117) and (118), which define the terms that contribute to the Jacobian in Equation (102).

$$\frac{\partial R_{ij}}{\partial U_{st}^{r}} = \left[1 - \phi^{(k)}(\theta)\right] \delta_{is} \delta_{jt} \tag{117}$$

$$\frac{\partial R_{ij}}{\partial U_{st}^{g}} = \delta_{is}\delta_{lt}\frac{\left(U_{rev}^{stor}\right)_{lj}^{(k)}}{\phi_{rev}}\phi^{(k)}\left(\theta\right) = \delta_{is}\frac{\left(U_{rev}^{stor}\right)_{tj}^{(k)}}{\phi_{rev}}\phi^{(k)}\left(\theta\right) \tag{118}$$

IV.D.3.1.3. Constitutive Equations

In addition to the kinematic equations, the constitutive equations must be considered and discretized for use in the Newton-Raphson method. Begin first with the constitutive equations presented in Equations (100) and (101) for the rubbery and glassy phases, respectively. Substituting these equations into the constraint on the stresses in Equation (99) results in Equation (119).

$$\begin{aligned}\mathbf{0} = {} & \frac{\mu^{r}}{J^{r}}\mathbf{R}\mathbf{U}^{r}\mathbf{U}^{r}\mathbf{R}^{\mathrm{T}} + \left(\frac{\lambda^{r}}{2}J^{r} - \frac{\lambda^{r}}{2J^{r}} - \frac{\mu^{r}}{J^{r}}\right)\mathbf{I} \\ & -3\alpha^{r}\Delta\theta\left(\lambda^{r} + \frac{2\mu^{r}}{3}\right)\frac{1}{\left(J^{r}\right)^{2}}\left(1-\ln J^{r}\right)\mathbf{I} \\ & -\frac{\mu^{g}}{J^{r}}\mathbf{R}\mathbf{U}^{g}\mathbf{U}^{g}\mathbf{R}^{\mathrm{T}} + \left(\frac{\lambda^{g}}{2}J^{g} - \frac{\lambda^{g}}{2J^{g}} - \frac{\mu^{g}}{J^{g}}\right)\mathbf{I} \\ & +3\alpha^{g}\Delta\theta\left(\lambda^{g} + \frac{2\mu^{g}}{3}\right)\frac{1}{\left(J^{g}\right)^{2}}\left(1-\ln J^{g}\right)\mathbf{I}\end{aligned} \tag{119}$$

To eliminate the rotational components of Equation (119), the transpose of the rotation is multiplied through on the left and the rotation is multiplied through on the right. Using the identity that $\mathbf{R}^{\mathrm{T}}\mathbf{R} = \mathbf{R}\mathbf{R}^{\mathrm{T}} = \mathbf{I}$, Equation (119) is equivalently rewritten, in indicial notation as Equation (120), which effectively defines the components to the

residual vector for use in the Newton-Raphson method (for $i, j = (1,1),(1,2),(1,3),(2,2),(2,3),(3,3)$ with considering the symmetry of $\mathbf{U}$).

$$\begin{aligned} R_{ij} = 0_{ij} = & \frac{\mu^r}{J^r} U^r_{ik} U^r_{kj} + \left(\frac{\lambda^r}{2} J^r - \frac{\lambda^r}{2J^r} - \frac{\mu^r}{J^r} \right) \delta_{ij} \\ & -3\alpha^r \Delta\theta \left(\lambda^r + \frac{2\mu^r}{3} \right) \frac{1}{\left(J^r \right)^2} \left(1 - \ln J^r \right) \delta_{ij} \\ & - \frac{\mu^g}{J^r} U^g_{ik} U^g_{kj} + \left(\frac{\lambda^g}{2} J^g - \frac{\lambda^g}{2J^g} - \frac{\mu^g}{J^g} \right) \delta_{ij} \\ & +3\alpha^g \Delta\theta \left(\lambda^g + \frac{2\mu^g}{3} \right) \frac{1}{\left(J^g \right)^2} \left(1 - \ln J^g \right) \delta_{ij} \end{aligned} \tag{120}$$

Taking the partial derivative of Equation (120) with respect to the unknowns results in the contributions to the Newton-Raphson Jacobian matrix. Using the identities $\partial U_{ij} \big/ \partial U_{st} = \delta_{is}\delta_{jt}$ and $\partial J \big/ \partial U_{st} = J \left[U^{-1} \right]_{st}$, the partial derivatives with respect to the rubbery and glassy phases are presented in Equations (121) and (122), respectively.

$$\begin{aligned} \frac{\partial R_{ij}}{\partial U^r_{st}} = & -\frac{\mu^r}{J^r} \left[U^{r^{-\mathrm{T}}} \right]_{st} U^r_{ik} U^r_{kj} \\ & + \frac{\mu^r}{J^r} \left(\delta_{is} U^r_{tj} + U^r_{is} \delta_{jt} \right) \\ & + \left(\frac{\lambda^r}{2} J^r + \frac{\lambda^r}{2J^r} + \frac{\mu^r}{J^r} \right) \left[U^{r^{-\mathrm{T}}} \right]_{st} \delta_{ij} \\ & +3\alpha^r \Delta\theta \left(\lambda^r + \frac{2\mu^r}{3} \right) \frac{1}{\left(J^r \right)^2} \left(3 - 2\ln J^r \right) \left[U^{r^{-\mathrm{T}}} \right]_{st} \delta_{ij} \end{aligned} \tag{121}$$

$$\frac{\partial R_{ij}}{\partial U^{g}_{st}} = \frac{\mu^{g}}{J^{g}}\left[U^{g^{-\mathrm{T}}}\right]_{st} U^{g}_{ik}U^{g}_{kj}$$
$$-\frac{\mu^{g}}{J^{g}}\left(\delta_{is}U^{g}_{tj} + U^{g}_{is}\delta_{jt}\right)$$
$$-\left(\frac{\lambda^{g}}{2}J^{g} + \frac{\lambda^{g}}{2J^{g}} + \frac{\mu^{g}}{J^{g}}\right)\left[U^{g^{-\mathrm{T}}}\right]_{st}\delta_{ij} \qquad (122)$$
$$-3\alpha^{g}\Delta\theta\left(\lambda^{g} + \frac{2\mu^{g}}{3}\right)\frac{1}{\left(J^{g}\right)^{2}}\left(3 - 2\ln J^{g}\right)\left[U^{g^{-\mathrm{T}}}\right]_{st}\delta_{ij}$$

IV.D.3.1.4. Line-Search Method

In solving the Newton-Raphson method, initial guesses must be provided for the unknowns in the first increment in the iterative procedure. It is recalled that the procedure used in this work is to calculate the material is a pure rubbery material at high temperatures, a pure glassy material at low temperatures, and a mixed material at intermediate temperatures. In the rubbery phase, for example, the input deformation is used to determine the new value of the rubbery deformation gradient and there is no consideration of the glassy phase deformation gradient. Thus, special consideration must be taken when transitioning from a single phase material to a mixed phase material. In other words, proper guesses for both phases of the material must be provided to facilitate the convergence of the local Newton-Raphson method. In this work, the initial guess for the newly created phase is taken to be the rotation of the previous phase. That is, in the first step transitioning from the rubbery phase to the glassy phase, the initial guess for the deformation gradient of the glassy phase is set equal to the rotation of the rubbery phase. This assumption maintains consistency with previous assumptions that

the rotations of the two phases remain equal without specifying the magnitude of the stretch in the initial guess.

For cases where large deformations and/or complex thermomechanical load paths are present, the convergence capability of the Newton-Raphson method is improved by the addition of the line search method. This method, described in more detail in [122], allows for accepting a fraction of the increment that results from solving the Newton-Raphson system of equations until a converged solution is obtained. For the traditional Newton-Raphson method, the system of equations in Equation (102) is solved for the increment to the unknowns vector $\partial\mathbf{u}$, which is then used to modify the unknowns vector through Equation (123).

$$\mathbf{u}_{new} = \mathbf{u}_{old} + \partial\mathbf{u} \tag{123}$$

In the line searching method, however, Equation (123) is modified to Equation (124) through the introduction of a backtracking parameter ξ.

$$\mathbf{u}_{new} = \mathbf{u}_{old} + \xi\partial\mathbf{u} \qquad 0<\xi\leq 1 \tag{124}$$

Thus, in this method, the system of equations is solved using the standard Newton-Raphson method and $\partial\mathbf{u}$ is obtained. The backtrack parameter is set $\xi = 1$ such that the full increment is used in the next guess, as in the standard method. Using this guess, the norm of the residual vector (i.e. $f = \frac{1}{2}\mathbf{R}\cdot\mathbf{R}$) is checked, through Equation (125), to see if it has decreased sufficiently when compared to the initial rate of decrease.

$$f(\mathbf{u}_{new}) \leq f(\mathbf{u}_{old}) + \alpha\nabla f\cdot(\mathbf{u}_{new} - \mathbf{u}_{old}) \tag{125}$$

where α is a small parameter (10^{-4} is used in this work, as recommended by [122]) used as comparison against the initial rate of decrease. If the criteria in Equation (125) is met, the initial result from the Newton-Raphson method is used. If not, the backtrack parameter is modified in the second step through Equation (126).

$$\xi = -\frac{g'(0)}{2\left[g(1) - g(0) - g'(0)\right]} \tag{126}$$

where g is defined in Equation (127) as the norm of the residual when the increment is added to the previous unknown vector.

$$g(\xi) \equiv f\left(\mathbf{u}_{old} + \xi \partial \mathbf{u}\right) \tag{127}$$

In the third and subsequent iterations, g is expanded as a cubic function of ξ as in Equation (128). Requiring Equation (128) to produce the values of g at the previous two iterations and solving the resulting system equations for a and b, the backtrack parameter in the new iteration is determined through Equation (129).

$$g(\xi) = a\xi^3 + b\xi^2 + g'(0)\xi + g(0) \tag{128}$$

$$\xi = \frac{-b + \sqrt{b^2 - 3ag'(0)}}{3a} \tag{129}$$

IV.D.4. Continuum Tangent Modulus

In addition to providing the updated stress for a given deformation gradient and temperature, the UMAT is required to provide the local continuum tangent modulus. This fourth-order tensor, denoted in this work by $\mathbb{C}$ and often termed the Jacobian or elasticity tensor of the material, provides the relationship for the change in the stress

array given an infinitesimal perturbation of the strain increment array [122]. This elasticity tensor is then defined for total-form constitutive equations[8] through Equation (130), which expresses the variational form for the Jaumann rate of the Kirchhoff stress with respect to the variations (δ) in the deformation.

$$\delta\left(J\boldsymbol{\sigma}\right)=\delta\left(\boldsymbol{\tau}\right)=J\left(\mathbb{C}:\delta\mathbf{D}+\delta\mathbf{W}\cdot\boldsymbol{\sigma}-\boldsymbol{\sigma}\cdot\delta\mathbf{W}\right) \tag{130}$$

where $J\boldsymbol{\sigma}=\boldsymbol{\tau}$, the Kirchhoff stress, $\delta\mathbf{D}$ is the variation in the virtual rate of deformation tensor, and $\delta\mathbf{W}$ is the variation in the virtual spin tensor. $\mathbf{D}$ and $\mathbf{W}$ represent the symmetric and anti-symmetric components of the rate of deformation whose variations are related to the variation in the deformation gradient $\delta\mathbf{F}$ through Equations (131) and (132).

$$\delta\mathbf{D}=\mathrm{sym}\left(\delta\mathbf{F}\cdot\mathbf{F}^{-1}\right) \tag{131}$$

$$\delta\mathbf{W}=\mathrm{asym}\left(\delta\mathbf{F}\cdot\mathbf{F}^{-1}\right) \tag{132}$$

To define the elasticity tensor in Equation (130), it is first noted that the Lie derivative of the Kirchhoff stress $\left(L_v\boldsymbol{\tau}\right)$ can be written in spatial rate-constitutive form in Equation (133) or in terms of the Jaumann rate $\overset{\nabla}{\boldsymbol{\tau}}$ of the Kirchhoff stress in Equation (134) [126].

$$L_v\boldsymbol{\tau}=\underset{\approx}{\mathbf{c}}:\mathbf{D} \tag{133}$$

[8] For constitutive equations written in a rate-form, such as in plasticity, the exact constitutive Jacobian is expressed by $\mathbb{C}=\frac{1}{J}\frac{\partial\Delta\left(J\boldsymbol{\sigma}\right)}{\partial\Delta\boldsymbol{\varepsilon}}$.

$$L_v\boldsymbol{\tau} = \overset{\nabla}{\boldsymbol{\tau}} - \mathbf{D}\boldsymbol{\tau} - \boldsymbol{\tau}\mathbf{D} \tag{134}$$

where $\underset{\approx}{\mathbf{c}}$ is the fourth-order spatial (co-rotational) elasticity tensor and the Jaumann rate is an objective rate in terms of the spin tensor defined by Equation (135).

$$\overset{\nabla}{\boldsymbol{\tau}} = \dot{\boldsymbol{\tau}} - \mathbf{W}\boldsymbol{\tau} + \boldsymbol{\tau}\mathbf{W} \tag{135}$$

Combining Equations (133) and (134) results in Equation (136)., which is subsequently rewritten in constitutive form as Equation (137).

$$\underset{\approx}{\mathbf{c}} : \mathbf{D} = \overset{\nabla}{\boldsymbol{\tau}} - \mathbf{D}\boldsymbol{\tau} - \boldsymbol{\tau}\mathbf{D} \tag{136}$$

$$\overset{\nabla}{\boldsymbol{\tau}} = \underset{\approx}{\mathbf{a}} : \mathbf{D} \tag{137}$$

where $\underset{\approx}{\mathbf{a}}$ is the fourth-order modulus whose components are defined by Equation (138).

$$a_{ijkl} = c_{ijkl} + \delta_{ik}\tau_{jl} + \delta_{jl}\tau_{ik} \tag{138}$$

Combining Equations (135) and (137) results in an expression for the time derivative of the Kirchhoff stress in Equation (139).

$$\dot{\boldsymbol{\tau}} = \underset{\approx}{\mathbf{a}} : \mathbf{D} + \mathbf{W}\boldsymbol{\tau} - \boldsymbol{\tau}\mathbf{W} \tag{139}$$

Comparing Equation (130) to Equation (139), the desired Jacobian can be written in terms of $\underset{\approx}{\mathbf{a}}$ as shown in Equation (140).

$$\mathbb{C} = \frac{1}{J}\underset{\approx}{\mathbf{a}} \tag{140}$$

Thus, Equation (140) indicates the Jacobian required by Abaqus can be determined by determining the value of the determinant of the deformation gradient J

and the fourth order modulus tensor $\underset{\approx}{\mathbf{a}}$, which is a function of the spatial elasticity tensor $\underset{\approx}{\mathbf{c}}$. The components of the spatial elasticity tensor can be expressed through Equation (141) as a function of the components of the deformation gradient and the material elasticity tensor [125].

$$c_{ijkl} = F_{iI} F_{jJ} F_{kK} F_{lL} C^{mat}_{IJKL} \tag{141}$$

The material elasticity tensor is then a result of taking the second partial derivative of the Helmholtz free energy with respect to the right Cauchy-Green deformation tensor in Equation (142), which is also rewritten in terms of the second Piola-Kirchhoff stress.

$$\underset{\approx}{\mathbf{C}}^{mat} = 4\frac{\partial^2 \Psi}{\partial \mathbf{C} \partial \mathbf{C}} = 2\frac{\partial \mathbf{S}}{\partial \mathbf{C}} \tag{142}$$

Thus, Equations (140), (138), (141), and (142) provide the necessary equations for determining the Jacobian of a material with a known Helmholtz free energy. It is noted, however, that no single Helmholtz free energy in this work for the shape memory polymer that is assumed to be a mixture of the rubbery and glassy phases with a spatially constant stress. As a result, it is assumed that the Jacobian can be approximated by a rule of mixtures between the Jacobian for a pure rubbery material and the Jacobian for a pure glassy material as shown in Equation (143).

$$\mathbb{C} = \left[1 - \phi(\theta)\right]\mathbb{C}^r + \phi(\theta)\mathbb{C}^g \tag{143}$$

IV.D.4.1. Single Phase Neo-Hookean Spatial Elasticity Tensor

With the assumption of Equation (143), the Jacobians for the single phase neo-Hookean materials (rubbery and glassy) need to be determined. Due to the fact that this work assumes the same form of the Helmholtz free energy for each phase (with different material properties), the derivations will be presented in terms of a more general material (i.e. the superscripts 'r' and 'g' will be omitted). First, recall the Helmholtz free energy and second Piola-Kirchhoff stress (cf. Equations (48) and (54)), which are presented again in Equations (144) and (145).

$$\begin{aligned}\Psi(\mathbf{C},\theta) = {} & \frac{\mu}{2}\left(I_{\mathbf{C}} - 3 - 2\ln J\right) + \frac{\lambda}{4}\left(J^2 - 1 - 2\ln J\right) \\ & -3\alpha\left(\theta-\theta_0\right)\left(\lambda + \frac{2}{3}\mu\right)\frac{\ln J}{J} \\ & +c_d\left(\theta\left(1-\ln\frac{\theta}{\theta_0}\right)-\theta_0\right)+e_0-\theta\eta_0\end{aligned} \tag{144}$$

$$\mathbf{S} = \mu\mathbf{I} + \left(\frac{\lambda}{2}J^2 - \frac{\lambda}{2} - \mu\right)\mathbf{C}^{-1} - 3\alpha\Delta\theta\left(\lambda + \frac{2\mu}{3}\right)\frac{1}{J}\left(1-\ln J\right)\mathbf{C}^{-1} \tag{145}$$

Written in indicial notation, the second Piola-Kirchhoff stress is given by Equation (146), and the derivative with respect to the right Cauchy-Green deformation tensor is given by Equation (147).

$$\begin{aligned}S_{ij} = {} & \mu\delta_{ij} + \left(\frac{\lambda}{2}J^2 - \frac{\lambda}{2} - \mu\right)\left[C^{-1}\right]_{ij} \\ & -3\alpha\Delta\theta\left(\lambda + \frac{2\mu}{3}\right)\frac{1}{J}\left(1-\ln J\right)\left[C^{-1}\right]_{ij}\end{aligned} \tag{146}$$

$$\frac{\partial S_{ij}}{\partial C_{kl}} = \mu \frac{\delta_{ij}}{\partial C_{kl}} + \frac{\lambda}{2}\frac{\partial J^2}{\partial C_{kl}}\left[C^{-1}\right]_{ij} + \left[\frac{\lambda}{2}J^2 - \frac{\lambda}{2} - \mu - 3\alpha\Delta\theta\left(\lambda + \frac{2\mu}{3}\right)\frac{1}{J}\left(1-\ln J\right)\right]\frac{\partial\left[C^{-1}\right]_{ij}}{\partial C_{kl}} - 3\alpha\Delta\theta\left(\lambda + \frac{2\mu}{3}\right)\left[\frac{\partial\left(1/J\right)}{\partial C_{kl}}\left(1-\ln J\right) - \frac{1}{J}\frac{\partial \ln J}{\partial C_{kl}}\right]\left[C^{-1}\right]_{ij} \tag{147}$$

Using the partial derivatives of Equations (147) and (148), the material elasticity tensor is then presented through Equation (149).

$$\frac{\partial\left[C^{-1}\right]_{ij}}{\partial C_{kl}} = -\left[C^{-1}\right]_{ik}\left[C^{-1}\right]_{lj} \tag{148}$$

$$C^{mat}_{IJKL} = 2\frac{\partial S_{IJ}}{\partial C_{KL}} = \left[\lambda J^2 + 3\alpha\Delta\theta\left(\lambda + \frac{2\mu}{3}\right)\left(\frac{1}{J}\right)\left(2-\ln J\right)\right]\left[C^{-1}\right]_{KL}\left[C^{-1}\right]_{IJ} - \left[\lambda J^2 - \lambda - 2\mu - 6\alpha\Delta\theta\left(\lambda + \frac{2\mu}{3}\right)\frac{1}{J}\left(1-\ln J\right)\right]\left[C^{-1}\right]_{IK}\left[C^{-1}\right]_{LJ} \tag{149}$$

Using the symmetry of the material elasticity tensor (i.e. $C^{mat}_{IJKL} = C^{mat}_{IJLK}$), the second term is rewritten in Equation (150).

$$C^{mat}_{IJKL} = \left[\lambda J^2 + 3\alpha\Delta\theta\left(\lambda + \frac{2\mu}{3}\right)\left(\frac{1}{J}\right)\left(2-\ln J\right)\right]\left[C^{-1}\right]_{KL}\left[C^{-1}\right]_{IJ} - \left[\lambda J^2 - \lambda - 2\mu - 6\alpha\Delta\theta\left(\lambda + \frac{2\mu}{3}\right)\frac{1}{J}\left(1-\ln J\right)\right] \bullet \frac{1}{2}\left\{\left[C^{-1}\right]_{IK}\left[C^{-1}\right]_{LJ} + \left[C^{-1}\right]_{IL}\left[C^{-1}\right]_{KJ}\right\} \tag{150}$$

Expressing the components of the inverse of the right Cauchy-Green deformation tensor in terms of the deformation gradient through Equation (151), the multiplied tensors in Equation (150) can be rewritten as Equation (152).

$$\left[C^{-1}\right]_{IJ} = \left[F^{-1}\right]_{Ix}\left[F^{-1}\right]_{Jx} \tag{151}$$

$$\begin{aligned}
\left[C^{-1}\right]_{IJ}\left[C^{-1}\right]_{KL} &= \left[F^{-1}\right]_{Ii}\left[F^{-1}\right]_{Jx}\left[F^{-1}\right]_{Kj}\left[F^{-1}\right]_{Ly}\delta_{ix}\delta_{jy} \\
\left[C^{-1}\right]_{IK}\left[C^{-1}\right]_{LJ} &= \left[F^{-1}\right]_{Ii}\left[F^{-1}\right]_{Kx}\left[F^{-1}\right]_{Lj}\left[F^{-1}\right]_{Jy}\delta_{ix}\delta_{jy} \\
\left[C^{-1}\right]_{IL}\left[C^{-1}\right]_{KJ} &= \left[F^{-1}\right]_{Ii}\left[F^{-1}\right]_{Lx}\left[F^{-1}\right]_{Kj}\left[F^{-1}\right]_{Jy}\delta_{ix}\delta_{jy}
\end{aligned} \tag{152}$$

Thus, substituting Equation (152) into Equation (150), which is then substituted into Equation (141), the resulting spatial elasticity tensor is given in Equation (153).

$$\begin{aligned}
c_{ijkl} = &\left[\lambda J^2 + 3\alpha\Delta\theta\left(\lambda + \frac{2\mu}{3}\right)\left(\frac{1}{J}\right)\left(2 - \ln J\right)\right] \\
&+\left[\mu + \frac{\lambda}{2} - \frac{\lambda J^2}{2} + 3\alpha\Delta\theta\left(\lambda + \frac{2\mu}{3}\right)\frac{1}{J}\left(1 - \ln J\right)\right]\left(\delta_{ik}\delta_{jl} + \delta_{il}\delta_{kj}\right)
\end{aligned} \tag{153}$$

which can also be written in tensorial form, as shown in Equation (154).

$$\begin{aligned}
\underset{\approx}{\mathbf{c}} = &\left[\lambda J^2 + 3\alpha\Delta\theta\left(\lambda + \frac{2\mu}{3}\right)\left(\frac{1}{J}\right)\left(2 - \ln J\right)\right]\mathbf{I}\otimes\mathbf{I} \\
&+\left[2\mu + \lambda - \lambda J^2 + 6\alpha\Delta\theta\left(\lambda + \frac{2\mu}{3}\right)\frac{1}{J}\left(1 - \ln J\right)\right]\underset{\approx}{\mathbf{I}}
\end{aligned} \tag{154}$$

where $\mathbf{I}$ is used to denote the second order identity tensor, and $\underset{\approx}{\mathbf{I}}$ is the fourth order symmetric identity tensor. Note that, for an undeformed material $\left(\mathbf{F} = 1, J = 1\right)$, the spatial elasticity tensor reduces to that of a linear elastic material $\underset{\approx}{\mathbf{c}} = \lambda\mathbf{I}\otimes\mathbf{I} + 2\mu\underset{\approx}{\mathbf{I}}$.

Thus, by calculating the spatial elasticity tensor of the form in Equations (153) or (154) and the Kirchhoff stress for each the rubbery and glassy phases, the Jacobians for each phase are calculated through Equations (138) and (140). These Jacobians are then substituted into Equation (143) to find the Jacobian for the material, as a mixture of the rubbery and glassy phases.

IV.E. Calibration of Material Properties and Uniaxial Model Predictions

The kinematic equations and compressible constitutive equations in Equations (44), (100), (101), and (99) form the system of equations that must be solved to predict the behavior of the shape memory polymer system. Due to the assumption of isotropic material behavior in the rubbery and glassy phases, it is necessary to quantify seven calibration parameters, $\mu^r, \mu^g, \lambda^r, \lambda^g, \alpha^r, \alpha^g, \phi(\theta)$, which respectively represent the shear moduli in the rubbery and glassy phases, the Lamé coefficients in the rubbery and glassy phases, the coefficients of thermal expansion in the rubbery and glassy phases, and the glassy volume fraction as a function of temperature.

Similar to the 1D modeling in Chapter III, the 10% extension free recovery experiment is used to calibrate the shear moduli and the glassy volume fraction. Specifically, the rubbery and glassy tensile moduli are calibrated to the isothermal loading and unloading procedures at 90°C and 25°C, respectively. The shear moduli and Lamé coefficients are then calculated using Equations (24) and (49), respectively. The rubbery Poisson ratio is assumed to be 0.499 to capture the assumed nearly incompressible behavior of the rubbery phase while maintaining slight compressibility

for the chosen form of the constitutive equations and numerical implementation. In addition, the Poisson ratio for the glassy phase is assumed to be 0.4, which is considered similar to other polymers in the glassy phase [125].

The glassy volume fraction is assumed to take the shape of the free recovery extension profile, which is shown in Figure 14(b) to be independent of the value of applied deformation. As a result, the glassy volume fraction is modeled using the hyperbolic tangent equation, the parameters of which are fit to the normalized 10% free recovery extension profile as shown in Figure 19.

In addition, the coefficients of thermal expansion are calibrated from Thermomechanical Analysis (TMA) results that were conducted on cylindrical specimens approximately 4mm in diameter and 5-7mm in length (cf. Section A.2.1.3 of Chapter II).

Finally, the material properties related to the heat transfer ability of the material were calculated using a HotDisk® Thermal Conductivity Analyzer. Two square specimens approximately 2cm x 2cm x 3mmwere machined from a cylindrical specimen that was fabricated using the protocol in Chapter II and cured in a 20mL syringe. In this analysis, the two specimens were used to sandwich the sensor and the temperature increase of the sensor is used to determine the thermal conductivity and specific heat of the SMP specimen.

Presented in Table 8 is the list of all of the material properties that are calibrated – using shape memory tensile tests, thermomechanical analyzer, and thermal conductivity analysis – on the polyurethane shape memory polymer that is described in

more detail in Chapter II. The calibrated model is then used to predict the uniaxial experiments of Chapter II. To perform this simulation, two first order elements were subjected to the uniaxial deformations and temperatures experienced by the dogbone specimens. The resulting simulation for the 10% free recovery experiment, from which many of the material properties were calibrated, is shown in Figure 34(a) and (b), with the stress-temperature results in Figure 34(a) and the extension-temperature results shown in Figure 34(b).

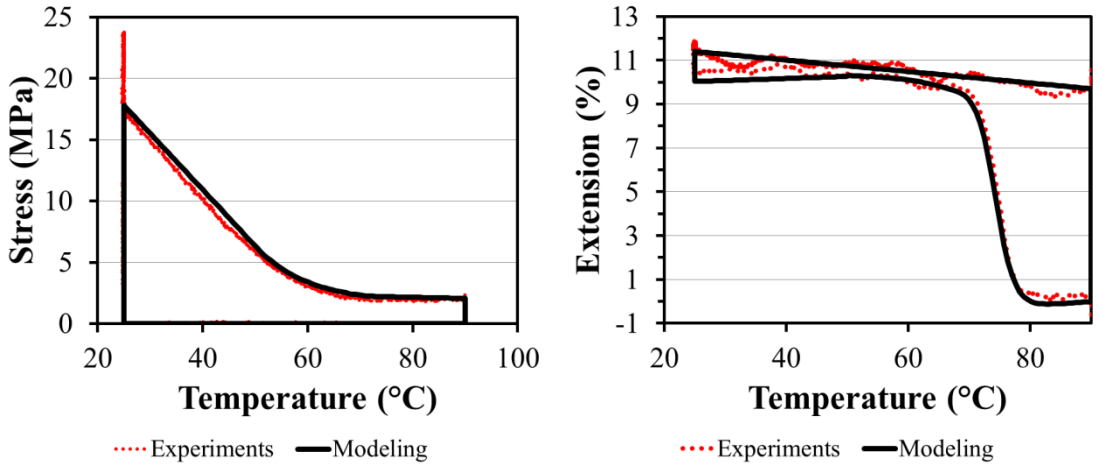

(a) (b)

Figure 34 – Comparison of the (a) stress-temperature and (b) extension-temperature modeling results (solid black line) compared to the experimental data (dotted red line) for the 10% extension free recovery case from which the shear modulus and glassy volume fraction are calibrated. The modeling results are obtained through the Abaqus finite element analysis of a two element, three-dimensional structure subjected to uniaxial tension.

Table 8 – Material properties – calculated from a 10% free recovery experiment, thermal mechanical analysis, and thermal conductivity analysis – used as input to the finite element model using isotropic, compressible neo-Hookean equations.

Parameter	Value
Rubbery phase shear modulus	$\mu^r = 8.5$ MPa
Glassy phase shear modulus	$\mu^g = 648$ MPa
Rubbery phase Lamé coefficient	$\lambda^r = 4244$ MPa
Glassy phase Lamé coefficient	$\lambda^g = 2596$ MPa
Rubbery phase coefficient of thermal expansion	$\alpha^r = 2.1*10^{-4}$ /K
Glassy phase coefficient of thermal expansion	$\alpha^g = 7.8*10^{-5}$ /K
Glassy volume fraction	$\phi(\theta) = C\dfrac{\tanh\left(\dfrac{\theta_{\max}-A}{B}\right)-\tanh\left(\dfrac{\theta-A}{B}\right)}{\tanh\left(\dfrac{\theta_{\max}-A}{B}\right)-\tanh\left(\dfrac{\theta_{\min}-A}{B}\right)}$ $\theta_{\min} = 323,\ \theta_{\max} = 363$ $A = 508.44, B = 18.71, C = 1.00 \quad \theta < 341.1$ $A = 347.25, B = 3.05, C = 0.94 \quad \theta \geq 341.1$
Density	$\rho \approx 1*10^{-6}$ kg/mm^3
Specific heat	$c = 1596$ J/(kg·K)
Thermal conductivity	$k^{th} = 2.946*10^{-4}$ W/(mm·K)

In addition, the finite element subroutine was used to predict the other free recovery cases (15%, 20%, and 25% applied extension) and the constrained recovery cases (10%, 15%, 20%, and 25% applied extension). The comparison of the model predictions to the free and constrained recovery data is shown in Figure 35(a) and (b), respectively.

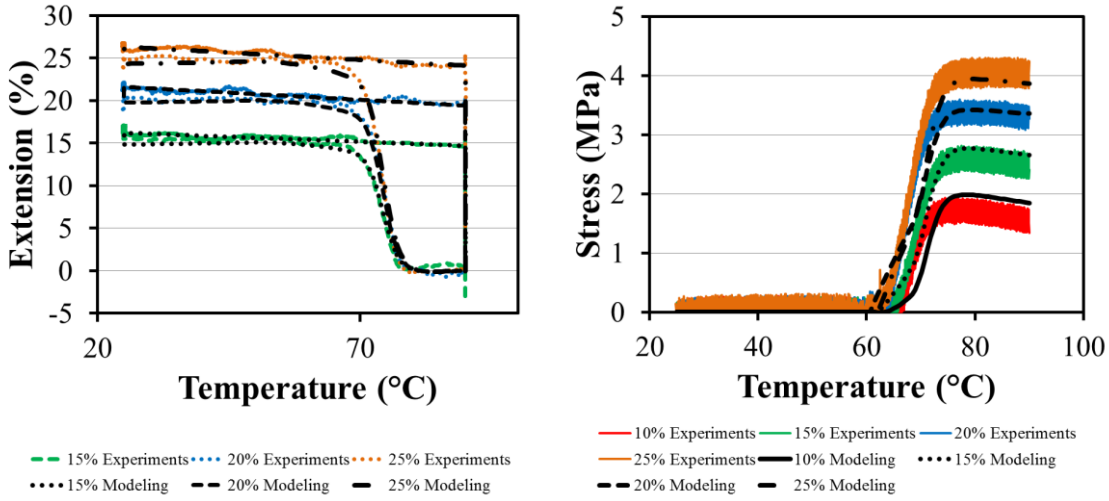

(a) (b)

Figure 35 – Comparison of the model predictions versus experimental results for (a) free recovery and (b) constrained displacement recovery profiles. The modeling results are obtained through the Abaqus finite element analysis of a two element, three-dimensional structure subjected to uniaxial tension. Extensions of 15%, 20%, and 25% are applied in the free recovery analyses, and extensions of 10%, 15%, 20%, and 25% are applied in the constrained displacement recovery analyses.

IV.F. Three-Dimensional Analyses

After calibrating the material properties, the implemented model is used to predict the response of systems undergoing various thermal and mechanical loads. The analyses are performed in Abaqus®, using the user material subroutine described in this chapter. In this work, four geometries are considered – a thin walled cylindrical section, a cylindrical compression sample, and two thrombectomy device designs.

IV.F.1. Thin-Walled Cylindrical Tube

Polymeric stents have been developed [11] with complex geometries that allow for sufficient radial recovery force while maintaining lateral flexibility through tortuous pathways. An example of one such stent is shown in Figure 36, which is based off the work of [41, 58, 61], where the solid rings primarily provide the radial recovery and the 'S' shaped struts provide flexibility for navigating narrow arteries. The analyses in this section consider the expansion and the crimping of a simplified geometry as a first step toward modeling the complete stent with a complex geometry.

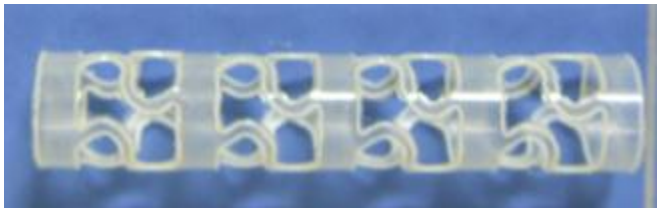

Figure 36 – Prototype of a shape memory polymer neurovascular stent. Courtesy of Landon Nash, Texas A&M University.

IV.F.1.1. Expansion of a Thin-Walled Cylinder

The first analysis considers a thin-walled cylinder that could be considered similar to one of the solid rings in the SMP stent. In the analysis, a tube of length 10 mm, inner diameter of 20mm, and thickness 0.5mm is considered. For purposes of analysis, symmetry conditions are applied such that only $1/8^{th}$ of the tube is considered in the computational analysis.

The tube begins at 90°C and is then expanded radially by 5mm, applied to the outer surface. Maintaining this radial expansion, the temperature is decreased uniformly to 25°C. After cooling to the glassy phase, the radial displacement boundary condition is released and the cylinder remains in its temporary shape. The cylinder is then heated, under zero applied load, back to 90°C and full recovery is observed. Figure 37(a) shows the boundary condition setup, with the radial expansion applied to the outer surface. In addition, Figure 37(b) shows the expanded tube, with the contours representing the maximum principal logarithmic strain in the tube, as compared to the original tube.

IV.F.1.2. Crimping of a Thin-Walled Cylinder

In inserting stent-like devices into the body, the device must first be crimped down before delivering through a catheter. As a first step toward modeling the crimping of a complex stent, this analysis considers a thin-walled cylinder that is crimped to a 4 point star. The geometry of the undeformed tube has a length of 20mm in length, an inner diameter of 10mm, and a thickness of 0.25mm. For computational saving,.

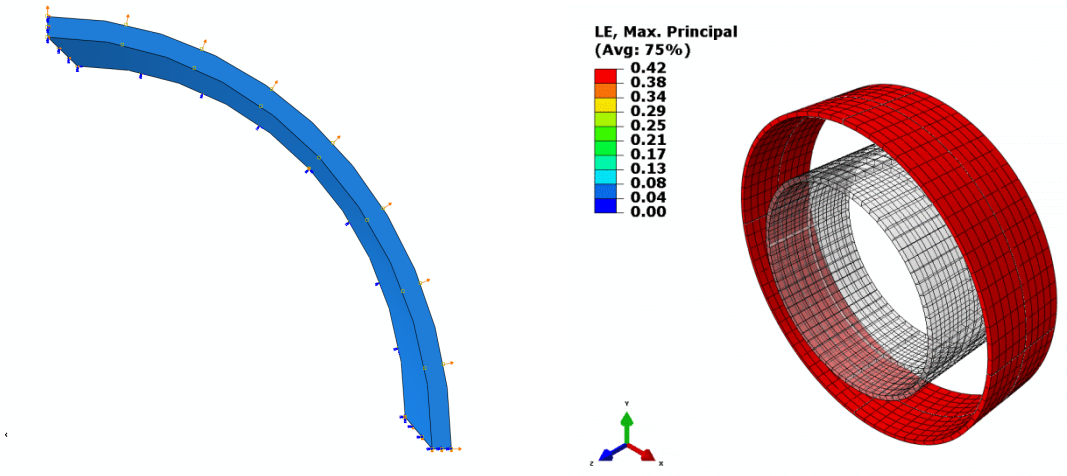

(a) (b)

Figure 37 – (a) Analysis setup showing the radial expansion of 1/8th of a thin-walled cylinder, and (b) the expanded configuration compared to the original configuration of the tube. The tube was expanded radially by 5mm, applied to the outer surface. The contours in (b) represent the maximum principal strain in the tube, with a uniform value of 0.41 mm/mm.

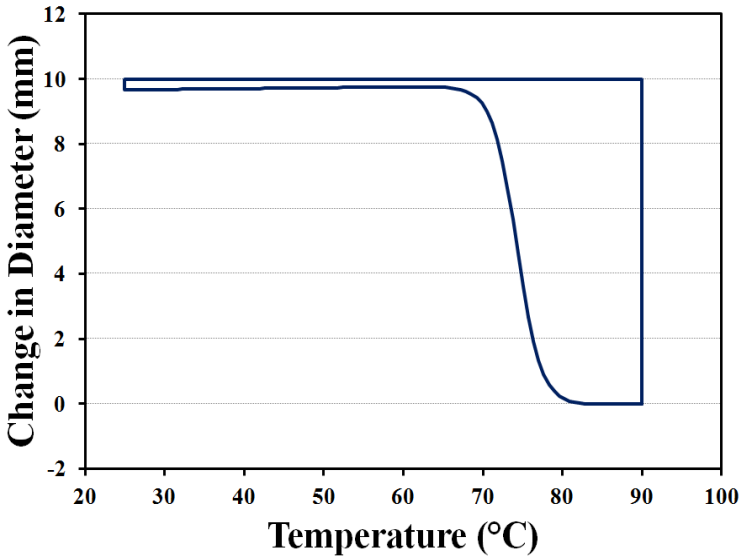

Figure 38 - Change in diameter as a function of temperature for the thin-walled cylinder. The cylinder, modeled as 1/8th of the full geometry, is expanded radially by 5mm at 90°C, cooled to 25°C maintaining a constant diameter, released, and then heated under zero applied load to 90°C.

symmetry conditions are enforced and 1/8th of the initial geometry is modeled in Abaqus

In performing the crimping, the tube temperature is initially 90°C, at which the SMP is in the rubbery phase. An inward radial displacement of 4.5mm is then applied to the nodes along the 45 degree line, as shown in Figure 39(a). The comparison of the entire geometry before and after the crimping is shown in Figure 39(b). After deforming, the tube is cooled – maintaining the applied displacement – to 25°C, at which the SMP is completely in the glassy phase. The displacement boundary condition is then removed, and the tube is again heated to 90°C with zero applied load.

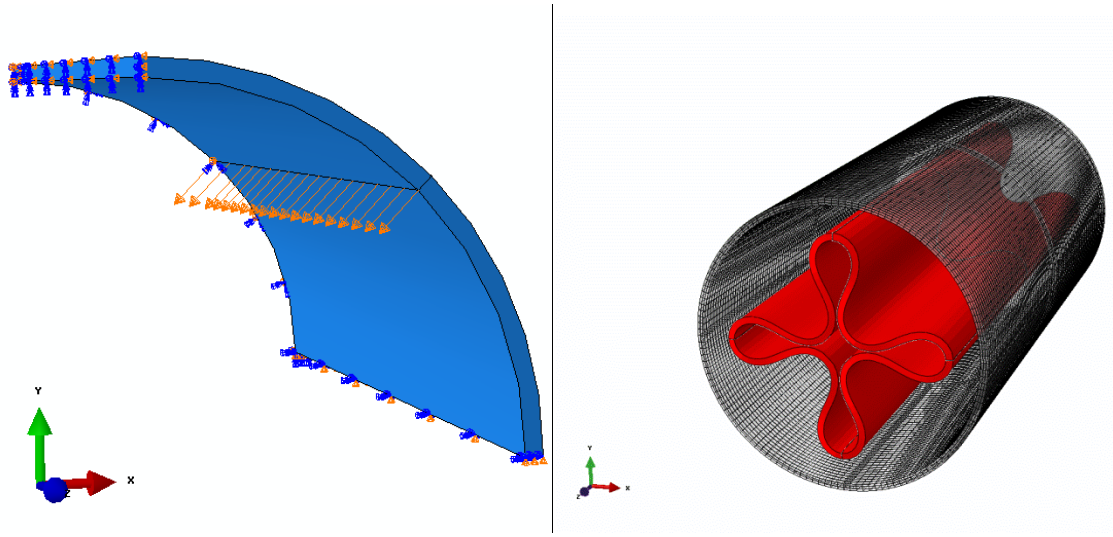

(a) (b)

Figure 39 – (a) Analysis setup showing the inward radial displacement of 1/8th of a thin-walled cylinder along the 45° nodes, and (b) the crimped configuration compared to the original configuration of the tube. The tube was crimped by applying a radial displacement of 4.5mm to the nodes along the 45° line.

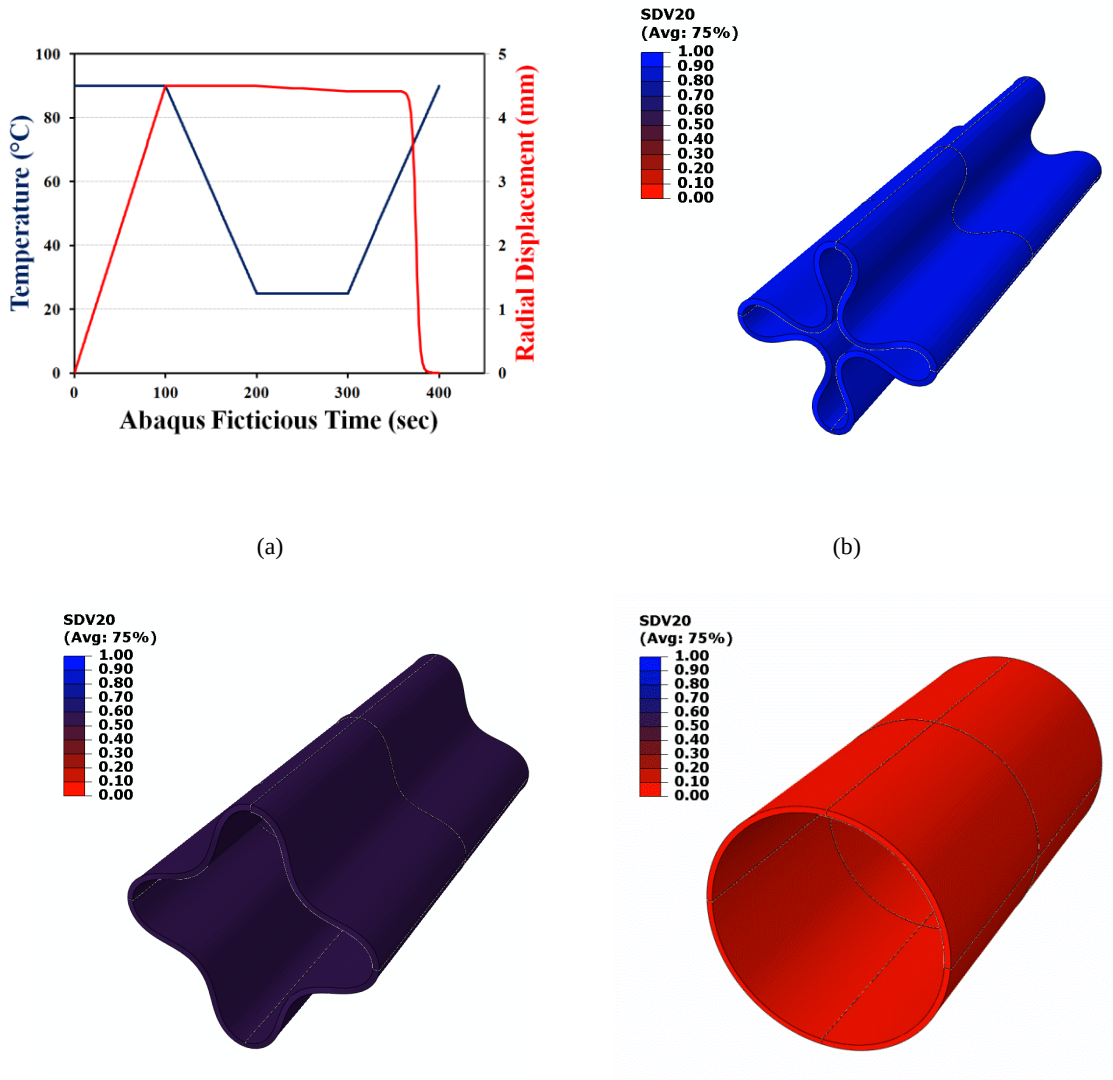

Figure 40 – (a) Radial displacement and temperature profile for one node on the 45° line (i.e., where the radial displacement is applied) plotted as a function of the fictitious analysis time, and the glassy volume fraction (GVF) contours for (b) the beginning of the shape recovery (GVF = 1.0), (c) the middle of shape recovery (GVF = 0.5), and (d) the end of recovery (GVF = 0.0).

Figure 40(a) presents the temperature and radial displacement of a node along the 45° line on the interior surface of the cylinder – the region in which the displacement boundary conditions were applied. Figure 40(b) – (d) shows the contour plots and shape of the crimped tube as it is heated through recovery. Specifically, Figure 40(b) shows the device at the beginning of the recovery heating (i.e., after crimping, cooling, and unloading) when the glassy volume fraction is equal to 1.0, Figure 40(c) shows the device once the glassy volume fraction has decreased to 0.5, and Figure 40(d) shows the device at the end of the recovery heating once the glassy volume fraction has reached 0.0.

IV.F.2. Cylindrical Compression Sample

In these analyses, a cylindrical compression sample is modeled to predict the response of a cylindrical sample undergoing compressive loading and to show the effects of applying different temperature boundary conditions during the recovery process. Specifically, a cylindrical specimen with a diameter of 20mm and length of 20mm is subjected to the free recovery shape memory cycle. The bottom of the specimen was not allowed to move vertically. The top of the specimen was placed in contact with and deformed by a compression platen. 'Hard' contact was used to prevent penetration of the top surface of the SMP into the compression platen, and the interaction between the SMP and the platen was assumed to be frictionless. As shown in Figure 1(a), only ¼ of the SMP is modeled with symmetry conditions enforced.

The initial temperature for the entire material was set to be 90°C so that the material was in equilibrium at the rubbery phase. The compression platen was then

moved down to compress the sample by 10% extension. The undeformed and deformed configurations are compared in Figure 41(b). During cooling to 25°C, the platen is slowly moved up to reflect the thermal contraction of the platen and the connecting extension rods.

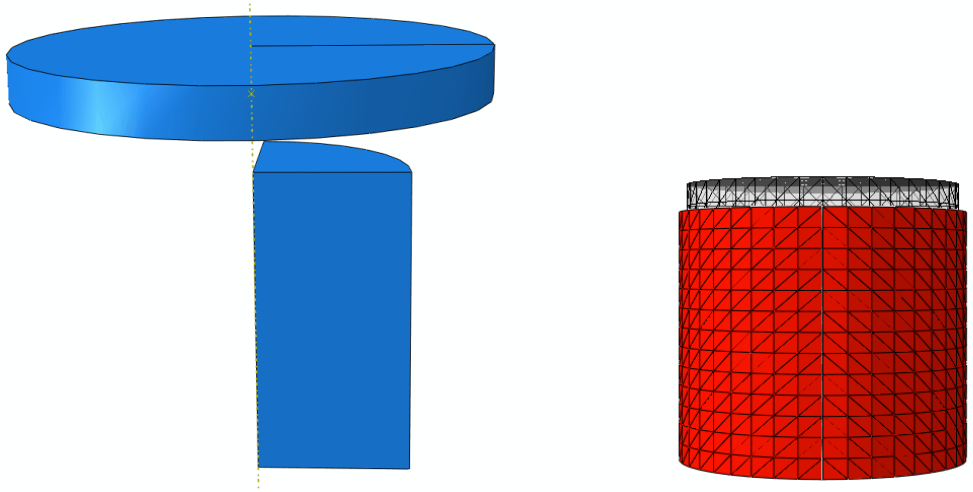

(a) (b)

Figure 41 – (a) Setup of the finite element assembly, modeling ¼ of the shape memory polymer cylinder and a rigid compression platen used to deform the SMP. (b) A comparison of the shape memory cylinder in the undeformed and deformed configurations at 90°C. The SMP was compressed by 10%, and the compression platen is not shown for clarity.

Preliminary experiments have shown the compression platen and attached extension rod move upward, after a delay of 11 minutes when heated/cooled at 1°C/min, by 0.39mm. These experimental observations are incorporated into the finite element analyses by beginning to move the compression platen 11 minutes after the cooling is initiated (at a temperature rate of 1°C/min). The associated displacement profile is such that the fixture moves up linearly by 0.39mm for the remainder of the cooling procedure.

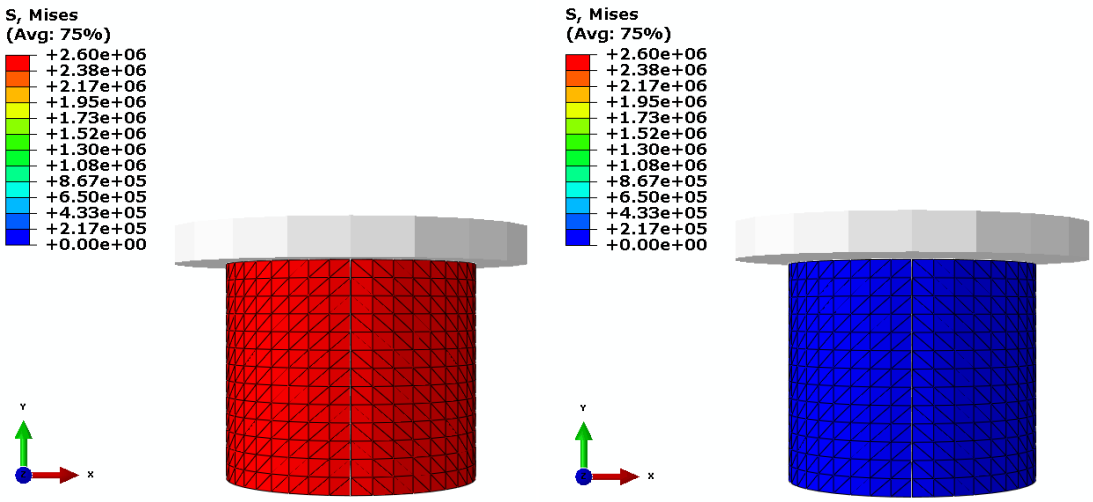

(a) (b)

Figure 42 – Comparison of the von Mises stress in the SMP at (a) the beginning of the constrained cooling procedure (temperature = 90°C, glassy volume fraction = 0)and at (b) the end of the cooling procedure (temperature = 25°C, glassy volume fraction = 1). The stress becomes zero as the SMP is locked in the temporary shape and the platen moves upward due to thermal contraction.

The specimen is then reheated to observe the shape recovery. In these analyses, the effects of the temperature boundary conditions are exploited. In particular, four different temperature boundary conditions are considered, including:

1. Cooling and heating the whole material uniformly – applying the temperature change to all of the nodes at the same time
2. Cooling and heating only the top and bottom of the specimen with the lateral surface insulated
3. Cooling and heating all exterior surfaces (top, bottom, and lateral surface)

4. Cooling and heating the lateral surface at a prescribed temperature rate with a slower temperature change on top and bottom (i.e., to model the effects that might be experienced due to the time necessary to heat/cool the compression platens that are in contact with the specimen)

Case 1 is analyzed using standard three-dimensional continuum elements with a uniform temperature assigned to each node. To model the cases 2-4, the transient heat transfer capability of Abaqus® was used in conjunction with the coupled thermal-displacement elements to allow for the simultaneous heat transfer and shape memory effect. In the transient cases, the temperature rate (on the relevant boundaries) was increased at a rate of 1°C/min. Pictorial results for each of the transient sections will first be presented, and then a comparison of the temperature of the center node versus time will be presented. In addition, the model predictions in case 1 and 4 are compared to a preliminary experimental result on a SMP cylindrical sample exposed to a free recovery shape memory thermomechanical load path in Appendix B.

IV.F.2.1. Uniform Heating

In this first case, the temperature change required to induce the shape recovery during the final heating step was prescribed uniformly to each node. In other words, this scenario represents the quasi-static heating case in which the temperature rate is assumed to be sufficiently slow to raise the temperature of the cylinder uniformly. Figure 43 shows the stress and strain response for the entire shape memory cycle. In tracing the

path of the state of the material, the SMP first begins at 90°C. The compression platen is then lowered along path (1) to induce a compressive strain and stress in the material.

After loading, the material is cooled along path (2). When cooling from 90°C to 80°C, the strain remains nearly constant while the magnitude of the stress decreases slightly, which is due to thermal contraction of the rubbery phase and the onset of the glass transition. At approximately 80°C, the compression platen begins to move up due to thermal contraction of the platen and the extension rod. As the platen moves up, the SMP elastically recovers some of the applied strain. At 65°C, the transition to the glass phase is complete, the applied deformation is stored, and the platen loses contact with the shape memory polymer causing the stress to go to zero. From 65°C to 25°C, the thermal contraction of the material in the glassy phase is observed.

After the cooling step is complete, the platen is moved upward to not interfere with the specimen recovery, and the temperature is raised from 25°C to 90°C. With no applied loads, the SMP undergoes free recovery. From 25°C to 65°C, thermal expansion of the glassy phase is observed. Starting at approximately 65°C, the transition from the glassy phase to the rubbery phase initiates, and the SMP recovers all of the applied deformation.

IV.F.2.2. Heating the Top and Bottom

The first coupled temperature-displacement analysis considers the behavior of the material if the top and bottom of the material were heated while the lateral surfaces were kept insulated. In this simulation, the temperature is increased on the top and

bottom surfaces at a rate of 1°C/min. Figure 44(a) and (b) show the response of the cylinder (cross-sectional view) when the applied temperature is approximately 66°C and

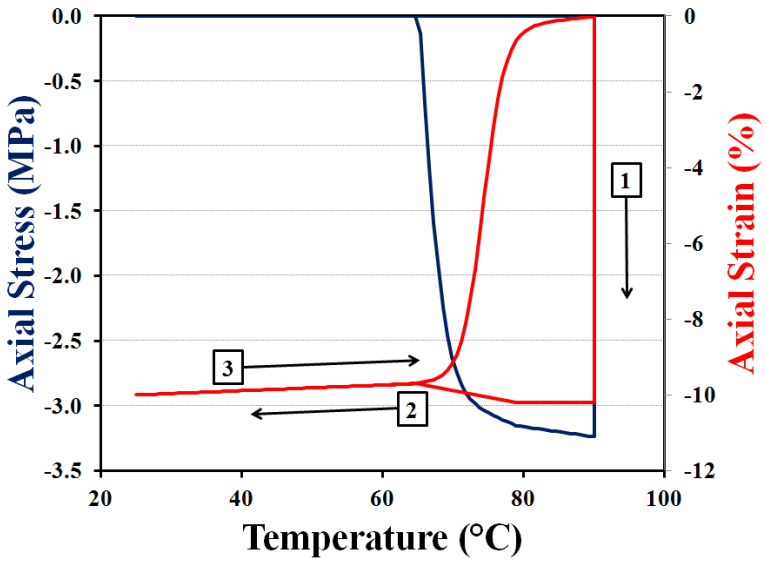

Figure 43 – Simulation of a compression experiment performed on a cylindrical SMP sample. 10% compressive strain is applied along path (1). The material is then cooled along path (2) and the magnitude of the stress decreases to 0 due to thermal contraction and the phase transition. The SMP is subsequently heated along path (3) at zero applied load to induce shape recovery.

76°C, respectively. The temperature is observed to increase first on the vertical faces while there is a delay in heating the interior of the SMP. In particular, due to the insulated boundary conditions, the temperature is observed to be constant for points sharing the same vertical coordinate. Further, in Figure 44(b), the temperature gradient induces a curvature along the top and bottom of the horizontal surfaces, creating a barreling effect due to the faster recovery in these regions.

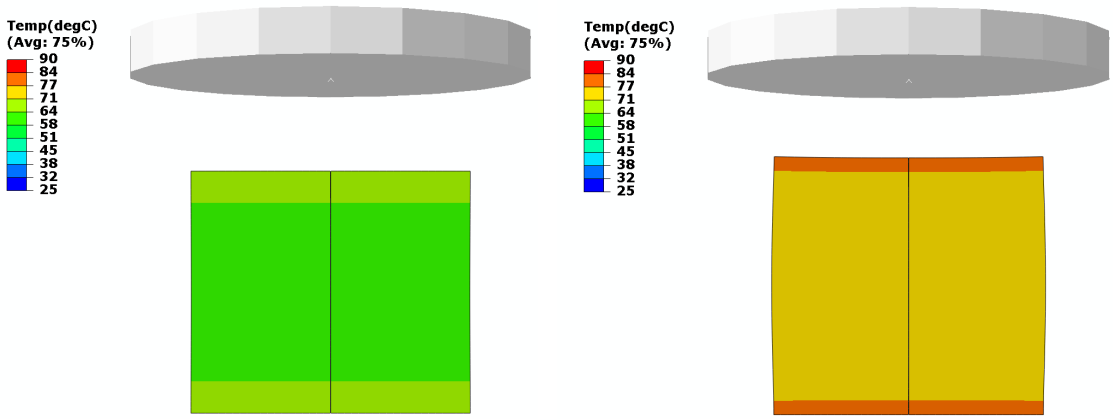

(a) (b)

Figure 44 – Cross-sectional view of the shape memory polymer cylinder when the applied temperature is approximately (a) 66°C and (b) 76°C. The temperature change is applied on the top and bottom surfaces, and the circumferential surface is kept insulated.

IV.F.2.3. Heating All Exterior Surfaces

In a variation to the coupled temperature-displacement analysis, this simulation now considers the scenario in which all exterior edges are heated uniformly. Specifically, the top, bottom, and circumferential surfaces are heated at a temperature rate of 1°C/min. Figure 45(a) and (b) present the cross-sectional view of the cylinder when the external temperature is approximately 66°C and 76°C, respectively. It is observed that the temperature increases near the edges while there is delay in the temperature increase in a concentric region on the interior of the SMP.

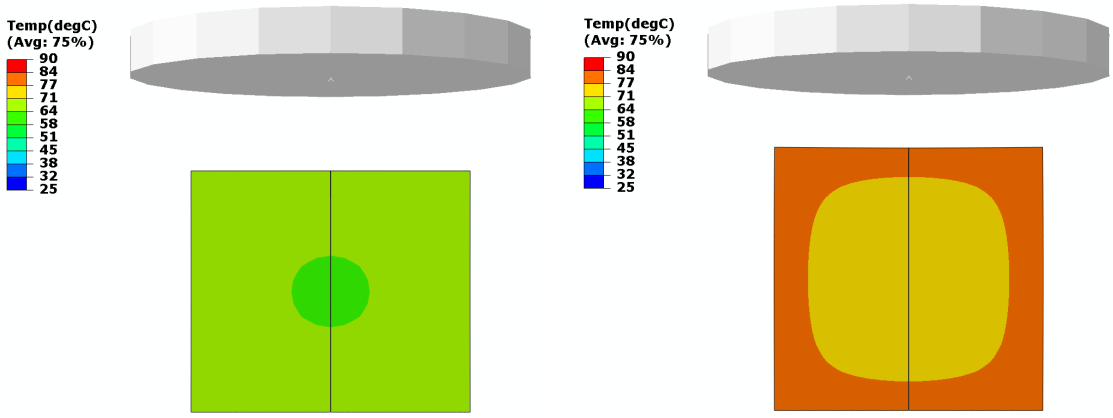

(a) (b)

Figure 45 – Cross-sectional view of the shape memory polymer cylinder when the applied temperature is approximately (a) 66°C and (b) 76°C. The temperature change is applied on the top, bottom, and circumferential surfaces.

IV.F.2.4. Heating All Exterior Surfaces with a Delay on Top and Bottom

The final variation to the transient coupled temperature-displacement analysis considers a scenario in which the circumferential surface is heated at the nominal temperature rate while the top and bottom surfaces are heated differently. Specifically, the circumferential surface is heated from 25°C to 90°C at a temperature rate of 1°C/min. The top and bottom surfaces are held at 25°C for 11 minutes, and then heated to 90°C at a temperature rate of 1°C/min. The delay in heating the top and bottom surfaces is intended to approximate the effects of these surfaces being in contact or near the compression platens. Figure 46(a) and (b) present the temperature gradients in the cross-sectional view of the cylinder when the circumferential temperatures are approximately 66°C and 76°C, respectively. It is observed that the temperature increases in a parabolic manner toward the center of the specimen.

IV.F.2.5. Comparison of the Center Node Temperature as a Function of Time

Four analyses have been performed that consider the effects of different temperature boundary conditions during the free recovery heating of a shape memory polymer cylinder. The first scenario assumed the cylinder was heated uniformly through the thickness, while the remaining scenarios applied the temperature gradients to combinations of the top, bottom, and circumferential surfaces. Figure 47 presents the temperature at the center of the specimen as a function of time. The nominal applied temperature profile is shown in black. It is observed that the center remains approximately 1-5°C cooler than the applied temperature, dependent on the temperature boundary conditions. Figure 48 presents the displacement of the node in the center of the top surface during the recovery heating. It is observed that, compared to heating all exterior surfaces, the displacement recovery is delayed by 2 minutes when only the top and bottom surfaces are heated and by 4 minutes when the top and bottom surfaces are heated slower than the circumferential surface.

IV.F.3. Thrombectomy Device

In the final set of analyses, the user material subroutine developed in this work is used to model the response of a thrombectomy device that has been proposed for the removal of blood clots. The device, based on the work of [41], is crimped down, and then deployed in a "net-like" manner to remove the clot. A prototype of this device was demonstrated [42] to be capable of heating via magnetic induction and the incorporation of ferromagnetic particles. The analysis performed in work considers only

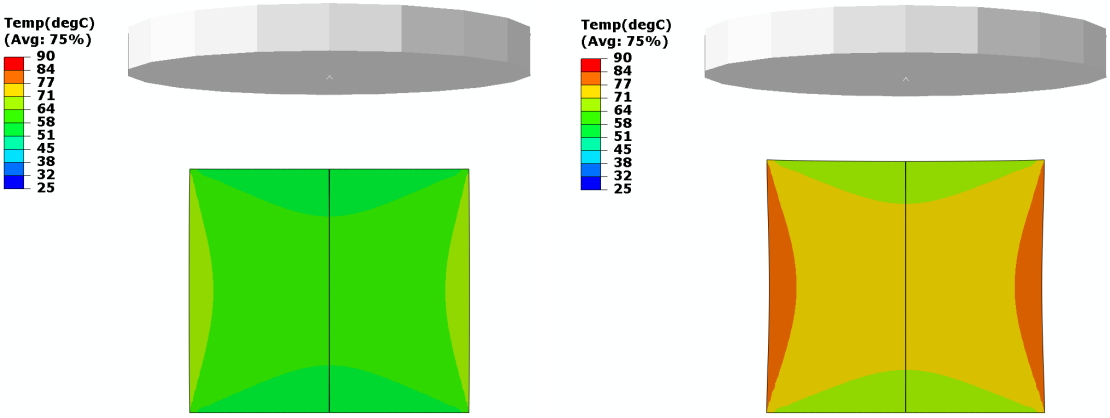

(a) (b)

Figure 46 – Cross-sectional view of the shape memory polymer cylinder when the applied circumferential temperature is approximately (a) 66°C and (b) 76°C. A temperature change of 1°C/min is applied to the circumferential surface. To approximate the effects of being near or in contact with the compression platens, the top and bottom surfaces are held at a constant temperature for 11 minutes before being heated at a temperature rate of 1°C/min.

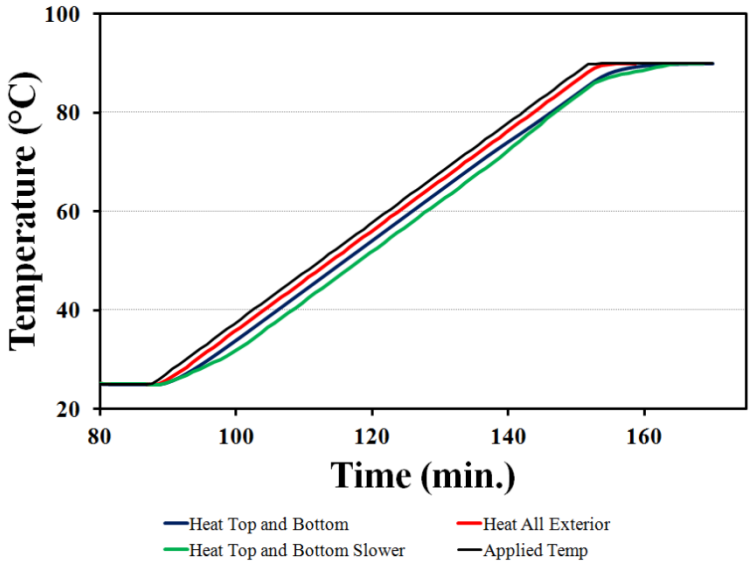

Figure 47 – Comparison of the temperature in the center of the specimen for the three simulations with transient boundary conditions. The temperature for the three cases is compared to the nominal applied temperature, shown in black. As all three transient cases were prescribed the same cooling boundary conditions, only the recovery heating portion of the temperature profile is pictured.

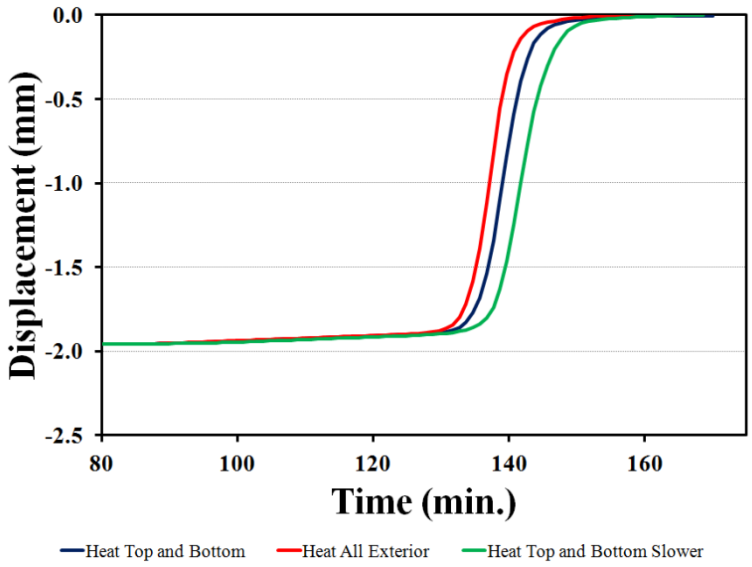

Figure 48 – Comparison of the displacement of the center node on the top surface as a function of time during the recovery heating for the three transient boundary conditions. As compared to heating all external surfaces uniformly (red line), it is observed that the motion of the center node is delayed by approximately 5 minutes when the top and bottom surfaces are heated slower than the circumferential surface (green line).

the neat shape memory polymer, without ferromagnetic particles, and the response of the device when subjected to temperature boundary conditions rather than magnetic.

In this work, the effects of heating the core of the device at different temperature rates, up to 5°C/min, are studied. In these preliminary analyses, potential external forces (e.g., fluid flow, contact with arterial walls, etc.) are not considered. In other words, these analyses consider only the material response as a result only of the loads necessary to deform the device into its secondary shape.

IV.F.3.1. Device Geometry

The device in this work is composed of a thick walled cylinder that serves as the center plug that provides strength and a component to help with device delivery. Surrounding the center plug are two levels of patterned loops. The first, inner level consists of eight loops that are almost diamond in shape. The second, outer level consists of eight larger loops that have a curved outer region. The outer diameter of the device is 12mm. The thickness of the device, outside of the center core, is 0.5mm and the width of the struts is approximately 0.2mm.

For computational purposes, the net-like device is modeled using $1/16^{th}$ symmetry, and is crimped using an analytical rigid funnel. The inner radius of the funnel is 6.5 mm, and the funnel has a curved leading edge to facilitate a smooth transition when crimping the device. The hard contact feature in Abaqus is enforced such that there is no penetration between the device and the funnel. In addition, the surface between the funnel and the device is modeled as frictionless. The setup of the finite element geometry, with symmetry invoked on the thrombectomy device, is shown in Figure 49(a) and (b). In addition, Figure 49(b) shows a top-view comparison of the diameter of the device compared to the inner diameter of the funnel.

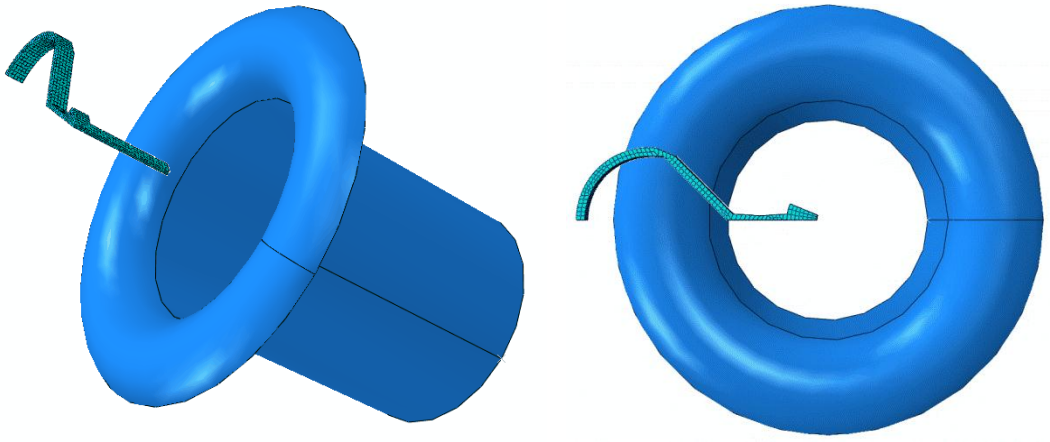

(a) (b)

Figure 49 – Setup of the finite element geometry for the net-like thrombectomy device, as viewed (a) from the side and (b) from the top. The device, 12mm in outer diameter, is modeled using 1/16th symmetry and is crimped using an analytical rigid funnel 6.5mm in inner diameter.

IV.F.3.2. Setting the Temporary Shape

In this analysis, the device is set to an initial temperature of 90°C, at which the SMP is in the rubbery phase and above the transition temperature range. To crimp the device, the bottom of the stem is held fixed and the funnel is slid over the device causing the 'pedals' of the device to bend away from the center stem. Figure 50 shows the device as it is being crimped by the funnel. The funnel in its initial, intermediate, and fully crimped states is shown in the first, second, and third rows, respectively. The glassy volume fraction (SDV20) is shown in the left set of contours and the von Mises stress is shown in the right set of contours. Due to the temperature being 90°C, the glassy volume fraction is observed to be equal to 0.0. In addition, stress concentrations are observed in the struts of the inner loops that connect to the center plug – the region that experiences the highest degree of bending.

The device is then cooled uniformly to 25°C while constrained inside the funnel. Once completely locked in the glassy phase, the funnel is removed and the device is locked in its temporary shape. This shape represents the configuration in which the device would be transported through the catheter. Figure 51 shows the device at the end of the cooling step (top row) and after removing the funnel (bottom row). It is observed that the glassy volume fraction is equal to 1.0 as the SMP has completely cooled to the glassy phase. In addition, the cooling procedure decreased the stress concentrations in much of the device (cf. stress contours in the first row of Figure 51 to those in the last row of Figure 50). This decrease is due to the thermal contraction, which relieves a portion of the stress due to the device shrinking and partially elastically unloading. A further decrease in the stresses is observed in the bottom row of Figure 51 as the funnel is removed and no additional loads are applied to the device.

IV.F.3.3. Device Actuation

Finally, the device is heated to 90°C, with zero applied loads, and recovery of the original shape is observed. In this work, the recovery of the device is simulated under five temperature boundary conditions. In the first case, the temperature change is assigned to all nodes such that the device heats uniformly. In the remaining cases, the temperature gradient is applied only to the center stem region at rates of 1°C/min, 2°C/min, 5°C/min, and 65°C/min respectively.

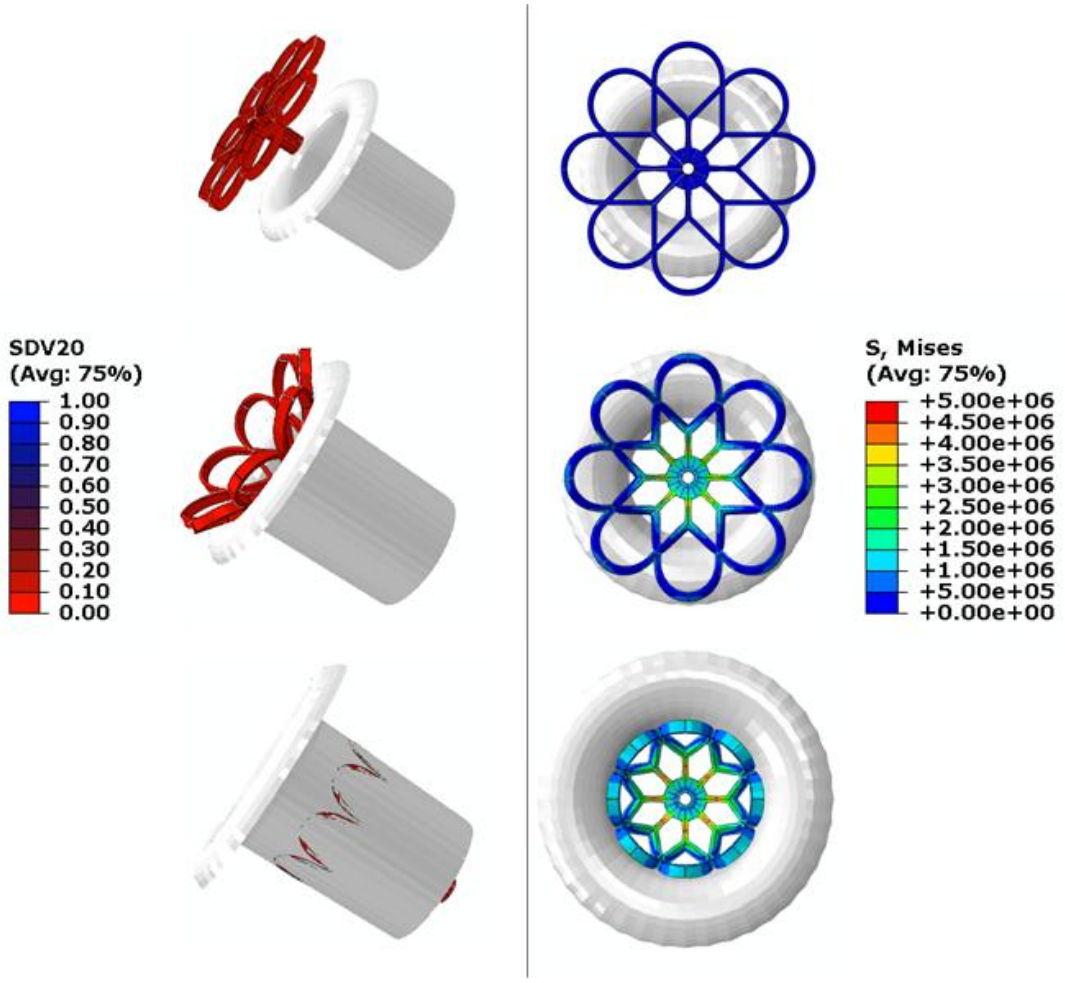

Figure 50 – Crimping of the net-like thrombectomy device, as shown from a side view (left) and a top view (right). The initial state of the device is shown in the first row, the device in the middle of crimping is shown in the second row, and the device fully crimped is shown in the last row. The contours indicate the glassy volume fraction (left) and the von Mises stress (right).

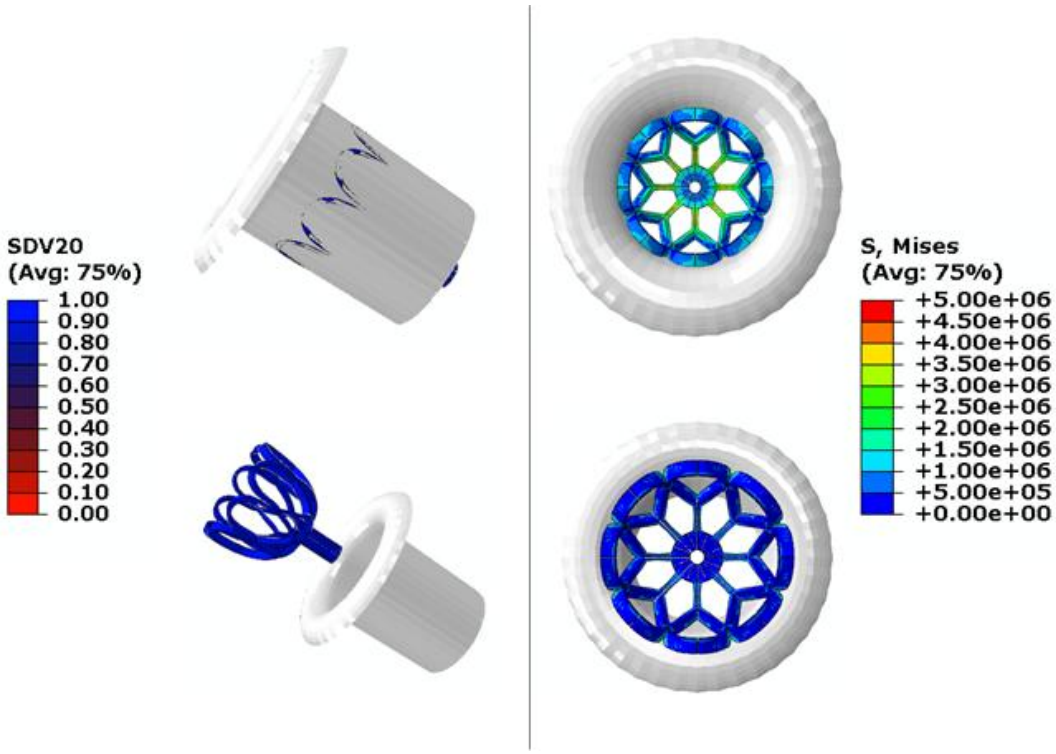

Figure 51 – Cooling and removal of the funnel in the shape setting process of the net-like thrombectomy device, as shown from a side view (left) and a top view (right). The first row shows the device as cooled inside the funnel, and the second row shows the device with the funnel removed after cooling. The contours indicate the glassy volume fraction (left) and the von Mises stress (right).

IV.F.3.3.1. Uniform Heating

In this simulation, the temperature gradient during recovery was applied to all nodes at the same time. As such, the temperature increased uniformly throughout the device. Figure 52 shows the progression of the device recovery at approximately 48°C, 79°C, 83°C, and 90°C. It is observed that nearly full actuation is observed once the temperature reaches 79°C.

Figure 52 – Recovery progression of the net-like thrombectomy device when the temperature increase is applied to all nodes uniformly. Pictured, from left to right, is the device at approximately 48°C, 79°C, 83°C, and 90°C. The device is observed to finish actuation at approximately 79°C.

IV.F.3.3.2. Heating Core at 1°C/min

In this simulation, the temperature gradient was applied only to the center core of the device at a rate of 1°C/min. The surfaces on the remainder of the device are kept insulated. Figure 53 shows the progression of the device recovery at approximately 48°C, 79°C, 83°C, and 90°C. It is observed that the temperature profile is nearly uniform; however, a slight temperature gradient is observed between the center core and the outer regions of the device. It is observed that nearly full actuation is observed once the core temperature reaches 83°C.

IV.F.3.3.3. Heating Core at 2°C/min

In this simulation, the temperature gradient was applied only to the center core of the device at a rate of 2°C/min, and the surfaces on the remainder of the device are kept insulated. Figure 54 shows the progression of the device recovery at approximately 48°C, 79°C, 83°C, and 90°C. A larger temperature gradient is observed between the

center core and the outer regions of the device, and this temperature gradient begins to noticeably slow the early stages of the shape recovery (cf. Figure 53). It is observed that nearly full actuation is observed once the core temperature reaches approximately 83°C.

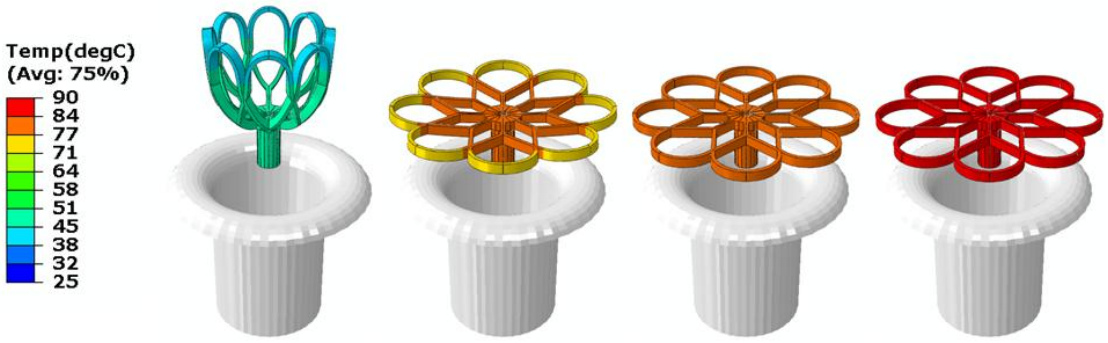

Figure 53 - Recovery progression of the net-like thrombectomy device when the temperature increase is applied to the center core at a temperature rate of 1°C/min. Pictured, from left to right, is the device at approximately 48°C, 79°C, 83°C, and 90°C. The device is observed to finish actuation once the core temperature reaches approximately 83°C.

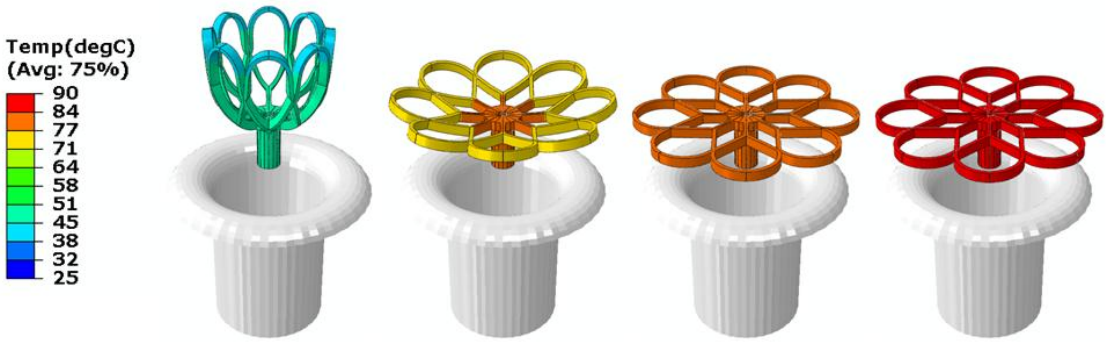

Figure 54 - Recovery progression of the net-like thrombectomy device when the temperature increase is applied to the center core at a temperature rate of 2°C/min. Pictured, from left to right, is the device at approximately 48°C, 79°C, 83°C, and 90°C. The device is observed to finish actuation once the core temperature reaches approximately 83°C.

IV.F.3.3.4. Heating Core at 5°C/min

In the third transient simulation, the temperature gradient was applied only to the center core of the device at a rate of 5°C/min, and the surfaces on the remainder of the device are kept insulated. Figure 55 shows the progression of the device recovery at approximately 48°C, 79°C, 83°C, and 90°C. A significant temperature gradient (~10°C) is observed between the center core and the outer regions of the device. As such, a noticeable delay in the shape recovery is observed in each step of the recovery process. Full actuation is observed once the core temperature reaches approximately 90°C.

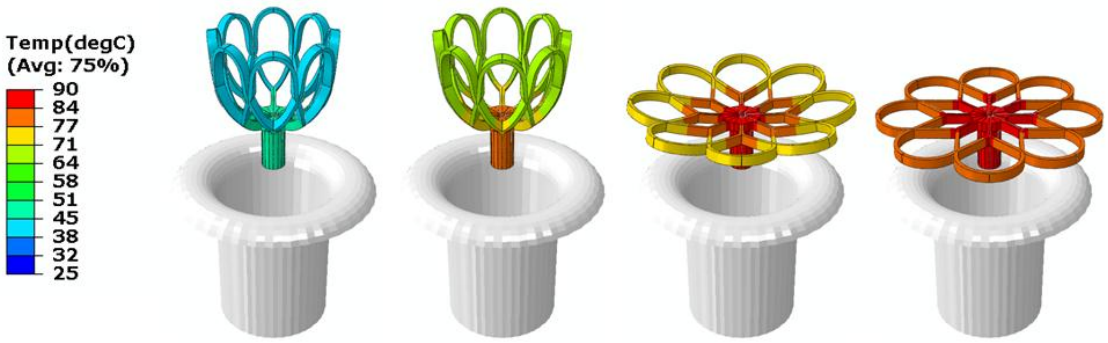

Figure 55 - Recovery progression of the net-like thrombectomy device when the temperature increase is applied to the center core at a temperature rate of 5°C/min. Pictured, from left to right, is the device at approximately 48°C, 79°C, 83°C, and 90°C. The device is observed to finish actuation once the core temperature reaches approximately 90°C.

IV.F.3.3.5. Heating Core at 65°C/min

In the fourth transient simulation, the temperature gradient was applied only to the center core of the device at a rate of 65°C/min, and the surfaces on the remainder of the device are kept insulated. This temperature rate is used to model a rate closer to a

rate that may be expected during practical device deployment. It is noted, however, that the insulated boundary conditions on the remainder of the device are not representative of an actual deployment environment. As such, the focus of this simulation is to demonstrate the capabilities for predicting the delay of device deployment due to much faster temperature rates. Additional future work should consider the effects of natural and/or forced convection to provide a more accurate prediction for the time necessary to fully deploy the device. Figure 56 shows the progression of the device recovery at approximately 48°C, 79°C, 83°C, and 90°C. A significant temperature gradient is observed between the center core and the outer regions of the device, and actuation of the device is not observed even when the core of the device first reaches 90°C.

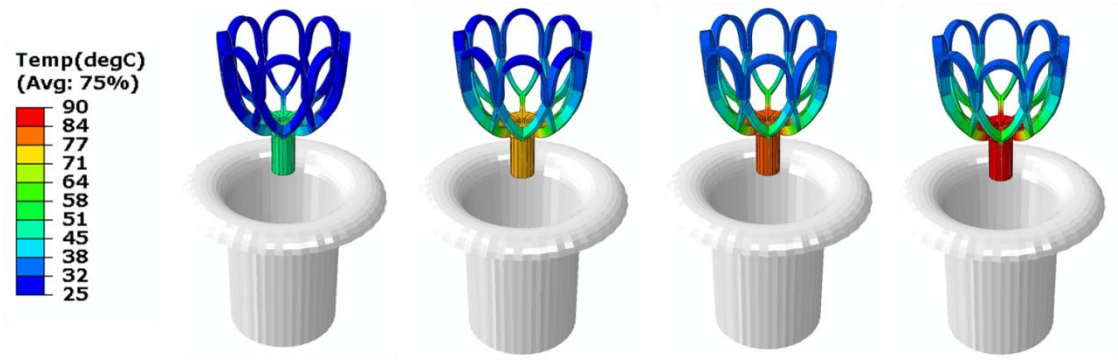

Figure 56 - Recovery progression of the net-like thrombectomy device when the temperature increase is applied to the center core at a temperature rate of 5°C/min. Pictured, from left to right, is the device at approximately 48°C, 79°C, 83°C, and 90°C. The device is observed to finish actuation once the core temperature reaches approximately 90°C.

IV.F.3.3.6. Recovery Comparison

In this section, a quantitative comparison of the device recovery as a function of the temperature conditions is presented. The previous sections showed pictorial evidence of the effects of the temperature boundary conditions on the device actuation. Recall that, in the cases where a temperature rate was prescribed, the temperature gradient was applied to the core of the device and the remainder of the device was treated as insulated. Figure 57 presents the magnitude of the displacement of the tip of the device as a function of the temperature rate. It is observed that the shift in the tip recovery temperature is approximately 1°C, 2°C, and 9°C for temperature rates of 1°C/min, 2°C/min, and 5°C/min, respectively, as compared to the uniformly heated (quasi-static) device deployment. In addition, Figure 58 presents the temperature at the outer edge (tip) as a function of time, which has been normalized by the time necessary to heat the core to 90°C. A small delay is observed in heating the tip for temperature rates of 1°C/min, 2°C/min, and 5°C/min while it takes over 5 times the time to heat the tip when the core is heated at 65°C/min.

The effects of heating the core at 65°C/min can further be seen in Figure 59, in which the magnitude of the tip displacement is plotted as a function of heating time. Although the core of the device heats in 1 minute, it is observed that the device does not complete actuation until approximately 4 minutes after the start of heating.

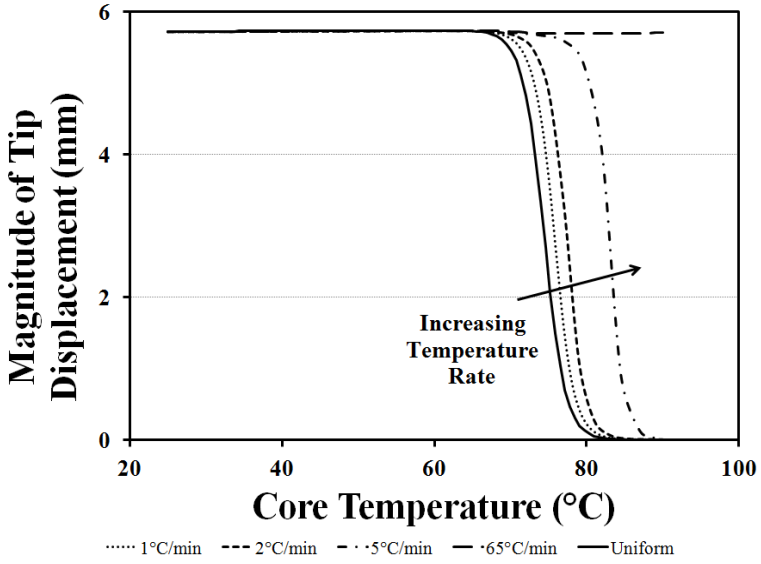

Figure 57 – Comparison of the magnitude of the tip displacement as a function of the core temperature for uniform (quasi-static) heating as well as heating the core at temperature rates of 1°C/min, 2°C/min, and 5°C/min.

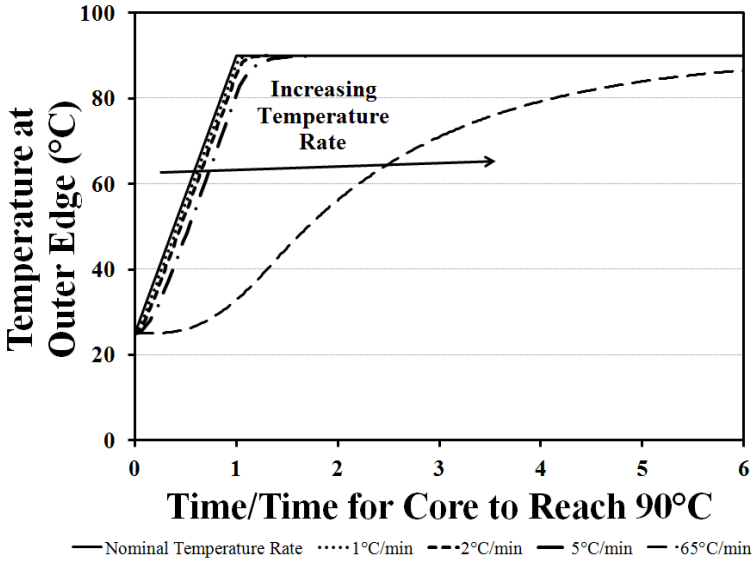

Figure 58 – Comparison of the temperature of the edge of the device as a time for the increasing temperature rates. The horizontal axis is normalized by the time it takes the core in each scenario to reach 90°C.

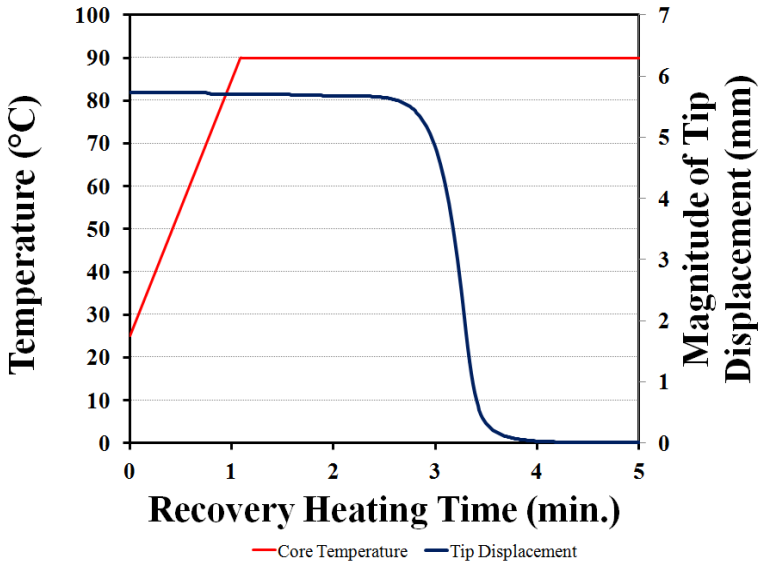

Figure 59 – Tip displacement as a function of the recovery heating time when heating the core at 65°C/min. The heating profile of the core is shown for comparison.

IV.G. Summary and Conclusions

In this chapter, a large deformation model for shape memory polymer was implemented in a three-dimensional user material subroutine in Abaqus – a commercially available finite element software. The kinematics were derived assuming the shape memory polymer consisted of a thermoelastic rubbery phase and a thermoelastic glassy phase, in which the deformation applied in the rubbery phase was stored during cooling. The average deformation gradient was obtained through a volume average of the deformation gradient of the rubbery phase and the deformation gradient of the glassy phase. An evolution equation was introduced for the recovery of the stored deformation during subsequent heating. Specifically, the evolution equation assumed

the stored deformation was recovered proportional to the glassy volume fraction during heating.

The constitutive equations for the glassy and rubbery phases were assumed to take the form of a compressible neo-Hookean response, in which the Helmholtz free energy was derived in terms of the first and third invariants of the right Cauchy-Green deformation tensor. These constitutive equations provided a more general framework than the incompressible neo-Hookean equations of the previous chapter, for which a specific boundary value problem must be solved or for which special considerations (e.g., penalty method) must be taken during the finite element implementation.

The numerical implementation was performed such that the system of equations to be solved was dependent on the temperature, and thus the glassy volume fraction, of the SMP. In particular, for temperatures at which the glassy volume fraction is 0 or 1, the average deformation gradient was reduced to an explicit relationship in terms of the rubbery and glassy deformation gradients, respectively. These deformation gradients were then substituted into the respective single phase constitutive equations to find the updated stress in the material. For intermediate temperatures, the constitutive equations for both phases and the kinematics were solved simultaneously assuming the stress in the rubbery and glassy phases was equal. The system of equations (i.e., kinematics and assumption that the rubbery stress was equal to the glassy stress) were solved using the Newton-Raphson method to find the updated stretches in the rubbery and glassy phase, which were then used to find the updated stress in the SMP.

The Abaqus user material subroutine was then used to analyze a series of three-dimensional boundary value problems. The material properties were calibrated to the experiments performed in Chapter II, and the UMAT was used to predict the response of the remaining uniaxial free and constrained displacement recovery experiments. The UMAT was then used to simulate the response of thin walled cylinders undergoing expansion and crimping procedures. In the expansion procedure, a thin walled cylinder was expanded to twice the original diameter and allowed to recover to its original shape. In the crimping analyses, a longer thin walled cylinder was crimped to a four point star and then heated for free recovery.

In addition, heat transfer and thermoelastic coupling were used to analyze the effects of heating the SMP at faster temperature rates. The balance of energy and entropy inequality equations were solved to find the relationship between the change in temperature and the change in the strain, and the thermoelastic coupling terms were coded in the user material subroutine for coupled thermomechanical analyses. The associated material parameters, namely the specific heat and the thermal conductivity, were experimentally obtained via testing samples of the polyurethane SMP on a HotDisk® Thermal Conductivity Analyzer. Coupled thermal-displacement analyses were performed on more complex geometries and loading conditions. In the first set of analyses, a compression cylinder 20mm in length and 20mm in diameter was loaded via a compression platen and subjected to the shape memory effect thermal cycle. The effects of heating the SMP with different thermal boundary conditions on the exterior surfaces was analyzed, and it was observed that the effects of the realistic thermal

boundary conditions delayed the shape recovery up to 5 minutes as compared to assuming the SMP is undergoing quasi-static (uniform heating). Additionally, the crimping and actuation of a thrombectomy device was analyzed. The thrombectomy device was first heated and crimped using an analytical funnel. After cooling and removing the funnel, the core of the device was heated using temperature rates of 1°C/min, 2°C/min, and 5°C/min while the remaining surfaces were kept insulated. It was observed that the shift in the recovery temperature, as measured by the change in displacement of the outer region of the device, was up to 9°C for temperature rates up to 5°C/min.

CHAPTER V

CONCLUSIONS AND FUTURE WORK

This dissertation focused on the experimental characterization and constitutive modeling of shape memory polymers. These efforts focused on enhancing the understanding of a new shape memory polymer system and developing an experimentally calibrated and validated finite element tool that is capable of predicting the response of shape memory polymer devices.

V.A. Experimental Characterization

Tests were performed on a polyurethane shape memory polymer that was previously untested in terms of its shape memory capability. The material was fabricated in a custom mold and cut to dogbone specimens that were tested. The SMP was tested under both free recovery and constrained displacement recovery conditions at applied extensions of 10%, 15%, 20%, and 25%. In performing the experiments, modifications to the thermomechanical load path were introduced. For free recovery experiments, the specimen was ungripped at the end of the cooling and unloading steps. As a result, it was ensured that no loads were applied to the material during the recovery heating process. During the constrained displacement recovery heating, out-of-plane motion due to thermal loads was observed while the material was heated in the glassy phase. To avoid this effect and better isolate the true material response, the bottom grip was released at the start of the recovery heating. Thus, the SMP was allowed to hang

freely under zero applied load at the beginning of the heating step. Before the material reached the temperature range at which recovery was expected, the bottom of the specimen was re-gripped and the displacement was held constant, which induced the desired tensile stress as the material attempted to return to its original, permanent shape.

In both recovery cases, the displacement of the material was measured using a laser extensometer. The use of this non-contact measurement technique provided the capability to measure the strain of the material during the free recovery experiments (i.e., when the specimen was not gripped on bottom and the tensile tester crosshead was not moving). In addition, the strain of the material was measured during the constrained cooling step. Compared to using the crosshead of the tensile tester during the cooling step to calculate the strain, the laser extensometer revealed the deformation that was being imposed on the specimen due to the thermal contraction of the grips and the extension rods. This deformation was subsequently minimized by utilizing the PID parameters of the tensile tester to move the crosshead as necessary to minimize the change in the strain the sample, as measured by the laser extensometer, during the constrained cooling process.

In the initial loading path, the polyurethane shape memory polymer exhibited a stress-strain response that was approximately linear. In addition, the SMP was observed to recover all of the applied deformation, for all values of extension, in the free recovery experiments. For the constrained displacement recovery, the SMP was observed to recover up to 4.2MPa for an applied extension of 25%. The recovery of the SMP occurred at the same temperature, regardless of the amount of applied deformation. The

shape memory polymer, however, was able to withstand larger strains during isothermal strain-to-failure experiments (up to 55%) as compared to shape memory experiments (up to 25%) when in the rubbery phase. This difference is believed to be a result of the time that the SMP is held at the large deformations. In the isothermal experiments, the loading step is relatively rapid and there is no time for microscopic defects to propagate throughout the specimen. In the shape memory experiment, the material is loaded and then held at constant displacement as cooling is initiated. Thus, more time is allowed for the propagation of defects at the start of the constrained cooling, which is when failure of the SMP was usually observed.

While this work further developed the experimental techniques for testing shape memory polymers and contributed to the understanding of a new shape memory polymer that is being considered for biomedical devices, additional studies should be performed to fully understand the effects of these materials. For instance, additional focus should be devoted to understanding and optimizing the processing conditions, which nay help maximize the amount of deformation the SMPs can be subjected to for shape memory cycles. In addition, experiments should be performed to evaluate the effects of strain rate and loading temperature on the elastic response as well as the strength and shape recovery ability of the material.

V.B. Constitutive Modeling

In this dissertation, a finite deformation model was implemented in 1-D and 3-D to model the response of the shape memory polymers. The model considered the

material as a mixture of the rubbery and glassy phases. Specifically, the average deformation gradient was derived through a volume averaging technique that accounted for the deformation gradient of the material still in the rubbery phase and the deformation gradient of the material that had transformed from the rubbery phase to the glassy phase. As part of this volume averaging, a glassy volume fraction was introduced to represent the fraction of the material that was in the glassy phase at a given temperature. Motivated through experimental observations that the transformation was independent of the applied stress or strain, the glassy volume fraction was assumed to be a function of only temperature. In performing the volume average, the stress was assumed to be spatially constant in the representative volume element. Consistent with this assumption, it was further assumed that the rotations of the rubbery and glassy phases were equal to that of the average rotation of the SMP. As a result, the expression for the average deformation gradient was reduced to an expression for the average stretch as a function of the stretches in the rubbery and glassy phases. Further, an evolution equation was introduced that assumed the stored deformation was recovered proportional to the glassy volume fraction during the recovery heating process.

Focusing on only the thermoelastic response and experimentally observing the stress-strain response of both phases were approximately linear for all values of applied deformation, this work assumed each phase behaved as a neo-Hookean material. In the 1-D modeling, incompressible neo-Hookean constitutive equations were used. The hydrostatic pressure term required to maintain incompressibility was eliminated due to the consideration of uniaxial boundary value problems. In the 3-D modeling,

compressible neo-Hookean constitutive equations were used for both the rubbery and the glassy phases. These compressible constitutive equations provided more generality for shape memory polymers in which at least one of the phases does not exhibit incompressibility. In addition, the compressible constitutive equations provided a more convenient means to three-dimensional numerical implementation by avoiding the need to invoke a penalty method to account for the indeterminate hydrostatic pressure term.

In these modeling efforts, the material properties were calibrated from experimental results. Specifically, the elastic properties of the rubbery phase and glassy phase were calibrated from the loading and unloading steps, respectively, in a shape memory experiment. The coefficients of thermal expansion were calibrated in 1-D to fit the stress-temperature increase observed during constrained cooling and were subsequently calibrated using thermomechanical analysis results for the three-dimensional implementation and analyses. The glassy volume fraction was assumed to take the shape of the extension-temperature during free recovery heating. As a result, a hyperbolic tangent function was introduced and the coefficients were calibrated, using a least squares method, to fit the function to a normalized 10% extension free recovery experiment.

The model was then implemented in a three-dimensional user material subroutine in Abaqus and represented the first three-dimensional implementation using the kinematics proposed by [42]. In the pure rubbery and glassy phases, an explicit equation was obtained for the new deformation gradients and the stress was obtained through substitution into the constitutive equations. When both the rubbery and glassy phases

coexisted, the system of equations was solved using a Newton-Raphson method assuming the stress in the rubbery phase was equal to that in the glassy phase. The model predictions matched well with the uniaxial experimental results.

In addition, heat transfer and thermoelastic coupling were introduced by considering the first and second laws of thermodynamics and Fourier's law to result in an equation for the change in the material temperature as a function of the change in the strain of the material. The heat transfer material properties were calibrated from experimental results obtained on a HotDisk Thermal Conductivity Analyzer and used as input to the user material subroutine.

Upon implementing and calibrating the model, the subroutine was used to analyze a series of boundary value problems. First, thin-walled cylinders were subjected to expansion or crimping deformations, cooled to lock in the permanent shape, and then heated under zero applied load to recover the original shape. In addition, a compression test was simulated. Specifically, a cylindrical SMP was deformed via a compression platen, cooled to its temporary shape, and then heated under different thermal boundary conditions under zero applied load. Through these simulations, it is expected that the SMP cylinder would recover its permanent shape up to 5 minutes later (when heated at 1°C/min) than if the material was undergoing quasi-static heating. Finally, a net-like thrombectomy device was crimped using an analytical rigid funnel, cooled to its temporary shape, and then the core of the device is heated at temperature rates of 1°C/min to 5°C/min. It is predicted that the core of the device would need to be heated approximately 9°C hotter in the faster heating rate (5°C/min) case than in the slower

heating rate (1°C/min) case to achieve the same amount of shape recovery, as measured by the magnitude of the exterior edge tip displacement.

These modeling efforts developed a tool that can is capable of predicting the response of shape memory polymers, in complex geometries, to complex loading and thermal boundary conditions. While the introduction of the evolution equation for the strain recovery during heating improved the efficiency of the UMAT, future efforts should focus on better improving the run times and robustness of this finite element tool. One possible approach would be to optimize the numerical algorithms in the current subroutine. As this model considers the relationship between two discrete phases with discrete thermodynamic potentials, another approach to improve the tool would be to develop an alternate formulation of the material response from a unified thermodynamics potential. This alternate formulation may result in a more efficient method for solving the system of equations (i.e., as compared to the current Newton-Raphson method) as well as a better defined tangent modulus (i.e., as compared to the current rule of mixtures approach between the rubbery and glassy phases).

In addition to improving the computational aspects of the current subroutine, future efforts should consider expanding this model to include viscoelastic strain rate effects, options for different rubbery and glassy constitutive behavior (e.g. Mooney-Rivlin, etc.), and validating the three-dimensional model predictions. Ideally, multiaxial testing in conjunction with thermal imaging techniques should be performed to compare the displacements, forces and pressures, and temperatures to the finite element predictions for complex loading and thermal boundary conditions.

REFERENCES

[1] A. Lendlein and S. Kelch, Shape Memory Polymers, Angew Andte Chemie-International Edition 41 (2002) 2034-2057.

[2] B. Dietsch and T. Tong, A Review - Features and Benefits of Shape Memory Polymers (SMPs), Journal of Advanced Materials 39 (2007) 3-12.

[3] P. T. Mather, X. Luo, and I. A. Rousseau, Shape Memory Polymer Research, Annual Review of Materials Research 39 (2009) 445-471.

[4] C. Liu, H. Qin, and P. Mather, Review of Progress in Shape Memory Polymers, Journal of Materials Chemistry 17 (2007) 1543-1558.

[5] M. Behl and A. Lendlein, Shape Memory Polymers, Materials Today 10 (2007) 20-28.

[6] J. Hu, Y. Zhu, H. Huang, and J. Li, Recent Advances in Shape Memory Polymers: Structure, Mechanism, Functionality, Modeling, and Applications, Progress in Polymer Science (2012) 1-155.

[7] J. Leng, X. Lan, Y. Liu, and S. Du, Electroactive Thermoset Shape Memory Polymer Nanocomposite Filled with Nanocarbon Powders, Smart Materials & Structures 18 (2009) 1-7.

[8] L. Sun, W. M. Huang, Z. Ding, Y. Zhao, C. C. Wang, *et al.*, Stimulus-Responsive Shape Memory Materials: A Review, Materials and Design 33 (2012) 577-640.

[9] T. Xie, Recent Advances in Polymer Shape Memory Polymer 52 (2011) 4985-5000.

[10] Y. Liu, K. Gall, M. L. Dunn, A. R. Greenberg, and J. Diani, Thermomechanics of Shape Memory Polymers: Uniaxial Experiments and Constitutive Modeling, International Journal of Plasticity 22 (2006) 279-313.

[11] J. William D. Callister, Materials Science and Engineering: An Introduction, 6 ed. New York, NY: John Wiley & Sons, Inc., 2003.

[12] P. C. Hiemenz and T. P. Lodge, Polymer Chemistry, 2 ed. Boca Raton, FL: CRC Press, 2007.

[13] G. Baer, T. S. Wilson, D. L. Matthews, and D. J. Maitland, Shape Memory Behavior of Thermally Stimulated Polyurethane for Medical Applications, Journal of Applied Polymer Science 103 (2006) 3882-3892.

[14] B. L. Volk, D. C. Lagoudas, Y.-C. Chen, and K. S. Whitley, Analysis of the Finite Deformation Response of Shape Memory Polymers: I. Thermomechanical Characterization, Smart Materials and Structures 19 (2010) 1-10.

[15] P. A. Toensmeir. (2005) Radical Departure. *Aviation Week Space Technology*. 72-73.

[16] J. Manzo and E. Garcia, Methodology for Design of an Active Rigidity Joint, Journal of Intelligent Material Systems and Structures 20 (2009) 311-327.

[17] Y. Zhou, F. Guan, and L. Qian, The Application of Shape Memory Polymer Composite in Space Deployable Truss Structure, Advanced Materials Research 287-290 (2011) 2756-2759.

[18] Q. Meng and J. Hu, A Review of Shape Memory Polymer Composites and Blends, Composites: Part A 40 (2009) 1661-1672.

[19] D. Ratna and J. Karger-Kocsis, Recent Advances in Shape Memory Polymers and Composites: A Review, Journal of Materials Science 43 (2008) 254-269.

[20] Z. G. Wei, R. Sandstrom, and S. Miyazaki, Shape Memory Materials and Hybrid Composites for Smart Systems: Part I - Shape Memory Materials, Journal of Materials Science 33 (1998) 3743-3762.

[21] J. T. Choi, T. D. Dao, K. M. Oh, H.-i. Lee, H. M. Jeong, *et al.*, Shape Memory Polyurethane Nanocomposites with Functionalized Graphene, Smart Materials & Structures 21 (2012) 1-9.

[22] J. M. Cuevas, R. Rubio, J. M. Laza, J. L. Vilas, M. Rodriguez, *et al.*, Shape Memory Composites Based on Glass-Fibre-Reinforced Poly(ethylene)-Like Polymers, Smart Materials & Structures 21 (2012).

[23] K. Gall, M. L. Dunn, Y. Liu, D. Finch, M. Lake, *et al.*, Shape Memory Polymer Nanocomposites, Acta Materialia 50 (2002) 5115-5126.

[24] K. Gall, M. Mikulas, N. A. Munshi, F. Beavers, and M. Tupper, Carbon Fiber Reinforced Shape Memory Polymer Composites, Journal of Intelligent Material Systems and Structures 11 (2000) 877-886.

[25] J. Leng, X. Lan, Y. Liu, and S. Du, Electroactive Thermoset Shape Memory Polymer Nanocomposite Filled with Nanocarbon Powders, Smart Materials & Structures 18 (2009).

[26] J. S. Leng, W. M. Huang, X. Lan, Y. J. Liu, and S. Y. Du, Significantly Reducing Electrical Resistivity by Forming Conductive Ni Chains in a Polyurethane Shape Memory Polymer/Carbon-Black Composite, Applied Physics Letters 92 (2008) 1-3.

[27] Y. Liu, K. Gall, M. L. Dunn, and P. McCluskey, Thermomechanics of Shape Memory Polymer Nanocomposites, Mechanics of Materials 36 (2004) 929-940.

[28] Y. Liu, H. Lv, X. Lan, J. Leng, and S. Du, Review of Electroactive Shape Memory Polymer Composite, Composites Science and Technology 69 (2009) 2064-2068.

[29] S. A. Madbouly and A. Lendlein, Shape Memory Polymer Composites, Advanced Polymer Science 226 (2010) 41-95.

[30] Q. Ni, C. Zhang, Y. Fu, G. Dai, and T. Kimura, Shape Memory Effect and Mechanical Properties of Carbon Nanotube/Shape Memory Polymer Nanocomposites, Composite Structures 81 (2007) 176-184.

[31] M. Nishikawa and M. Hojo, "Analysis of the Shape-Recovery Performance of Thermally-Activated Shape Memory Polymer Composite with Microstructural Heterogeneities," in *Behavior and Mechanics of Multifunctional Materials and Composites*, San Diego, CA, 2012, pp. 1-7.

[32] M. Nishikawa, K. Wakatsuki, A. Yoshimura, and N. Takeda, Effect of Fiber Arrangement on Shape Fixity and Shape Recovery in Thermally Activated Shape Memory Polymer-Based Composites, Composites Part A: Applied Science and Manufacturing 43 (2011) 1-34.

[33] J. Nji and G. Li, Damage Healing Ability of a Shape Memory Polymer-Based Particulate Composite with Small Thermoplsatic Contents, Smart Materials & Structures 21 (2012) 1-10.

[34] N. G. Sahoo, Y. C. Jung, and J. W. Cho, Electroactive Shape Memory Effect of Polyurethane Composites Filled with Carbon Nanotubes and Conducting Polymer, Materials and Manufacturing Processes 22 (2007) 419-423.

[35] N. G. Sahoo, Y. C. Jung, N. S. Goo, and J. W. Cho, Conducting Shape Memory Polyurethane-Polypyrrole Composites for an Electroactive Actuator, Macromolecular Materials and Engineering 290 (2005) 1049-1055.

[36] H. Tobushi, S. Hayashi, K. Hoshio, Y. Makino, and N. Miwa, Bending Actuation Characteristics of Shape Memory Composite with SMA and SMP, Journal of Intelligent Material Systems and Structures 17 (2006) 1075-1081.

[37] H. Tobushi, E. Pieczyska, Y. Ejiri, and T. Sakuragi, Thermomechanical Properties of Shape Memory Alloy and Polymer and Their Composites, Mechanics of Advanced Materials and Structures 16 (2009) 236-247.

[38] H. Yang and L. Y. Wang, Thermomechanical Analysis of Shape Memory Composite Tape Spring, Applied Composite Materials (2012) 1-15.

[39] D. M. Phillips and J. W. Baur, "Thermal Activation of Shape Memory Polymers Through Vascular Means," in *ASME 2011 Conference on Smart Materials, Adaptive Structures, and Intelligent Systems*, Scottsdale, AZ, 2011, pp. 135-140.

[40] J. Leng, D. Zhang, Y. Liu, K. Yu, and X. Lan, Study on the Activation of Styrene-Based Shape Memory Polymer by Medium-Infrared Laser Light, Applied Physics Letters 96 (2010) 1-3.

[41] G. M. Baer, W. Small IV, T. S. Wilson, W. J. Benett, D. L. Matthews, *et al.*, Fabrication and In Vitro Deployment of a Laser-Activated Shape Memory Polymer Vascular Stent, Biomedical Engineering Online 6 (2007) 1-8.

[42] P. R. Buckley, G. H. McKinley, T. S. Wilson, W. Small IV, W. J. Benett, *et al.*, Inductively Heated Shape Memory Polymer for the Magnetic Actuation of Medical Devices, IEEE Transactions on Biomedical Engineering 53 (2006) 2075-2083.

[43] D. J. Maitland, W. Small, J. M. Ortega, P. R. Buckley, J. Rodriguez, *et al.*, Prototype Laser-Activated Shape Memory Polymer Foam Device for Embolic Treatment of Aneurysms. , Journal of Biomedical Optics 12 (2007) 1-3.

[44] W. Small IV, P. R. Buckley, T. S. Wilson, J. M. Loge, K. D. Maitland, *et al.*, Fabrication and Characterization of Cylindrical Light Diffusers Comprised of Shape Memory Polymer Journal of Biomedical Optics 13 (2008) 1-7.

[45] W. Small IV, M. F. Metzger, T. S. Wilson, and D. J. Maitland, Laser-Activated Shape Memory Polymer Microactuator for Thrombus Removal Following Ischmeic Stroke: Preliminary In Vitro Analysis, IEEE Journal of Selected Topics in Quantum Electronics 11 (2005) 892-901.

[46] R. Mohr, K. Kratz, T. Weigel, M. Lucka-Gabor, M. Moneke, *et al.*, Initiation of Shape Memory Effect by Inductive Heating of Magnetic Nanoparticles in Thermoplastic Polymers, Proceedings of the National Academy of Sciences 103 (2006) 3540-3545.

[47] A. M. Schmidt, Electromagnetic Activation of Shape Memory Polymer Networks Containing Magnetic Nanoparticles, Macromolecular Rapid Communications 27 (2006) 1168-1172.

[48] J. Leng, H. Lv, Y. Liu, and S. Du, Electroactive Shape Memory Polymer Filled with Nanocarbon Particles and Short Carbon Fibers, Applied Physics Letters 91 (2007) 1-3.

[49] A. Lendlein, M. Behl, B. Hiebl, and C. Wischke, Shape Memory Polymers as a Platform for Biomedical Applications, Expert Reviews Medical Devices 7 (2010) 357-379.

[50] A. Lendlein and S. Kelch, Shape Memory Polymers as Stimuli-Sensitive Implant Materials Clinical Hemorheology and Microcirculation 32 (2005) 105-116.

[51] A. Lendlein and R. Langer, Biodegradable, Elastic Shape Memory Polymers for Potential Biomedical Applications, Science 296 (2002) 1673-1676.

[52] D. J. Maitland, W. Small IV, P. Singhal, W. Hwang, J. N. Rodriguez, *et al.*, "Design and Realization of Biomedical Devices Based on Shape Memory Polymers," in *Material Research Society* San Francisco, CA, 2009, pp. NN06-01.

[53] W. Small IV, T. S. Wilson, P. Singhal, and D. J. Maitland, Biomedical Applications of Thermally Actuated Shape Memory Polymers, Journal of Materials Chemistry 20 (2010) 3356-3366.

[54] W. M. Huang, C. L. Song, Y. Q. Fu, C. C. Wang, Y. Zhao, *et al.*, Shaping Tissue with Shape Memory Materials, Advanced Drug Delivery Reviews (2012) 1-21.

[55] K. Takashima, T. Noritsugu, J. Rossiter, S. Guo, and T. Mukai, Curved Type Pneumatic Artificial Rubber Muscle Using Shape Memory Polymer, Journal of Robotics and Mechatronics 24 (2012) 472-479.

[56] M. Ahmad, J. Luo, and M. Miraftab, Feasibility Study of Polyurethane Shape Memory Polymer Actuators for Pressure Bandage Application, Science and Technology of Advanced Materials 13 (2012) 1-7.

[57] J. M. Ortega, W. Small, T. S. Wilson, W. J. Benett, J. M. Loge, *et al.*, A Shape Memory Polymer Dialysis Needle Adapter for the Reduction of Hemodynamic Stress Within Arteriovenous Grafts IEEE Transactions on Biomedical Engineering 54 (2007) 1722-1724.

[58] G. M. Baer, T. S. Wilson, W. Small IV, J. Hartman, W. J. Benett, *et al.*, Thermomechanical Properties, Collapse Pressure, and Expansion of Shape

Memory Polymer Neurovascular Stent Prototypes, Journal of Biomedical Materials Research Part B: Applied Biomaterials 90B (2009) 421-429.

[59] L. Xue, S. Dai, and Z. Li, Synthesis and Characterization of Elastic Star Shape Memory Polymers as Self-Expandable Drug-Eluting Stents, Journal of Materials Chemistry 22 (2012) 7403-7411.

[60] X. Yu, L. Wang, M. Huang, T. Gong, W. Li, *et al.*, A Shape Memory Stent of Poly(E-Caprolactone-Co-DL-Lactide) Copolymer for Potential Treatment of Esophageal Stenosis, Journal of Materials Science: Materials in Medicine 23 (2011) 581-589.

[61] W. Small IV, P. R. Buckley, T. S. Wilson, W. J. Benett, J. Hartman, *et al.*, Shape Memory Polymer Stent with Expandable Foam: A New Concept for Endovascular Embolization of Fusiform Aneurysms, IEEE Transactions on Biomedical Engineering 54 (2007) 1157-1160.

[62] W. Small IV, T. S. Wilson, P. R. Buckley, W. J. Benett, J. M. Loge, *et al.*, Prototype Fabrication and Preliminary In Vitro Testing of a Shape Memory Endovascular Thrombectomy Device IEEE Transactions on Biomedical Engineering 54 (2007) 1657-1666.

[63] H. Tobushi, T. Hashimoto, S. Hayashi, and E. Yamada, Thermomechanical Constitutive Modeling in Shape Memory Polymer of Polyurethane Series, Journal of Intelligent Material Systems and Structures 8 (1997) 711-718.

[64] H. Tobushi, H. Hara, E. Yamada, and S. Hayashi, Thermomechanical Properties in a Thin Film of Shape Memory Polymer of Polyurethane Series, Smart Materials & Structures 5 (1996) 483-491.

[65] H. Tobushi, T. Hashimoto, N. Ito, S. Hayashi, and E. Yamada, Shape Fixity and Shape Recovery in a Film of Shape Memory Polymer of Polyurethane Series, Journal of Intelligent Material Systems and Structures 9 (1998) 127-136.

[66] J. R. Lin and L. W. Chen, Study on Shape Memory Behavior of Polyether-Based Polyurethanes. I. Influence of the Hard-Segment Content, Journal of Applied Polymer Science 69 (1998) 1563-1574.

[67] C. Azra, C. J. G. Plummer, and J.-A. E. Manson, Isothermal Recovery Rates in Shape Memory Polyurethanes, Smart Materials & Structures 20 (2011) 1-10.

[68] T. S. Wilson, J. P. Bearinger, J. L. Herberg, J. E. M. III, W. J. Wright, *et al.*, Shape Memory Polymers Based on Uniform Aliphatic Urethane Networks, Journal of Applied Polymer Science 106 (2007) 540-551.

[69] B. L. Volk, D. C. Lagoudas, and D. J. Maitland, "Characterizing and Modeling the Free Recovery and Constrained Recovery Behavior of a Polyurethane Shape Memory Polymer," presented at the ASME 2010 Conference on Smart Materials, Adaptive Structures, and Intelligent Systems, Philadelphia, PA, 2010.

[70] B. L. Volk, D. C. Lagoudas, and D. J. Maitland, Characterizing and Modeling the Free Recovery and Constrained Recovery Behavior of a Polyurethane Shape Memory Polymer Smart Materials & Structures 20 (2011) 1-15.

[71] B. Atli, F. Gandhi, and G. Karst, Thermomechanical Characterization of Shape Memory Polymers, Journal of Intelligent Material Systems and Structures 20 (2009) 87-95.

[72] B. L. Volk, D. C. Lagoudas, Y.-C. Chen, and K. S. Whitley, Analysis of the Finite Deformation Response of Shape Memory Polymers: I. Thermomechanical Characterization, Smart Materials and Structures 19 (2010) 075005.

[73] C. Schmidt, A. M. S. Chowdhury, K. Neuking, and G. Eggeler, Stress-Strain Behavior of Shape Memory Polymers by 1WE Method: Application to Tecoflex, Journal of Macromolecular Science, Part A: Pure and Applied Chemistry 48 (2011) 204-210.

[74] A. M. S. Chowdhury, C. Schmidt, K. Neuking, and G. Eggeler, Comparative Studies on Thermomechanical Behavior of Veriflex, a Shape Memory Polymer, for a Low Strain (ε_m=70%): Laser Experiments, Journal of Macromolecular Science, Part A: Pure and Applied Chemistry 48 (2011) 707-712.

[75] C. M. Yakacki, R. Shandas, C. Lanning, B. Rech, A. Eckstein, *et al.*, Unconstrained Recovery Characterization of Shape Memory Polymer Networks for Cardiovascular Applications., Biomaterials 28 (2007) 2255-2263.

[76] V. Srivastava, S. A. Chester, and L. Anand, Thermally Actuated Shape Memory Polymers: Experiments, Theory, and Numerical Simulations, Journal of the Mechanics and Physics of Solids 58 (2010) 1100-1124.

[77] W. Voit, T. Ware, and K. Gall, Radiation Crosslinked Shape Memory Polymers, Polymer 51 (2010) 3551-3559.

[78] W. Voit, T. Ware, R. R. Dasari, P. Smith, L. Danz, *et al.*, High-Strain Shape Memory Polymers, Advanced functional materials 20 (2010) 162-171.

[79] N. Lakhera, C. M. Yakacki, T. D. Nguyen, and C. P. Frick, Partially Constrained Recovery of (Meth)acrylate Shape Memory Polymer Networks, Journal of Applied Polymer Science 126 (2012) 72-82.

[80] A. J. W. McClung, G. P. Tandon, and J. W. Baur, Deformation Rate-, Hold Time-, and Cycle-Dependent Shape Memory Performance of Veriflex-E Resin, Mechanics of Time Dependent Materials (2011) 1-14.

[81] A. J. W. McClung, G. P. Tandon, and J. W. Baur, Strain Rate- and Temperature-Dependent Tensile Properties of an Epoxy-based, Thermosetting, Shape Memory Polymer (Veriflex E), Mechanics of Time-Dependent Materials 16 (2012) 205-221.

[82] G. P. Tandon, K. Goecke, K. Cable, and J. Baur, Durability Assessment of Styrene- and Epoxy-Based Shape Memory Polymer Resins, Journal of Intelligent Material Systems and Structures 20 (2009) 2127-2143.

[83] G. P. Tandon, K. Goecke, K. Cable, and J. Baur, Environmental Durability of Fabric-Reinforced Shape Memory Polymer Composites, Journal of Intelligent Material Systems and Structures 21 (2010) 1365-1381.

[84] W. B. Song and Z. D. Wang, Characterization of Viscoelastic Behavior of Shape Memory Epoxy Systems, Journal of Applied Polymer Science (2012) 1-7.

[85] A. J. W. McClung, G. P. Tandon, K. E. Goecke, and J. W. Baur, Non-Contact Technique for Characterizing Full-field Surface Deformation of Shape Memory

Polymers at Elevated and Room Temperatures, Polymer Testing 30 (2011) 140-149.

[86] J. Diani, C. Fredy, P. Gilormini, Y. Merckel, G. Regnier, *et al.*, A Torsion Test for the Study of the Large Deformation Recovery of Shape Memory Polymers, Polymer Testing 30 (2011) 335-341.

[87] S. J. Hong, W.-R. Yu, and J. H. Youk, Two-Way Shape Memory Behavior of Shape Memory Polyurethanes with a Bias Load, Smart Materials & Structures 19 (2010) 1-9.

[88] G. Li and W. Xu, Thermomechanical Behavior of Thermoset Shape Memory Polymer Programmed by Cold-Compression: Testing and Constitutive Modeling, Journal of the Mechanics and Physics of Solids 59 (2011) 1231-1250.

[89] A. Bhattacharyya and H. Tobushi, Analysis of the Isothermal Mechanical Response of a Shape Memory Polymer Rheological Model, Polymer Engineering and Science 40 (2000) 2498-2510.

[90] H. Tobushi, N. Ito, K. Takata, and S. Hayashi, Thermomechanical Constitutive Modeling of Polyurethane-Series Shape Memory Polymer, Materials Science Forum 327-328 (2000) 343-346.

[91] H. Tobushi, K. Okumura, S. Hayashi, and N. Ito, Thermomechanical Constitutive Model of Shape Memory Polymer, Mechanics of Materials 33 (2001) 545-554.

[92] Z. Bailin, H. Xinming, H. Congcong, and Y. Qing, Numerical Verification of Constitutive Relationship for Mechanic Behavior of Shape Memory Polymer, Applied Mechanics and Materials 121-126 (2012) 3514-3519.

[93] J. R. Lin and L. W. Chen, The Mechanical-Viscoelastic Model and WLF Relationship in Shape Memorized Linear Ether-Type Polyurethanes, Journal of Polymer Research 6 (1999) 35-40.

[94] H. A. Khonakdar, S. H. Jafari, S. Rasouli, J. Morshedian, and H. Abedini, Investigation and Modeling of Temperature Dependence Recovery Behavior of

Shape Memory Crosslinked Polyethylene, Macromolecular Theory and Simulations 16 (2007) 43-52.

[95] M. Bonner, H. M. d. Oca, M. Brown, and I. M. Ward, A Novel Approach to Predict the Recovery Time of Shape Memory Polymers, Polymer 51 (2010) 1432-1436.

[96] A. Srinivasa and P. Gosh, A Simple, Gibbs Potential Based Multinetwork Model for Shape Memory Polymers, Smart Devices: Modeling of Material Systems, An International Workshop 1029 (2008) 58-74.

[97] P. Ghosh and A. R. Srinivasa, A Two-Network Thermomechanical Model of a Shape Memory Polymer, International Journal of Engineering Science 49 (2011) 823-838.

[98] Z. D. Wang, D. F. Li, Z. Y. Xiong, and R. N. Chang, Modeling Thermomechanical Behaviors of Shape Memory Polymer, Journal of Applied Polymer Science 113 (2009) 651-656.

[99] B. Zhou, Y.-J. Liu, X. Lan, J.-S. Leng, and S.-H. Yoon, A Glass Transition Model for Shape Memory Polymer and its Composite, International Journal of Modern Physics B 23 (2009) 1248-1253.

[100] B. Zhou, Y.-J. Liu, and J.-S. Leng, A Macro-Mechanical Constitutive Model for Shape Memory Polymer, Science China: Physics, Mechanics, and Astronomy 53 (2010) 2266-2273.

[101] J. M. Husson, F. Dubois, and N. Sauvat, A Finite Element Model for Shape Memory Behavior, Mechanics of Time-Dependent Materials 15 (2011) 213-237.

[102] P. Gilormini and J. Diani, On Modeling Shape Memory Polymers as Thermoelastic Two-Phase Composite Materials, Comptes Rendus Mecanique 340 (2012) 1-11.

[103] J. H. Kim, T. J. Kang, and W.-R. Yu, Simulation of Mechanical Behavior of Temperature-Responsive Braided Stents Made of Shape Memory Polyurethanes, Journal of Biomechanics 43 (2010) 632-643.

[104] M. Baghani, R. Naghdabadi, J. Arghavani, and S. Sohrabpour, A Constitutive Model for Shape Memory Polymers with Application to Torsion of Prismatic Bars, Journal of Intelligent Material Systems and Structures 23 (2012) 107-116.

[105] M. Baghani, R. Naghdabadi, J. Arghavani, and S. Sohrabpour, A Thermodynamically-Consistent 3D Constitutive Model for Shape Memory Polymers, International Journal of Plasticity 35 (2012) 1-18.

[106] M. Baghani, R. Naghdabadi, and J. Arghavani, A Semi-Analytical Study on Helical Springs Made of Shape Memory Polymer, Smart Materials & Structures 21 (2012) 1-11.

[107] J. Diani, Y. Liu, and K. Gall, Finite Strain 3D Thermoviscoelastic Constitutive Model for Shape Memory Polymers, Polymer Engineering and Science 46 (2006) 486-492.

[108] X. Chen and T. D. Nguyen, Influence of Thermoviscoelastic Properties and Loading Conditions on the Recovery Performance of Shape Memory Polymers, Mechanics of Materials 43 (2011) 127-138.

[109] T. D. Nguyen, H. J. Qi, F. Castro, and K. N. Long, A Thermoviscoelastic Model for Amorphous Shape Memory Polymers: Incorporating Structural and Stress Relaxation, Journal of the Mechanics and Physics of Solids 56 (2008) 2792-2814.

[110] T. D. Nguyen, C. M. Yakacki, P. D. Brahmbhatt, and M. L. Chambers, Modeling the Relaxation Mechanisms of Amorphous Shape Memory Polymers, Advanced Materials 22 (2010) 3411-3423.

[111] K. K. Westbrook, P. H. Kao, F. Castro, Y. Ding, and H. J. Qi, A 3D Finite Deformation Constitutive Model for Amorphous Shape Memory Polymers: A Multi-Branch Modeling Approach for Nonequilibrium Relaxation Processes, Mechanics of Materials 43 (2011) 853-869.

[112] K. K. Westbrook, V. Parakh, T. Chung, P. T. Mather, L. C. Wan, *et al.*, Constitutive Modeling of Shape Memory Effects in Semicrystalline Polymers with Stretch Induced Crystallization, Journal of Engineering Materials and Technology 132 (2010) 1-9.

[113] Y.-C. Chen and D. C. Lagoudas, A Constitutive Theory for Shape Memory Polymers. Part I: Large Deformations, Journal of the Mechanics and Physics of Solids 56 (2008) 1752-1765.

[114] Y.-C. Chen and D. C. Lagoudas, A Constitutive Theory for Shape Memory Polymers. Part II: A Linearized Model for Small Deformations, Journal of the Mechanics and Physics of Solids 56 (2008) 1766-1778.

[115] B. L. Volk, D. C. Lagoudas, and Y.-C. Chen, Analysis of the Finite Deformation Response of Shape Memory Polymers: II. 1D Calibration and Numerical Implementation of a Finite Deformation, Thermoelastic Model, Smart Materials and Structures 19 (2010) 1-11.

[116] H. J. Qi, T. D. Nguyen, F. Castroa, C. M. Yakacki, and R. Shandas, Finite Deformation Thermo-Mechanical Behavior of Thermally Induced Shape Memory Polymers, Journal of the Mechanics and Physics of Solids 56 (2008) 1730-1751.

[117] S. Reese, M. Bol, and D. Christ, Finite Element Based Multi-Phase Modelling of Shape Memory Polymer Stents, Computer Methods in Applied Mechanics and Engineering 199 (2010) 1276-1286.

[118] ASTM International, D638-08: Standard Test Method for Tensile Properties of Plastics, ed, 2003, pp. 1-16.

[119] D. L. Safranski and K. Gall, Effect of Chemical Structure and Crosslinking Density on the Thermo-Mechanical Properties and Toughness of (Meth)acrylate Shape Memory Polymer Networks, Polymer 49 (2008) 4446-4455.

[120] M. E. Gurtin, An Introduction to Continuum Mechanics. San Diego: Academic Press, 1981.

[121] G. A. Holzapfel, Nonlinear Solid Mechanics: A Continuum Approach for Engineering. West Sussex: John Wiley & Sons Ltd., 2000.

[122] W. H. Press, S. A. Teukolsky, W. T. Vetterling, and B. P. Flannery, Numerical Recipes: The Art of Scientific Computing. New York: Cambridge University Press, 2007.

[123] D. Lagoudas, D. Hartl, Y. Chemisky, L. Machado, and P. Popov, Constitutive Model for the Numerical Analysis of Phase Transformation in Polycrystalline Shape Memory Alloys, International Journal of Plasticity 32-33 (2012) 155-183.

[124] D. Christ and S. Reese, A Finite Element Model for Shape Memory Alloys Considering Thermomechanical Couplings at Large Strains, International Journal of Solids and Structures 46 (2009) 3694-3709.

[125] J. C. Simo and T. J. R. Hughes, Computational Inelasticity. New York: Springer-Verlag, 1998.

[126] Simulia, Abaqus User's Manual, ed: Dassault Systemes, 2012.

APPENDIX A

POLAR DECOMPOSITION ALGORITHM

In this appendix, the polar decomposition algorithm is presented that was used in the three-dimensional numerical implementation of the constitutive model in Chapter IV. This algorithm is shown in the Simo and Hughes book [113] as Box 7.1. This algorithm is used in the current work to take the polar decomposition of the deformation gradient $\mathbf{F}$, which is provided as input from Abaqus, to obtain the rotational and stretch components ($\mathbf{R}$ and $\mathbf{U}$). The stretch tensor is then used as input to the system of equations that are solved using the Newton-Raphson method. After the unknown stretches in the rubbery and glassy phases ($\mathbf{U}_e^r$ and $\mathbf{U}_e^g$) are solved for using the Newton-Raphson method, the total elastic deformation gradients for the rubbery and glassy phases are obtained by multiplying the stretches by the rotation $\mathbf{R}$ (recall the assumption that the rotations in each phase are considered equal to the rotation of the average deformation gradient).

The first step to the algorithm is to obtain the squares of the principal stretches, which are the eigenvalues of the right Cauchy-Green deformation tensor $\mathbf{C}$. As $\mathbf{C}$ is the square of the stretch tensor $\mathbf{U}$ $\left(\mathbf{C}=\mathbf{U}^2\right)$, the eigenvalues of $\mathbf{C}$ are the square of the eigenvalues of $\mathbf{U}$. The first step in the algorithm is to calculate the quantities in Equation (155).

$$
\begin{aligned}
b &= I_2 - I_1^2 \big/ 3 \\
c &= -\frac{2}{27} I_1^3 + \frac{I_1 I_2}{3} - I_3
\end{aligned}
\tag{155}
$$

where I_1, I_2, and I_3 are the first, second, and third invariants of $\mathbf{C}$, respectively. The absolute values of b are then checked to see if they are smaller than the tolerance value. If b is sufficiently small to cause numerical problems, the squares of the eigenvalues are calculated through Equation (156), where the quantities are calculated for $A = 1, 2, 3$

$$
\begin{aligned}
x_A &= -c^{1/3} \\
\lambda_A^2 &= x_A + I_1 \big/ 3
\end{aligned}
\tag{156}
$$

On the other hand, if the absolute value of b is greater than the tolerance value, then the squares of the eigenvalues are calculated through Equation (157).

$$
\begin{aligned}
m &= 2\sqrt{-b/3} \\
n &= \frac{3c}{mb} \\
t &= \arctan\left[\sqrt{1-n^2} \,/\, n \right] \Big/ 3 \\
x_A &= m \, \cos\left[t + 2(A-1)\pi / 3 \right] \\
\lambda_A^2 &= x_A + I_1 / 3
\end{aligned}
\tag{157}
$$

After calculating the eigenvalues of $\mathbf{U}$ (through taking the square root of the eigenvalues of $\mathbf{C}$), the invariants of $\mathbf{U}$ are calculated through Equation (158).

$$
\begin{aligned}
i_1 &= \lambda_1 + \lambda_2 + \lambda_3 \\
i_2 &= \lambda_1\lambda_2 + \lambda_1\lambda_3 + \lambda_2\lambda_3 \\
i_3 &= \lambda_1\lambda_2\lambda_3
\end{aligned}
\tag{158}
$$

Using these invariants, the stretch tensor $\mathbf{U}$ and its inverse $\mathbf{U}^{-1}$ are calculated through Equation (159).

$$\begin{aligned} D &= i_1 i_2 - i_3 \\ &= \left(\lambda_1 + \lambda_2\right)\left(\lambda_1 + \lambda_3\right)\left(\lambda_2 + \lambda_3\right) > 0 \\ \mathbf{U} &= \frac{1}{D}\left[-\mathbf{C}^2 + \left(i_1^2 - i_2\right)\mathbf{C} + i_1 i_3 \mathbf{I}\right] \\ \mathbf{U}^{-1} &= \frac{1}{i_3}\left[\mathbf{C} - i_1 \mathbf{U} + i_2 \mathbf{I}\right] \end{aligned} \tag{159}$$

Finally, the rotation tensor $\mathbf{R}$ is calculated through Equation (160).

$$\mathbf{R} = \mathbf{F}\mathbf{U}^{-1} \tag{160}$$

APPENDIX B

COMPRESSION SHAPE MEMORY TEST

In this appendix, the results to a preliminary free recovery compression experiment on a cylindrical shape memory polymer are presented. The experiment is performed on the same polyurethane shape memory polymer discussed in Chapter II. Instead of injecting the polymer resin into an aluminum mold for curing, the resin was injected into a 20mL syringe. A needle tip was placed on the end of the syringe to allow air to escape, and the syringe was cured upside down (with the needle pointing up). After curing, the cylinder was cut using a lathe into cylindrical samples approximately 17mm in diameter and 17mm in length. A picture of one of the final samples, prepared for testing with the laser extensometer, is presented in Figure 60.

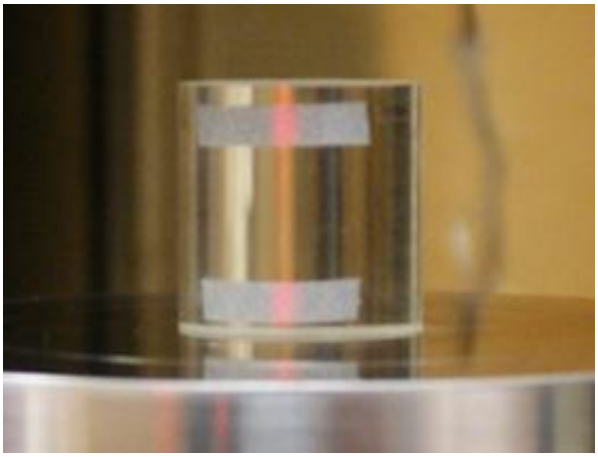

Figure 60 – Cylindrical shape memory polymer sample ready that has been cut with a lathe and has reflective strips attached to the surface for use with the laser extensometer.

In performing the experiment, the shape memory polymer was first heated to 90°C and then the upper compression platen was lowered to compress the sample by 10% extension. The crosshead was then held constant and the temperature was lowered to 25°C. During this cooling procedure, the extension rods, compression platen, and shape memory polymer all undergo thermal contraction. As a result of this thermal contraction and the transformation from the rubbery phase to the glassy phase, the SMP loses contact with the compression platen during the cooling process and the stress drops to zero. Consequently, there is no need for an unloading step (as performed in the tension experiments) after the end of cooling; however the upper compression platen is moved up to avoid interference with the sample during the free recovery heating.

The displacement of the upper compression platen as a function of temperature is presented in Figure 61. This result was obtained by cycling the temperature from 25°C to 90°C and back to 25°C at 1°C/min with no sample present. The displacement of the grip was measured by attaching laser extensometer tapes to the edge of the compression platen. From this figure, it is observed that there is approximately an 11°C delay before noticeable displacement is observed in the compression platen, and then the displacement of the platen is approximately linear with respect to temperature.

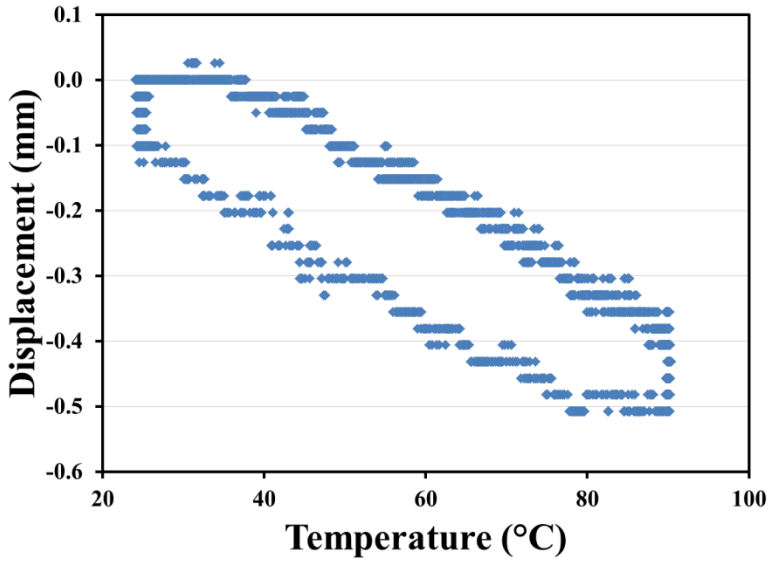

Figure 61 – Displacement of the compression platen as a function of temperature when cycled from 25°C to 90°C and back to 25°C at 1°C/min.

With the thermal contraction of the compression platen used as an input to the constitutive model in Chapter IV, the results of the model predictions to the experimental results are shown in Figure 62. In this figure, two modeling results are shown. The first is the prediction if the temperature of the material is assumed to increase uniformly throughout the sample. The second prediction is assuming the top and bottom of the sample are heated 11 minutes slower than the outside of the sample, to model the effects of the delay in the change of temperature in the grips observed in Figure 61. Good agreement is observed between the model predictions and the experimental data through the deforming and cooling step. However, Figure 62 indicates the assumption of uniform heating during recovery underpredicts the effective transformation temperature of the SMP by about 7°C. On the other hand, by using the simplified thermal boundary conditions that the nominal temperature change is applied

to the lateral surface of the SMP and that the top and bottom of the material are heated 11°C slower, the model predictions are much closer to the experimental data with a deviation of only 2°C. These results further highlight the necessity to consider the coupled temperature-displacement behavior of SMPs when attempting to predict the material response for thicker specimens undergoing complex thermal boundary conditions.

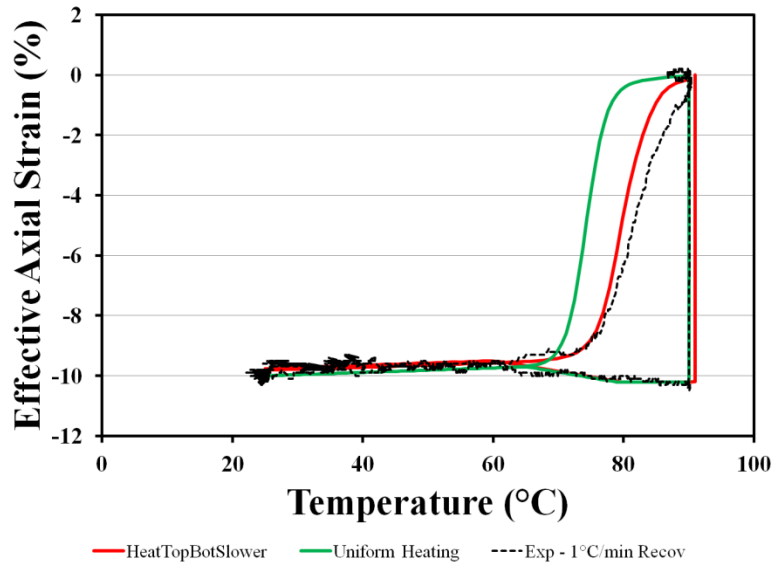

Figure 62 – Comparison of experimental results to model predictions for the 10% free recovery compression experiment. The model prediction assuming uniform heating of the SMP is shown as well as the prediction assuming the top and bottom are heated slower due to effects of the compression platen heating/cooling slower.

APPENDIX C

RECOMMENDED PROTOCOL FOR CALIBRATING THE CONSTITUTIVE MODEL PARAMETERS

In Chapter IV, the kinematics and constitutive equations were presented that describe the response of thermosetting shape memory polymers. In the development of this model, only the thermoelastic responses of the rubbery and glassy phases were considered. As a result, the following calibration parameters were introduced in the system of equations:

- Shear modulus of the rubbery and glassy phases
- Lamé constants of the rubbery and glassy phases
- Coefficients of thermal expansion of the rubbery and glassy phases
- Glassy volume fraction

And, for cases in which the coupled thermomechanical analysis is considered, the following additional parameters are necessary:

- Density
- Specific heat
- Thermal conductivity

In calibrating these parameters, it is first recommended to perform dynamic mechanical analysis (DMA) and differential scanning calorimetry (DSC) on the specimen. The DSC will provide an indication of the glass transition temperature and the DMA will provide an indication of the elastic and viscoelastic response of the

material as a function of temperature. In these results, it is recommended to consider the plateau regions in both the glassy and the rubbery phases.

To obtain both the shear moduli and the Lamé constants in each phase, it is necessary to perform experiments that will provide information on at least two elastic constants of the material. Such experiments may include (i) isothermal loading/unloading experiments with digital image correlation or strain gauges to obtain both the tensile modulus and the Poisson's ratio or (ii) isothermal loading/unloading in addition to a shear/torsion test to obtain the tensile modulus and the shear modulus. Strain-to-failure experiments in the rubbery and glassy phases will provide information regarding the maximum expected strain during a strain recovery profile as well as the degree of nonlinearity of the stress-strain curve during loading. These experiments should be performed at multiple orientations to confirm the isotropy of the material response.

To obtain the coefficients of thermal expansion, it is recommended to perform thermomechanical analysis (TMA) on cylindrical samples of the SMP. The TMA provides a direct mechanism for obtaining the displacement as a function of temperature while maintaining approximately zero applied load. From the slope of the displacement vs. temperature data and knowledge of the initial length of the specimen, the coefficients of thermal expansion for both phases can be calculated. In cases where TMA is not available or to aid in evaluating the isotropy of the coefficients of thermal expansion tensor, it is recommended to use a noncontact measurement technique with a temperature chamber and tensile tester. By hanging the sample from the top grip (in

different orientations) and changing the temperature, the coefficients of thermal expansion can be derived from the change in the specimen length as a function of temperature.

To obtain the glassy volume fraction, it is recommended to perform a free recovery (zero load) experiment and measuring the strain recovery as a function of temperature. It is recommended to load the specimen at temperatures well above the glass transition temperature (in the rubbery phase plateau of the DMA) and cooling to well below the glass transition temperature (in the glassy phase plateau of the DMA). During the free recovery heating, a plateau at the beginning and end of the strain recovery will be observed. The functional form for the glassy volume fraction in Chapters III and IV can then be obtained by normalizing this strain recovery profile and fitting the calibration constants A and B (and C, when a piecewise hyperbolic tangent is used) using a least squares method.

Finally, to obtain the thermal material properties, namely the specific heat and thermal conductivity, it is recommended to use a piece of equipment such as a thermal conductivity analyzer. Such equipment will obtain these material properties by applying stimulus and measuring the change in temperature.